An Investigation of the Bursting of Trailing Vortices Using Numerical Simulation

Thesis by
Philip Stewart Beran

In Partial Fulfillment
of the Requirements for the Degree of
Doctor of Philosophy

California Institute of Technology
Pasadena, California

1989
(Submitted May 30, 1988)

To Kendra

Acknowledgements

I would very much like to thank my advisor, Professor Fred E. C. Culick, for the invaluable advice and inspiration he has given to me during this study. I feel very fortunate to have worked under such a wise and patient man. The long-distance assistance he provided in the preparation of this document will always be appreciated.

I would also like to thank Drs. Lewis Schiff and Murray Tobak of the NASA Ames Research Center for countless, insightful and thought-provoking discussions on vortex breakdown, and for their support of this research.

I am very grateful to my parents for all the encouragement they have given to me over the years, especially for that which motivated me to begin and carry out this work.

Finally, I would like to express my deepest gratitude to my wife, Kendra, who, through her loving support and contagious energy, made the completion of this work possible.

This research was sponsored by the NASA Post-Baccalaureate Program, project number NCC 2-309.

Abstract

Solutions of the Navier-Stokes equations are obtained for the flow of an isolated, trailing vortex, and for the swirling flow through a frictionless pipe. In both cases, the flow is assumed to be steady, incompressible and rotationally symmetric. Solutions are computed using Newton's method and Gaussian elimination for a wide range of values of two parameters: Reynolds number, Re, and vortex strength, V. Pseudo-arclength continuation is employed to facilitate the computation of solution points in the parameter space. The numerical procedure is validated through comparison of solutions with solutions obtained in previous investigations for the case of a trailing vortex. Solutions are also compared with results reported by Brown and Lopez (1988) for the case of flow through a pipe.

Solutions of the quasi-cylindrical equations are obtained for the flow of a trailing vortex. Solutions are computed using an explicit, space-marching scheme, and are compared with solutions of the Navier-Stokes equations.

Provided that Re is about 200, or larger, four vortex states are observed.

1. When V is sufficiently small, the flow is entirely supercritical.

2. As V is increased, the flow at an axial station becomes critical and a transition point forms. At the point, the flow departs from an upstream state that is supercritical to a downstream state that is marked by large-amplitude, spatial oscillations of core radius. When Re is large, the downstream state is nearly periodic. The general features of transition are well described by the conjugate-flow theory of Benjamin (1967). Failure of the quasi-cylindrical equations is found to be a necessary and sufficient condition for the existence of a transition point. As V is further increased, the transition point moves

upstream. Reversed flow is not observed.

3. Over a narrow range of vortex strengths, a small bubble of reversed flow is observed downstream of the transition point.

4. When V is large, the entire flow is marked by large-amplitude, spatial oscillations of core radius. A transition point is not evident within the computational domain. Typically, large regions of reversed flow are observed.

Contents

List of Figures

List of Tables

Chapter 1

Introduction

1.1 The Phenomenon of Vortex Breakdown

The phenomenon of vortex breakdown has been an enigma since it was first observed by Peckham and Atkinson (1957) in the flow above highly swept wings at large angle-of-attack. The phenomenon has been the subject of numerous experimental, computational and theoretical investigations, and yet the mechanisms responsible for vortex breakdown are still not adequately understood.

Vortex breakdown is a feature of rotational flows involving a concentrated core of vorticity imbedded in a largely irrotational flow that is moving in a direction approximately parallel to the vortex. Examples of such flows are swirling flows through pipes and the vortical flows produced by delta wings at large angle-of-attack. "Vortex breakdown" is the term used to identify the development of a stagnation point on a vortex core, followed by a limited region of reversed flow, with an associated dramatic increase of core size. "Vortex bursting" is another term sometimes used to identify this phenomenon, although in this work, the term will be given the broader meaning of identifying any abrupt increase in core radius, regardless of whether or not a stagnation point forms.

The study of vortex breakdown is important to the disciplines of both aerodynamics and combustion physics. The breakdown of the leading-edge vortices over a delta wing can have a significant effect on an aircraft's dynamics through large changes in the lift, drag and moment coefficients. It is thus desirable to be able to

predict when breakdown will occur and at what position along the vortex it will develop. Faler and Leibovich (1978) have also noted that it is important to understand the structure of the flow that develops as a consequence of vortex breakdown in some applications involving combustion chambers. In these applications, flows are purposefully generated, which lead to vortex breakdown so that the resulting bubble of recirculating fluid can be used as a "fluid-dynamic flameholder."

In the remaining portion of this section, a summary of the experimental and computational studies of vortex breakdown will be provided. A discussion of the theories proposed to explain vortex breakdown is postponed until Section (1.2). There have been several review papers on vortex breakdown, including the reports by Hall (1972), Leibovich (1978), Leibovich (1984) and Hall (1985).

Early experimental investigations on the breakdown of leading-edge vortices were conducted by Elle (1960) and Lambourne and Bryer (1961) to further investigate the phenomenon observed by Peckham and Atkinson (1957). Many useful observations were made in these studies, but quantitative results were difficult to obtain because of the sensitivity of the breakdown structure to intrusion of probes into the vortex core. One of the most important observations was the finding of two distinct types of vortex breakdown. A "famous" picture taken by Lambourne and Bryer of the breakdown of the leading-edge vortices over a delta wing, reproduced in Figure 2 of Hall's (1972) review, clearly captures the features of these two types. The structure of each vortex core was made visible by injecting dye into the flow near the wing apex. One type of vortex breakdown, termed "bubble breakdown," was distinguished by the near-axisymmetric swelling of the core into the shape of a bubble, followed by the turbulent disintegration of the vortex. The other type, "spiral breakdown," was characterized by an abrupt transformation of the nearly linear core into the form of a helical filament. Several turns of the helical core were observed before the disintegration of the vortex.

The discovery of a near-axisymmetric form of vortex breakdown spawned a long series of experiments carried out by several investigators, involving the visualiza-

tion of vortex breakdown in circular tubes. Vortices were generated by passing water through a set of swirl vanes near the entrance to a circular test section and visualized by introducing dye into the center of the vortex, upstream of the test section. Test sections were generally constructed of Plexiglas to permit visualization from arbitrary angular positions. The first of these experiments was conducted by Harvey (1962). Subsequent experiments were performed by Kirkpatrick (1964); Sarpkaya (1971A); Sarpkaya (1971B); Sarpkaya (1974); Faler and Leibovich (1977); Garg (1977); and Faler and Leibovich (1978). To avoid the difficulties associated with the introduction of probes into the flowfield, laser-doppler anemometry was used in the last of the three experimental investigations listed to provide quantitative flowfield data. Faler and Leibovich (1977) used laser-doppler anemometry to obtain a quantitative description, at the entrance of the test section, of those flows leading to vortex breakdown, in an effort to verify predictions made by Benajmin in his conjugate-flow theory of vortex breakdown. Garg (1977) and Faler and Leibovich (1978) used the same measurement technique to obtain a quantitative description of the internal structure of the bubble type of vortex breakdown.

With the vane-tube apparatus, investigators were able to exercise a greater degree of control over parameters characterizing flows leading to vortex breakdown than in experiments involving delta-wing models. As a result, tube experiments yielded more precise visualizations of the breakdown phenomenon. Two parameters, flow rate and vane angle, were free to be varied in tube experiments in which the geometry of the test section was fixed (Sarpkaya (1974) investigated the effects of tube divergence on breakdown devlopment). By increasing the vane angle, vortex circulation was caused to increase, while by varying flow rate, Reynolds number of the flow, based on mean axial velocity and tube diameter, was controlled.

Through the imposition of rotational symmetry on the flow entering the test section of the vane-tube apparatus, a wider class of breakdown types was observed. In distinction, the naturally asymmetric flow formed over delta wings was

preferentially susceptible to the spiral form of vortex breakdown. Faler and Leibovich (1977) found seven distinct types of large-amplitude disturbances of vortices in tubes. Five of these types involved stagnation points in the core and thus are identified as vortex breakdown in the sense defined above. The different types were observed to comprise an evolutionary sequence of disturbances involving transitions between type as vane angle was increased with Reynolds number fixed. (The disturbance of type 6, in the classification system of Faler and Leibovich, is called the "double-helix" form and was found previously by Sarpkaya (1971A). It is not a form of vortex breakdown.)

The type 0 form of breakdown is the bubble breakdown mentioned above. According to Faler and Leibovich, the type 0 form is "characterized by a stagnation point on the swirl axis, followed by an abrupt expansion of the centerline dye filament to form the envelope of a bubble of recirculating fluid. The envelope has a high degree of axial symmetry over most of its length, but the rear is not closed and is asymmetric." The last observation is common to all experimental studies of breakdown—some degree of asymmetry in the breakdown structure is always present.

The type 2 form of breakdown is the spiral breakdown, a common feature of the flows above delta wings at high angle-of-attack. However, when this form is observed in tubes, the helical-shaped core turns in the same angular direction as the flow, opposite to the observed behavior of spiral breakdowns above delta wings.

Type 0 and type 2 are the forms of breakdown most often observed in experiment and thus are generally the focus of past and present investigations. Refer to the report by Faler and Leibovich (1977) for a description of the remaining five forms of vortex disturbance.

There are several aspects of the behavior of both types of breakdown that warrant particular attention. In all experiments it was found that there was a certain degree of unsteadiness in axial position of the breakdown forms, no matter what steps were taken to eliminate disturbances from the flow upstream of the

stagnation point. The level of unsteadiness was found to increase with increasing Reynolds number or vane angle. Variations in axial position ranged typically from one-quarter to one-half of a tube radius. However, the mean position of breakdown, if viewed over a sufficient period of time, was found by Faler and Leibovich (1977) to be a repeatable function of vane angle and Reynolds number.

By increasing either Reynolds number or the vane angle, Faler and Leibovich (1977) observed that the breakdown structure moved upstream, leading to an decrease of the size of the breakdown bubble (type 0) or a reduction of the radial extent of the helical core (type 2). Although bubbles of the type 0 form are not completely closed at the rear end, a vortex core was reestablished downstream of the bubble. The radius of the vortex core downstream of the bubble was observed to be at least twice that of the core upstream of the bubble. The core downstream of the bubble was found to be short-lived, however, and breaks down into the type 2 form at an axial position approximately one bubble diameter downstream of the rear of the bubble.

Sarpkaya (1971A,B) and Faler and Leibovich (1977) also found that the form into which the vortex breaks down is not always constant in time but is subject to random changes. Over a wide range of values of Reynolds number and vane angle, the type 2 form would occasionally move upstream and transform into a type 0 bubble. After a short period of time, typically a few seconds, the bubble would move downstream, transforming back into type 2 form. Faler and Leibovich found no net change in the mean axial position of the spiral breakdown after a complete cycle of the transformation process. During the transformation process, the type 0 form was always observed upstream of the type 2 form, by a distance approximately equal to several core diameters. In general, type 2 forms were found more often when the vane angle was small and less often when the vane angle was large.

With the assumption that physical mechanisms responsible for bubble breakdown are axisymmetric in nature, some investigators began to model vortex break-

down, using digital computers. The first of these studies was carried out in 1967 by Hall, using a set of equations, approximating the Navier-Stokes equations, called the "quasi-cylindrical" equations. The theory of vortex breakdown proposed by Hall, in which these equations play a central role, is discussed in more detail in the next section. Kopecky and Torrance (1973) were first to model vortex breakdown using the Navier-Stokes equations. Since 1973, results of numerical simulation, using the Navier-Stokes equations, have been reported by Grabowski (1974); Krause et al. (1983); Hafez et al. (1986); Beran (1987); Hafez et al. (1987); Brown and Lopez (1988); Lopez (1988); and Menne (1988). Each of these studies assumed the flow to be rotationally symmetric, thereby eliminating the possibility of studying the nonaxisymmetric features of vortex breakdown.

Nakamura et al. (1985) and Nakamura et al. (1986) have used the vortex filament method to model vortex breakdown without the assumption of rotational symmetry.

There are several aspects of vortex breakdown that make it an attractive phenomenon to simulate numerically. First, even with the use of laser-doppler anemometry, it is difficult to obtain a complete, quantitative description of the flowfield in which breakdown is observed to occur. Through numerical simulation, such difficult quantities to measure, as pressure and vorticity, are readily obtained. Second, with the *assumption* of rotational symmetry, the problem simplifies to a two-dimensional problem, allowing solutions to be computed on rectangular domains, for which appropriate boundary conditions are not difficult to formulate. Third, since the phenomenon has been visualized in numerous experiments, there is a considerable body of qualitative information that may serve to validate computations. Fourth, vortex breakdown is observed in incompressible flows, so that after the boundary conditions are specified, Reynolds number is the only parameter on which the flow depends. Finally, numerical modeling is an attractive alternative for the simple reason that numerous experimental investigations have yet to inspire a workable theory of vortex breakdown.

The questionable aspect of most numerical simulations has been the assumption of rotational symmetry. As emphasized by Faler and Leibovich (1977), the term axisymmetric breakdown is a "misnomer" since no breakdown form is truly axisymmetric. However, numerical simulations reported by Grabowski (1974); Beran (1987); Hafez et al. (1987); Lopez (1988); and Brown and Lopez (1988), have been quite successful in reproducing the structure of the axisymmetric breakdown. In fact, computational results were directly compared with flow visualizations in the last of the two references listed above, and found to be very accurate representations of the experimentally observed flows.

1.2 Theories of Vortex Breakdown

There have been several theoretical attempts, based on the assumption of rotational symmetry, to explain the phenomenon of vortex breakdown. Most of these theories have been reviewed by Hall (1972) and Leibovich (1978). There have also been many theoretical investigations in which rotational symmetry was not assumed. This work has been reviewed by Leibovich (1984).

The theories that rely on the assumption of axisymmetry fail, of course, to account for the asymmetric features of vortex breakdown. They also fail to explain adequately the axisymmetric structure of vortex breakdown, observed through experiment and numerical simulation. The main objectives of this work, described in more detail in Section (1.3), are to provide as complete a description of axisymmetric breakdown as possible and to compare computed results with theories of axisymmetric breakdown. The philosophy of this approach is that a valid theory of axisymmetric breakdown should be verifiable through numerical experiment. Once a valid theory is constructed, it may be possible to expand the theory to incorporate flow asymmetries.

An attempt to compare results with all theories of vortex breakdown is not made in this work. However, results will be compared to a set of three representative theories, which are described in Sections 1.2.2-1.2.4. Prior to this discussion

the fundamental concept of flow criticality is examined.

1.2.1 Flow Criticality

Rotationally symmetric flows of fluids of constant density are partially governed by the equation

$$\psi_{zz} + \psi_{rr} - \psi_r/r = -r\eta, \tag{1.1}$$

where ψ is the Stokes streamfunction and η is the azimuthal vorticity. These variables are expressed in terms of the velocity components in (2.4)—(2.7). A subscripted variable represents differentiation of the variable with respect to the subscript. Refer to the schematics in Figures (2.1) and (2.2) to visualize how the coordinate system and velocity components are defined.

The governing equations, including (1.1), reduce to a single governing equation when the fluid is inviscid (see Batchelor (1967) for details):

$$\psi_{zz} + \psi_{rr} - \psi_r/r = r^2\frac{dH}{d\psi} - \Gamma\frac{d\Gamma}{d\psi}. \tag{1.2}$$

The total head, H, and circulation (divided by 2π), Γ, are functions of ψ alone for inviscid flow and are defined as follows:

$$H(\psi) = P/\rho + \frac{1}{2}(u^2 + v^2 + w^2), \tag{1.3}$$

$$\Gamma(\psi) = rv. \tag{1.4}$$

Equation (1.2) can be rewritten as (Benjamin (1962))

$$\psi_{yy} + \frac{1}{2y}\psi_{zz} = \frac{dH}{d\psi} - \frac{1}{2y}\frac{dI}{d\psi}, \tag{1.5}$$

where

$$y \equiv \frac{1}{2}r^2, \tag{1.6}$$

$$I \equiv \frac{1}{2}\Gamma^2. \tag{1.7}$$

The criticality of a columnar flow (i.e., a flow free of axial gradients) depends on its ability to support standing waves of infinitesimal amplitude. As defined by Benjamin (1962), a flow is subcritical when waves of finite wavelength are supportable and supercritical when no waves are supportable. The flow is termed critical when it may support a standing wave of both infinitesimal amplitude and infinite wavelength. The concept of flow criticality may be extended to flows with axial gradients, provided that these gradients are sufficiently small. In these cases the criticality of the flow is dependent on axial position.

Flow criticality is evaluated through a linear analysis of (1.5). The development provided below follows that put forth by Benjamin (1962).

The streamfunction is assumed to take the form

$$\psi(y,z) = \Psi(y) + \epsilon\phi(y)e^{\gamma z}, \tag{1.8}$$

where the "base flow," Ψ, satisfies

$$\ddot{\Psi} = \dot{H}(\Psi) - \frac{1}{2y}\dot{I}(\Psi). \tag{1.9}$$

Note that a dotted function represents differentiation of the function with respect to the single variable on which the function depends. Substitution of (1.8) and (1.9) into (1.5) yields, in the limit $\epsilon \to 0$,

$$\ddot{\phi} + \left(\frac{\gamma^2}{2y} + P(\Psi,y)\right)\phi = 0, \tag{1.10}$$

where

$$P(\Psi,y) = -\ddot{H}(\Psi) + \frac{1}{2y}\ddot{I}(\Psi). \tag{1.11}$$

Equation (1.10) (when supplemented with appropriate boundary conditions) represents an eigenproblem for the eigenvalue γ^2 and the eigenfunction ϕ. The eigenproblem has an infinite spectrum of eigenvalues. Let γ_o^2 be the smallest eigenvalue. According to the definitions of subcritical, critical and supercritical flow given above, the base flow is subcritical when γ_o^2 is negative, critical when γ_o^2 is zero and supercritical when γ_o^2 is positive.

If the base flow, $\Psi(y)$, is not columnar, but slowly changes with axial position, then both (1.9) and (1.10) are approximately satisfied. In general, γ_o^2 will also slowly vary with axial position and may change sign at some axial station, implying a change in flow criticality at that station.

As shown by Benjamin (1962), flow criticality has an important bearing upon the phase speed of travelling waves supported by the base flow. Travelling waves supported by a supercritical base flow have a positive phase speed and thus move in the flow direction. In contrast, travelling waves with negative phase speed are admissible when the flow is subcritical. Travelling waves of long wavelength (i.e., $|\gamma| \rightarrow 0$) have the most negative phase speed when the base flow is subcritical. The eigenproblem for travelling waves is treated in Appendix C. There, a simple example is provided to demonstrate the relationship between flow criticality and the phase speed of supportable waves.

1.2.2 Hall's Boundary-Layer-Analogy Theory

The Navier-Stokes equations for swirling flows with rotational symmetry may be approximated by a simpler set of equations, referred to as the "quasi-cylindrical" (QC) equations, when the Reynolds number is sufficiently large. In this limit, axial gradients of flow quantities can be assumed small in comparison to radial gradients. Swirling flows that exhibit this character are termed "quasi-cylindrical." The idea of applying the QC equations to the study of vortex breakdown was first conceived by Gartshore (1962), although the equations were first solved numerically by Hall (1965). These equations, the derivation of which is included in Appendix A, are mathematically analogous to the boundary-layer equations for two-dimensional flows.

It is generally observed in experiment that swirling flows upstream of breakdown are quasi-cylindrical. It is also found in plane flows that the flow upstream of a separation point is well approximated by the boundary-layer equations. The position of the separation point may be predicted approximately by integrating

the boundary-layer equations in the streamwise direction until a computed separation point is found, even though the boundary-layer equations fail at that point. Hall's theory postulates that the position of vortex breakdown may be predicted by integrating the QC equations in the streamwise direction, starting at some axial station where the flow is quasi-cylindrical and assumed known, until large axial gradients in the flow are observed, and the integration process fails. Furthermore, Hall (1972) showed that calculations diverge at an axial station at which the flow becomes critical.

Hall (1967) integrated the QC equations to simulate numerically the experiment performed by Kirkpatrick (1964). Hall found that the calculations diverged at a point approximately 1.5 core diameters downstream of the point at which the vortex was observed to break down.

1.2.3 Benjamin's Conjugate-Flow Theory

The conjugate-flow theory of Benjamin (1967) proposes that "vortex breakdown is fundamentally a transition from a uniform state of swirling flow to one featuring stationary waves of finite amplitude." (This theory expands on the original theory proposed by Benjamin (1962), which was limited to the treatment of waves of infinitesimal amplitude.) Benjamin's conjugate-flow theory, and the analysis with which the theory is constructed, share many features with the theory of weak bores. The theory is based on the assumption that the flow is axisymmetric and inviscid. However, the effects of viscous dissipation on the flow are modeled through the specification of a dissipation parameter, as will be described later in this section.

Benjamin's analysis treats swirling flows through pipes of constant radius and unbounded swirling flows. However, since the qualitative aspects of these flows differ only slightly, as will be seen in Chapter 3, the presentation of Benjamin's theory contained in this section will be limited to the context of flows through a pipe of constant radius.

The theory does not explicitly provide information concerning the structure of

the breakdown bubble. Instead, breakdown is modeled as an event that signals the crossover from one flow to a distinctly different flow. The flow downstream of breakdown (flow B) is represented as a small, but finite, perturbation to a columnar base flow, $\Psi_A(y)$, which exists upstream of breakdown (flow A). Flows A and B are referred to as "conjugate flows."

The base flow satisfies

$$\ddot{\Psi}_A = \dot{H}(\Psi_A) - \frac{1}{2y}\dot{I}(\Psi_A) \tag{1.12}$$

and is constrained to be supercritical, thus demanding that the eigenvalue of least value, γ_o^2, of the eigenproblem

$$\ddot{\phi}_A + \left(\frac{\gamma^2}{2y} + P(\Psi_A, y)\right)\phi_A = 0 \tag{1.13}$$

$$\phi_A(a) = \phi_A(0) = 0 \tag{1.14}$$

be positive. In (1.14) $a = \frac{1}{2}R^2$, where R is the radius of the pipe in which the flow is examined. The base flow is assumed to be sufficiently close to the critical state, however, so that γ_o^2 can be assumed to be small.

The streamfunction associated with flow B, $\psi(z, y)$, is written as

$$\psi(z, y) = \Psi_A(y) + \epsilon\varphi(z, y; \epsilon). \tag{1.15}$$

ϵ, a parameter which represents wave amplitude, is assumed small, but finite. Since mass flux is constant through the pipe, φ vanishes on the centerline of the vortex and at the pipe wall:

$$\varphi(z, 0) = \varphi(z, a) = 0. \tag{1.16}$$

The conjugate-flow theory is based primarily on three assumptions:

1. $\gamma_o^2 l^2 = O[1]$

2. $\epsilon^{1/2} l = O[1]$

3. $\int_0^a (H_A - H)dy = \epsilon^3 q \quad (q > 0)$,

where l is the length scale typifying axial changes of $\psi(z,y)$. The first assumption indicates that this length scale is of the same order as the length scale defined by γ_o (γ_o has the dimension of inverse length). In other words, the proximity of the base flow to the critical state is inversely related to the length scale typifying axial changes in flow B. The second assumption establishes the scale of wave amplitudes for which the theory is valid. The third assumption calls for a loss in the total head across the pipe because of viscous losses. The loss is third order in ϵ and is applied at the assumed position of breakdown. By applying the loss at a single point, the effect of viscosity on flow B is inferred through the magnitude of the dissipation parameter, q, but not explicitly accounted for in the equation governing flow B.

Benjamin defines the "flow force," S, as follows:

$$S \equiv 2\pi \int_0^a (p + \rho w^2) dy. \tag{1.17}$$

The flow force represents the sum of the axial momentum flux and the axial pressure force and is independent of axial position if the flow is contained within a frictionless pipe of constant radius and is free of external forces. An integral equation for φ is obtained by first substituting (1.15) into the equation

$$\frac{S_A - S}{2\pi\rho} = 0, \tag{1.18}$$

and then expanding the result to $O[\epsilon^3]$. Let

$$H_A \equiv H(\Psi_A), \tag{1.19}$$

$$I_A \equiv I(\Psi_A), \tag{1.20}$$

and define

$$K_n \equiv K_n(\Psi_A, y) = \frac{d^n}{d{\Psi_A}^n}(-H_A + \frac{1}{2y} I_A). \tag{1.21}$$

Then, to $O[\epsilon^3]$,

$$\int_0^a \left((H(\psi) - H_A) - \frac{1}{2y}(I(\psi) - I_A) \right) dy = -\epsilon^3 q$$

$$-\int_0^a \left(\epsilon K_1\varphi + \frac{1}{2}\epsilon^2 K_2\varphi^2 + \frac{1}{6}\epsilon^3 K_3\varphi^3\right) dy. \tag{1.22}$$

After noting that (1.12) yields

$$\int_0^a \left(\ddot{\Psi}_A + K_1\right)\varphi dy = 0, \tag{1.23}$$

or

$$\int_0^a \left(K_1\varphi - \dot{\Psi}_A\varphi_y\right) dy = 0, \tag{1.24}$$

(1.18) becomes, to $O[\epsilon^3]$,

$$-\epsilon^3 q + \frac{1}{2}\epsilon^2 \int_0^a \left(\varphi_y^2 - \frac{1}{2y}\varphi_x^2 - K_2\varphi^2\right) dy - \frac{1}{6}\epsilon^3 \int_0^a K_3\varphi^3 dy = 0. \tag{1.25}$$

The integral equation (1.25) is solved by assuming that φ takes the form

$$\varphi(z,y) = g(\tilde{z})\Phi(y) \quad (\tilde{z} = \epsilon^{1/2}z), \tag{1.26}$$

where $\Phi(y)$ is the normalized eigenfunction that solves the equation

$$\ddot{\Phi} + P_C\Phi = 0, \tag{1.27}$$

and $\tilde{z}$ is a scaled axial coordinate ($\dot{g} = O[1]$; cf. assumption 2). P_C is a function evaluated at the *critical state*:

$$P_C = P_C(\Phi_C, y) = -\ddot{H}_C(\Phi_C) + \frac{1}{2y}\ddot{I}_C(\Phi_C), \tag{1.28}$$

which could be obtained by adjusting a physical parameter, such as the vortex strength, in such a way that the supercritical base flow is made critical. Benjamin showed that

$$P_C = P_A + \epsilon\zeta(y) = K_2 + \epsilon\zeta(y), \tag{1.29}$$

where $\zeta(y)$ is a function of $O[1]$.

After noting that $\varphi_z^2 = \epsilon\dot{g}^2$, and

$$\int_0^a \left(\dot{\Phi}^2 - (K_2 + \epsilon\zeta)\Phi^2\right) dy = 0, \tag{1.30}$$

(1.25) is found to reduce to (all terms are $O[\epsilon^3]$)

$$E\dot{g}^2 = Fg^2 - Gg^3 - 2q \equiv \Sigma(g,q), \tag{1.31}$$

where

$$E \equiv \frac{1}{2}\int_0^a \frac{\Phi^2}{y}dy > 0, \tag{1.32}$$

$$F \equiv \int_0^a \zeta\Phi^2 dy > 0, \tag{1.33}$$

$$G \equiv \frac{1}{3}\int_0^a K_3\Phi^3 dy. \tag{1.34}$$

Benjamin observed that the solutions of (1.31) fall into three classes. Assuming $G > 0$ (if $G < 0$, the roots of $\Sigma = 0$ change sign but the physical description remains unchanged), one class of solutions is defined for $0 < q < 2F^3/27G^2$. When q is specified to lie in this range, there are two positive roots and one negative root of $\Sigma(g,q) = 0$. Between the two positive roots $\Sigma > 0$, while $\Sigma < 0$ at other points for which $g > 0$. If g is initially positive, then the solution, $g(\tilde{z})$, is constrained to lie between the two positive roots and oscillates between these roots as $\tilde{z}$ varies. Note that $\dot{g}$ changes sign as the solution passes through either of the two roots. Thus, solutions in this class represent wave trains supported by the base flow. Benjamin obtained an analytical expression for the wave-train solutions involving the cnoidal function cn. Wave amplitude is proportional to the separation of the two roots. As q approaches 0, or as viscous losses diminish, the separation between the two positive roots increases. The root of lesser magnitude moves towards $g = 0$, while the root of greater magnitude moves in the direction of increasing g. Benjamin also observed that the wavelength of the solution increased without bound as q vanished.

When $q = 0$, $\Sigma(g,0) = 0$ has two distinct roots. A double root is located at $g = 0$, while the second root is positive. Benjamin found the solution for this special case to be

$$g(\tilde{z}) = \frac{F}{G}\mathrm{sech}^2\left(\frac{\tilde{z}}{2}\left(\frac{F}{G}\right)^{1/2}\right). \tag{1.35}$$

This solution is representative of a solitary wave with amplitude $\frac{F}{G}$ at $\tilde{z} = 0$. Note that $g(\tilde{z}) \rightarrow 0$ as $\tilde{z} \rightarrow \infty$, so that in this limit the base flow is regained.

The third class of solutions is defined by $q = 2F^3/27G^2$. When q achieves this value, a double root at $g = \frac{2F}{3G}$ is obtained. A third root is found to be negative. For all positive values of g, the function Σ is negative. Thus, the only admissible solutions are columnar flows with $g(\tilde{z}) = \frac{2F}{3G}$. These columnar solutions are conjugate to flow A in the sense originally described by Benjamin (1962).

In summary, Benjamin (1967) found three types of flows that are conjugate to flow A, the type of flow obtained dependent on the severity of the viscous losses imposed at breakdown. In the absence of losses, the conjugate flow is a solitary wave with maximum amplitude at the point of breakdown. When the dissipation is finite, but sufficiently small, the conjugate flow is a cnoidal wave, the amplitude and wavelength of which decrease as viscous forces increase in magnitude. At a limiting value of the dissipation parameter, q, the conjugate flow is a columnar flow. Beyond this limiting value, breakdown is not possible. Benjamin also found that flow A must be supercritical for a steady conjugate flow to exist except in the unusual case that there is an external agency acting to reduce the flow force, S. Thus, in the absence of this agency, a necessary condition for transition to a noncolumnar flow is that flow A be supercritical.

1.2.4 The Theory of Brown and Lopez

Like the conjugate-flow theory, the recent theory proposed by Brown and Lopez (1988) is based on the assumption that the flow is steady, inviscid and rotationally symmetric. Their analysis does not culminate in a description of the flow structure that would result from vortex breakdown, as is provided by the conjugate-flow theory, but does yield a necessary condition, distinct from the condition of supercritical flow, for the occurrence of breakdown.

The analysis begins with the equation

$$\eta = \frac{\Gamma(\psi)}{r}\frac{d\Gamma}{d\psi} - r\frac{dH}{d\psi}, \tag{1.36}$$

which is obtained by equating the right-hand sides of (1.1) and (1.2). If a particular fluid particle is considered, then the azimuthal vorticity associated with the particle will vary in a simple way with radial position, since ψ is a constant along the particle's trajectory. Equation (1.36) can thus be rewritten as

$$\eta(z) = A/\sigma(z) - \sigma(z)B, \tag{1.37}$$

where $r = \sigma(z)$ describes the radial position of the stream surface, $\psi = \psi_o$, on which the trajectory is assumed to lie, and where A and B are constants given by:

$$A = \Gamma(\psi_o)\dot{\Gamma}(\psi_o), \tag{1.38}$$

$$B = \dot{H}(\psi_o). \tag{1.39}$$

The analysis proceeds by assuming that at some axial station upstream of breakdown, the components of the velocity and vorticity vectors on the stream surface, $\psi = \psi_o$, are known. Brown and Lopez designated known quantities with an "o" subscript and expressed the constants A and B in terms of the known velocity and vorticity components by evaluating (1.37) at the upstream station. After introduction of the axial vorticity, ζ, A and B were found to be

$$A = \sigma_o\zeta_o\alpha_o \tag{1.40}$$

$$B = \frac{\eta_o}{\sigma_o}\left(\frac{\alpha_o}{\beta_o} - 1\right), \tag{1.41}$$

where α_o and β_o are defined as follows:

$$\alpha_o \equiv v_o/w_o, \tag{1.42}$$

$$\beta_o \equiv \eta_o/\zeta_o. \tag{1.43}$$

Brown and Lopez observed that α_o and β_o are, respectively, the tangents of the pathline and vortex line helix angles. (Note that the pathline, although helical, lies on the stream surface $\psi = \psi_o$.) With A and B known, (1.37) can be rewritten as

$$\frac{\eta}{\eta_o} = \frac{\sigma_o}{\sigma}\left(\frac{\alpha_o}{\beta_o}\right) - \frac{\sigma}{\sigma_o}\left(\frac{\alpha_o}{\beta_o} - 1\right). \tag{1.44}$$

Since approach flows leading to vortex breakdown in tubes are generally of a jet-like character (Faler and Leibovich (1977)), it is reasonable to take η_o positive. With the additional assumption, to be discussed presently, that $\sigma/\sigma_o > 1$, Brown and Lopez found that the necessary condition for η to become negative is

$$\alpha_o/\beta_o > 1. \tag{1.45}$$

They also found that when (1.45) is satisfied, the azimuthal vorticity of the particle decreases monotonically as σ increases from σ_o.

Brown and Lopez proposed that the mechanism leading to vortex breakdown is a "positive feedback" of the production of negative azimuthal vorticity. Their reasoning proceeded along two lines. First, since breakdown involves the generation of negative azimuthal vorticity in the vicinity of the breakdown bubble and since azimuthal vorticity is generally positive upstream of breakdown, then (1.45) is a condition that must be met by the upstream flow for breakdown to occur. Using (1.44) and (1.45) to explain the breakdown mechanism assumes, of course, that the mechanism is an inviscid one, a reasonable assumption, since for the types of flows under consideration, viscous forces are too weak to cause the rapid divergence of streamsurfaces associated with breakdown.

In the second line of reasoning, Brown and Lopez describe the feedback mechanism. Assuming that (1.45) is satisfied and that the flow is diverging at the upstream station, then the consequential reduction of azimuthal vorticity predicted by (1.44) acts to reduce the axial velocity in the vortex core. Through continuity, reduced axial velocity leads to increased radial velocity in the core and the further expansion of the ψ_o streamsurface. Increased expansion of the streamsurface closes the feedback loop, since this expansion, through (1.44), results in further decrease of azimuthal vorticity. Brown and Lopez show that the initial flow divergence at the upstream station in calculations performed by Lopez (1988) is caused by an imbalance in the Γ and H distributions imposed by the global configuration of

the flow. In other flows the initial divergence can be attributed to weak, viscous effects. This point will be discussed further in Section (4.1). Another perspective on the feedback mechanism proposed by Brown and Lopez is also provided in Section (4.1).

1.3 Outline of Study

There are three main objectives of this investigation. The first is to identify the circumstances that lead to the bursting of a trailing vortex. Two parameters are used to describe the vortex: vortex strength, V, and Reynolds number, Re. Solutions of the equations governing the spatial evolution of the vortex are computed over a wide range of values of both parameters so as to determine approximately the parameter space for which vortex bursting is observed. The second objective is to provide qualitative and quantitative descriptions of those flows in which bursting is observed to occur. This includes: the description of the flow upstream of the point at which the vortex bursts, the axial position of the burst point and the structure of the flow that develops as a consequence of the burst. The last objective is to contribute to an increased understanding of vortex breakdown by comparing computed results with theory. Three theories are treated: Hall's theory, using the boundary-layer approximation, Benjamin's conjugate-flow theory and the theory proposed by Brown and Lopez. This investigation expands on findings reported by Beran (1987).

The algorithm used in this work to compute solutions of the Navier-Stokes equations, Euler-Newton pseudo-arclength continuation (Keller (1977)), has many advantages over algorithms used in previous investigations, making possible the calculation of a large collection of solutions that exhibit a broad spectrum of physical behavior not previously observed. One advantage offered by the algorithm is the ability to compute solutions for very large Reynolds numbers. These solutions can then serve as tests of theories, such as Benjamin's conjugate-flow theory, based on the inviscid equations of motion. Solutions of the Navier-Stokes equa-

tions, for large Reynolds numbers, can also be used to determine the ability of the quasi-cylindrical equations, which are of boundary-layer type, to predict the occurrence and position of vortex breakdown. Solutions are obtained for Reynolds numbers exceeding 20,000, or about two orders-of-magnitude greater than that attempted prior to Beran (1987). Solutions are computed using a central-difference approximation to the governing equations, ensuring that artificial viscosity is not introduced in the calculations.

Another significant advantage of the algorithm is that it enables changes in solution behavior to be readily determined as a specified parameter is varied. This ability is due to the efficiency with which solutions can be computed for different values of the specified parameter. For example, with Reynolds number fixed at some chosen value, solutions can be efficiently computed for many different values of vortex strength. The algorithm can then be used to "map" the solution space of the governing equations by alternately varying both Reynolds number and vortex strength. If solutions are represented by some appropriate scalar variable, such as kinetic energy, then these maps become surfaces in a three-dimensional space defined by Reynolds number, vortex strength and the scalar variable. Furthermore, the algorithm can find nonunique solutions of the governing equations, which in many cases are manifested as folds of the solution surface. Indeed, nonunique solutions were found in several cases, as described in Chapter 3, and may be of great importance to a better understanding of vortex breakdown. It is unlikely that such solutions could be computed using the methods with which the phenomenon of vortex breakdown has previously been studied.

Two flow models used to investigate vortex bursting are presented in Chapter 2. The assumptions, leading to a set of governing equations and boundary conditions for each model, are discussed. The first model, the Navier-Stokes model, is similar to that examined by Grabowski (1974). The continuum equations of this model, consisting of the steady-state Navier-Stokes equations and appropriate boundary conditions, are cast in finite-difference form and collocated into a system of non-

linear algebraic equations. The technique by which these discrete equations are solved to yield solutions of the steady-state problem is discussed in detail in Appendix B. The continuum equations of the alternate model, the quasi-cylindrical model, are derived in various forms in Appendix A, and cast in finite-difference form in Appendix E. The technique by which these discrete equations are solved is also treated in Appendix E.

In Chapter 3, solutions of the discrete equations of the Navier-Stokes model are presented. Solutions are obtained over a wide range of Reynolds numbers and vortex strengths. With these solutions, the important observation is made that an isolated vortex can change state. The upstream state is characterized by viscous decay of the vortex core, while the downstream state is characterized by large-amplitude, spatial oscillations of core radius. The point at which the vortex is defined to change state is termed the "transition point." This term is used in favor of "burst point," since it describes more accurately the process of transition between two states. The process of transition was first observed by Beran (1987). The transition point is marked by a rapid increase of core radius and a rapid decrease of axial velocity in the vortex core.

In total, four states are identified. The first state is that of slow, viscous decay, mentioned above. The remaining three states are classifications of the oscillatory flow. Those oscillatory flows not involving reversed flow are categorized as one state, while those involving small, symmetric bubbles of reversed flow are categorized as another state. Finally, for sufficiently large V, large bubbles of reversed flow are found, which are detached or nearly detached from the vortex axis, and which break the symmetry of the oscillatory flow. These flows are categorized as the fourth state and have been the focus of numerical investigations by Grabowski (1974) and Hafez et al. (1987). However, the relationship between this state and flows in the other three states has not been investigated previously.

The Navier-Stokes model is also modified slightly in Chapter 3 to yield solutions for the problem of flow through a frictionless pipe. These solutions are then

compared with a time sequence of solutions computed by Brown and Lopez (1988).

Solutions of the discrete equations of the quasi-cylindrical model are presented in Chapter 4. These solutions are compared with solutions of the discrete equations of the Navier-Stokes model. It is found that the quasi-cylindrical equations are an accurate approximation of the Navier-Stokes equations in the region of the flow upstream of the transition point. It is also found that the point at which the quasi-cylindrical equations fail lies downstream of the transition point predicted by the Navier-Stokes equations. Furthermore, failure of the quasi-cylindrical equations is found to serve as a necessary and sufficient condition for the existence of the transition point.

Conclusions based on the results of this work are stated in Chapter 5. The theories of Hall, Benjamin and Brown and Lopez are also discussed in light of the observations made in this investigation.

Chapter 2

Two Models for the Study of Trailing Vortex Bursting

In this chapter, two models for the study of the bursting of trailing vortices are described. These are:

1. Navier-Stokes model

2. quasi-cylindrical model.

The Navier-Stokes model provides the basis for accurate simulations of vortex bursting (relative to the assumptions common to both models as described in Section (2.1)), leading to predictions of burst position and structure. The Navier-Stokes model also allows the effect of viscosity on the behavior of the approach flow (flow upstream of the burst point). The quasi-cylindrical model leads to very efficient, numerical simulations of approach flows, but the position of the burst point is not accurately reproduced because the model equations do not account for upstream propagation of the breakdown structure. As will be shown in Chapter 4, the failure of the quasi-cylindrical equations is, however, a necessary and sufficient condition for vortex bursting.

The first section in this chapter summarizes the assumptions on which both models are based. It is followed by a presentation of the field equations and corresponding boundary conditions appropriate for each model. In the last section, the procedure by which the continuum equations of the Navier-Stokes model are cast in finite-difference form is outlined.

2.1 Model Assumptions

The primary type of flow investigated in this work is the evolution of a trailing vortex in the wake of a lifting surface. A depiction of this flow situation is shown in Figure (2.1), in which a trailing vortex exists in the wake of a delta wing at angle of attack with respect to a uniform, oncoming flow. This study will be restricted to the examination of vortex evolution in a cylindrical region downstream of the lifting surface containing a portion, many core diameters in length, of the trailing vortex.

In each model, the flow is assumed to be steady and incompressible. Furthermore, the flow is assumed to be rotationally symmetric, or "axisymmetric," with an axis of symmetry aligned with the freestream flow and coincident with the vortex axis. Effects of vortex pair interaction are not accounted for — the vortex is assumed to evolve in isolation and is viewed as embedded in a uniform flow of infinite extent.

Again referring to Figure (2.1), let r, θ and z denote radial, azimuthal and axial position, respectively, and let u, v and w represent the radial, azimuthal and axial velocity components, respectively. The upstream surface, S1, of the cylindrical region is defined to be located at $z = 0$, while the downstream surface, S3, is defined to be located at $z = Z$. A third surface, S2, of radius R and centered about the vortex, completes the bounding of the region.

As the assumed flow is rotationally symmetric, flow properties depend only on r and z. Thus, the equations governing the flow can be solved using a two-dimensional computational domain. This domain will be represented by $\Re$ and is shown in Figure (2.2). $\Re$ is bounded by the symmetry axis, denoted by S4, and three other lines, S1, S2 and S3, corresponding to the projections of the bounding surfaces of the cylindrical region on the computational domain.

Azimuthal and axial velocity profiles typical of trailing-vortex flows are depicted in Figure (2.3). In this figure, W represents freestream velocity and δ corresponds

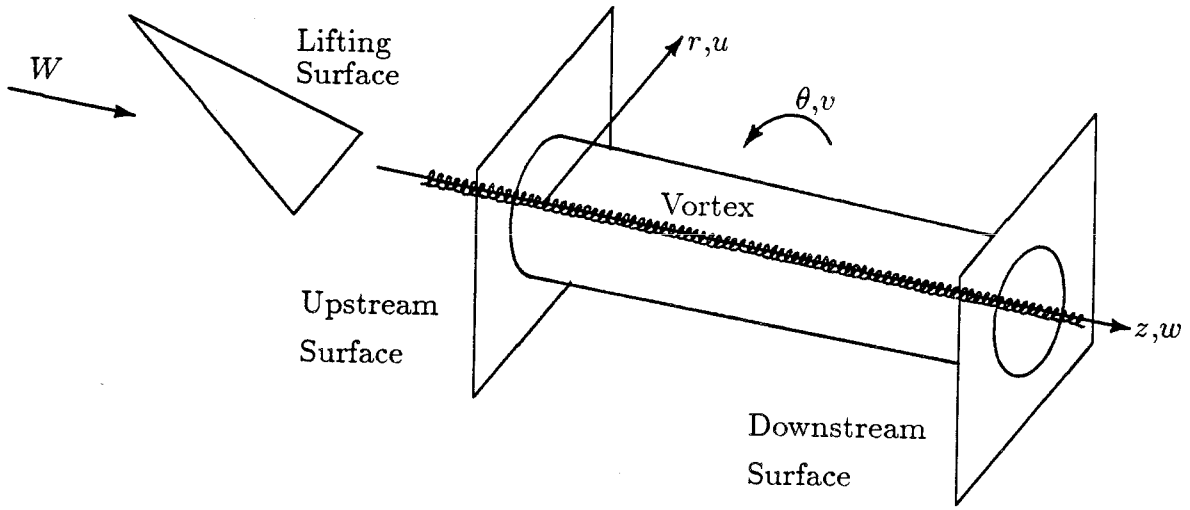

Figure 2.1 Characterization of flow

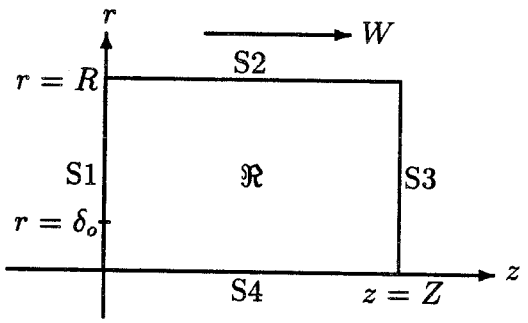

Figure 2.2 Geometry of computational domain

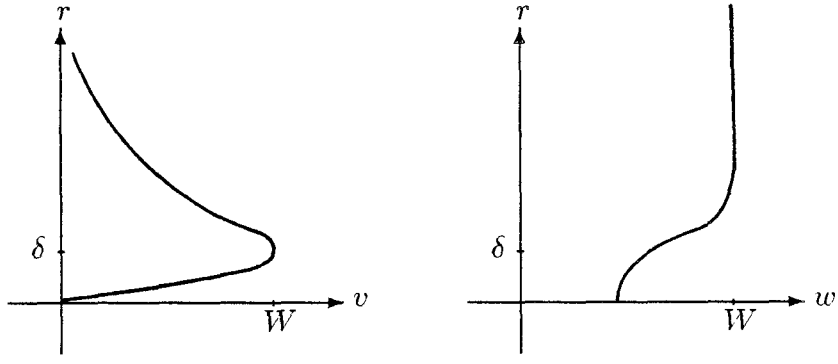

Figure 2.3 Velocity profiles typical of trailing vortices

to the radius of the vortex core. The vortex core is characterized by solid-body rotation ($v \sim r$), while outside the core, $v \sim 1/r$ and $w \sim W$ as $r \to \infty$. In cases of interest, peak swirl velocity is of the same order of magnitude as W.

At the inflow surface, the azimuthal and axial velocity profiles are assumed to be known and to be similar in form to those profiles shown in Figure (2.3).

The quasi-cylindrical model assumes viscous forces to be sufficiently weak so that the axial gradient of a flow variable is negligible relative to the radial gradient of the flow variable. Consequently, vortex evolution is assumed to occur on a much larger length scale than that defining the vortex core. The main implication of the quasi-cylindrical assumption is that the resulting equations are parabolic, where the streamwise direction is the timelike direction.

The Navier-Stokes model does not make any assumptions beyond those stated above except for the specification of quasi-cylindrical flow at the inflow surface. As will be seen in Chapter 3, this is not a necessary assumption and can be replaced with a condition on the radial velocity at the inflow surface. However, approach flows generally can be approximated as quasi-cylindrical (Leibovich (1978)). The enforcement of quasi-cylindrical flow at the inflow surface is simply an effort to reproduce conditions that lead to the development of breakdown within the bounds of the computational domain.

With the arguable exception of the assumption of rotational symmetry, the assumptions of the Navier-Stokes model are consistent with the main goal of this work, which is to learn more about the mechanism(s) responsible for vortex breakdown. It is well documented (Sarpkaya (1971); Faler and Leibovich (1977); and Leibovich (1978)) that to varying degrees, vortex breakdown is essentially non-axisymmetric in structure. However, numerical simulations (Grabowski (1974); Beran (1987); Hafez et al. (1987); Brown and Lopez (1988); and others) have demonstrated that the bubble-like breakdown structures observed in experiment (Sarpkaya (1971A)) also occur in strictly axisymmetric flows. Since the mechanism for breakdown in these axisymmetric flows is not well understood, a better understanding would most likely benefit any investigation of vortex breakdown as a three-dimensional phenomenon.

2.2 Governing Equations

The governing equations corresponding to each of the models described above are presented in nondimensional form in this section. Scales appropriate for the nondimensionalization of the governing equations are the radius of the vortex core at the inflow boundary, δ_o, for length and the freestream velocity, W, for velocity.

2.2.1 Navier-Stokes Equations

Under the assumptions of a steady, incompressible, rotationally symmetric flow, the nondimensional Navier-Stokes equations are:

$$\psi_{zz} + \psi_{rr} - \psi_r/r = -r\eta \tag{2.1}$$

$$\frac{\psi_r \Gamma_z}{r} - \frac{\psi_z \Gamma_r}{r} = \frac{1}{\mathrm{Re}} \left(\Gamma_{zz} + \Gamma_{rr} - \Gamma_r/r \right) \tag{2.2}$$

$$\frac{\psi_r \eta_z}{r} - \frac{\psi_z \eta_r}{r} + \frac{\psi_z \eta}{r^2} = \frac{2\Gamma\Gamma_z}{r^3} + \frac{1}{\mathrm{Re}} \left(\eta_{zz} + \eta_{rr} + \eta_r/r - \eta/r^2 \right), \tag{2.3}$$

where $\mathrm{Re} = W\delta_o/\nu$. Equations (2.1—2.3) are elliptic. Streamfunction, ψ, circulation (divided by 2π), Γ, and the azimuthal component of vorticity, η, are related to the velocity components as follows:

$$u = -\frac{\psi_z}{r} \tag{2.4}$$

$$w = \frac{\psi_r}{r} \tag{2.5}$$

$$\Gamma = rv \tag{2.6}$$

$$\eta = u_z - w_r. \tag{2.7}$$

Henceforth, all variables will be assumed to be in nondimensional form.

2.2.2 Quasi-Cylindrical Equations

The equations resulting from the assumption of quasi-cylindrical flow, derived in Appendix A, will be referred to as the QC equations. In nondimensional form they are:

$$\psi_{rr} - \psi_r/r = -r\eta \tag{2.8}$$

$$\frac{\psi_r \Gamma_z}{r} - \frac{\psi_z \Gamma_r}{r} = \frac{1}{\mathrm{Re}} \left(\Gamma_{rr} - \Gamma_r/r\right) \tag{2.9}$$

$$\frac{\psi_r \eta_z}{r} - \frac{\psi_z \eta_r}{r} + \frac{\psi_z \eta}{r^2} = \frac{2\Gamma\Gamma_z}{r^3} + \frac{1}{\mathrm{Re}} \left(\eta_{rr} + \eta_r/r - \eta/r^2\right), \tag{2.10}$$

where

$$\eta \equiv -w_r. \tag{2.11}$$

Equations (2.8—2.10) are parabolic, with the streamwise direction serving as a timelike coordinate.

2.3 Boundary Conditions

The boundary conditions necessary to complement the governing equations are different, of course, for each of the two models, since the model equations are of different type (i.e., elliptic versus parabolic). The Navier-Stokes model requires the specification of boundary conditions on ψ, η and Γ on all four sides of the

computational domain, $\Re$. The quasi-cylindrical model requires conditions to be specified on the symmetry axis and boundaries S1 and S2.

In both models the streamfunction and circulation profiles are specified at the inflow surface. The profiles are assumed to have the following functional forms:

$$\psi_o(r) = \frac{1}{2}r^2 + \left(\frac{a}{2}\right)\left(1 - e^{-r^2}\right) \tag{2.12}$$

$$\Gamma_o(r) = V\left(1 - e^{-r^2}\right) \quad \text{or} \tag{2.13}$$

$$\Gamma_o(r) = \begin{cases} V & r \geq 1 \\ Vr^2(2 - r^2) & r < 1, \end{cases} \tag{2.14}$$

and are related to the following axial and azimuthal velocity profiles:

$$w_o(r) = 1 + ae^{-r^2} \tag{2.15}$$

$$v_o(r) = \frac{V}{r}\left(1 - e^{-r^2}\right) \quad \text{or} \tag{2.16}$$

$$v_o(r) = \begin{cases} V/r & r \geq 1 \\ Vr(2 - r^2) & r < 1. \end{cases} \tag{2.17}$$

The "vortex strength," V, is equal to the circulation of the vortex in the far field. The parameter a represents the difference between the centerline axial velocity and the freestream axial velocity. The axial velocity profile in Figure (2.3) is an example of $w_o(r)$ for $a < 0$.

Two different circulation profiles were used so that results could be compared with those of previous investigations.

2.3.1 Navier-Stokes Model Boundary Conditions

The boundary conditions used in this work for the Navier-Stokes model are presented below and are essentially the same as those used by Grabowski (1974); Krause et al. (1983); and Hafez et al. (1987). There are some differences, however, and these will be discussed in the following paragraphs.

Navier-Stokes Model Boundary Conditions

- Boundary S1: $\psi(0,r) = \psi_o(r)$, $\Gamma(0,r) = \Gamma_o(r)$, $u(0,r) = 0$ or $\eta(0,r) = -\frac{1}{r}(\psi_{o_{rr}}(r) - \psi_{o_r}(r)/r)$

- Boundary S2: $\Gamma(z,R) = \Gamma(0,R)$, $\eta(z,R) = \eta(0,R)$, $\psi_r(z,R) = \psi_r(0,R)$

- Boundary S3: $\psi_z(Z,r) = \Gamma_z(Z,r) = \eta_z(Z,r) = 0$

- Boundary S4: $\psi(z,0) = \Gamma(z,0) = \eta(z,0) = 0$

The condition on inflow vorticity is complicated by the dependence of vorticity on the axial gradient of u, which is not generally known at the upstream boundary. This problem has been dealt with in two ways by previous investigators for the case of $w(0,r) = 1$ $(a = 0)$. Krause et al. (1983) enforced a Dirichlet condition, $\eta_o(r) = 0$, on vorticity at the inflow boundary. This condition implies that $w_{zz} = 0$ at that surface, and thus allows the inflow to have an axial gradient in the axial velocity. Krause et al. obtained steady-state solutions to the time-dependent form of (2.1—2.3) in the absence of reversed axial flow, but were unable to find steady-state or time-periodic solutions with reversed flow. Hafez et al. (1987) applied an implicit condition on inflow vorticity, $\eta(0,r) = -\frac{1}{r}\psi_{zz}(0,r)$, which follows from (2.1), assuming $u(0,r) = 0$. $\psi_{zz}(0,r)$ was approximated with a one-sided, finite-difference expression using streamfunction values within $\Re$.

Grabowski (1974) solved the Navier-Stokes equations in velocity-pressure form, using the artificial compressibility method, and obtained equilibrium solutions with reversed flow. The only significant difference between the boundary conditions used by Grabowski and those by Krause et al. (1983) was that Grabowski, like Hafez et al. (1987), chose the radial velocity at the upstream boundary to be identically zero, implying that $w_z = 0$ at that boundary instead of $w_{zz} = 0$.

For inflows that are strongly parabolic, i.e., flows with small radial velocities and small axial gradients, the equation $\eta = -w_r$ provides an accurate approximation to the profile of inflow vorticity. The past inability to compute reasonable solutions of the Navier-Stokes equations for such an inflow vorticity condition appears to have

been due to the development of vortex breakdown just downstream of the inflow boundary, a situation that violates the assumption of a quasi-cylindrical inflow. In these cases, proximity of breakdown to the inflow surface was caused by the specification of a "strong" vortex ($V \approx 1$). As will be seen in the next chapter, it is necessary to decrease the vortex strength or increase the centerline axial velocity ($a > 0$) to cause breakdown to occur farther downstream from the inflow surface, so that conditions at this surface can be approximated as quasi-cylindrical.

Since it is apparent that the behavior of the trailing vortex is sensitive to the choice of upstream boundary condition on vorticity, the approaches of both Krause et al. and Grabowski are examined in this work.

For R sufficiently large, the flow on S2 is essentially the same as the freestream. However, a gradient condition is imposed on ψ at that boundary to allow fluid transfer across S2 and is necessary for conservation of mass, since decay of the trailing vortex leads to a deficit of mass flux across axial stations, $z =$ constant.

The axial boundary conditions ensure bounded behavior on the axis, and the downstream boundary conditions are standard outflow conditions. More accurate outflow conditions, derived by parabolizing (2.1—2.3), were experimented with, but did not lead to solutions appreciably different from solutions obtained with the downstream boundary conditions shown above, as long as computed flow gradients near the outflow boundary were small.

2.3.2 Quasi-Cylindrical Model Boundary Conditions

The boundary conditions for the quasi-cylindrical model are summarized below and are the same as those of the Navier-Stokes model, except that downstream boundary conditions are not enforced, and the inflow is assumed to be quasi-cylindrical.

Quasi-Cylindrical Model Boundary Conditions

- Boundary S1: $\psi(0,r) = \psi_o(r)$, $\Gamma(0,r) = \Gamma_o(r)$ $\eta(0,r) = -\frac{1}{r}(\psi_{orr}(r) -$

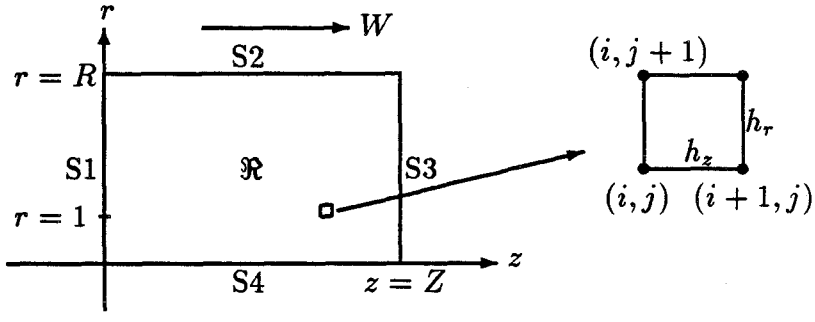

Figure 2.4 Discretized computational domain

$\psi_{o_r}(r)/r)$

- Boundary S2: $\Gamma(z,R) = \Gamma(0,R)$, $\eta(z,R) = \eta(0,R)$, $\psi_r(z,R) = \psi_r(0,R)$
- Boundary S4: $\psi(0,z) = \Gamma(0,z) = \eta(0,z) = 0$

2.4 Discretization of Computational Domain

$\Re$ is discretized by a rectangular mesh with constant node spacings h_z and h_r in the z and r coordinate directions, as illustrated in Figure (2.4). Flow variables (ψ, Γ, η) are evaluated at node points (i,j), where $1 \leq i \leq I$, $1 \leq j \leq J$, $z = (i-1)h_z$, and $r = (j-1)h_r$. The unknown values of (ψ, Γ, η) at each node point are collocated into a single vector, $\underline{x}$, in the following order:

$$\underline{x} = (\psi_1, \Gamma_1, \eta_1, \psi_2, \Gamma_2, \eta_2, ..., \psi_k, \Gamma_k, \eta_k, ..., \psi_N, \Gamma_N, \eta_N)^T,$$

where $k = (i-1)J + j$ and $N = IJ$.

2.5 Discretization of Navier-Stokes Equations

The procedure by which the governing equations of the Navier-Stokes model are discretized is described in this section. A different procedure is involved in discretizing the QC equations and will be discussed in Appendix E.

Continuum derivatives are approximated with second-order accurate, central-difference operators. The finite-difference representations of (2.1), (2.2) and (2.3) are written, respectively, as

$$P_h(\psi_{(i,j)}, \eta_{(i,j)}) = 0, \tag{2.18}$$

$$G_h(\psi_{(i,j)}, \Gamma_{(i,j)}) = 0, \tag{2.19}$$

$$E_h(\psi_{(i,j)}, \Gamma_{(i,j)}, \eta_{(i,j)}) = 0. \tag{2.20}$$

P_h, G_h, and E_h are discrete operators and (2.18—2.20) are to be satisfied at all interior node points. At boundary nodes, the discrete equations are replaced with finite-difference representations of the boundary conditions.

Discrete equations are collocated into an array of equations, $\underline{F}$, organized in the same way as $\underline{x}$:

$$\underline{F} = (P_{h1}, G_{h1}, E_{h1}, ..., P_{hk}, G_{hk}, E_{hk}, ..., P_{hN}, G_{hN}, E_{hN})^T .$$

For a particular mesh geometry Re, V and a are free parameters of the discrete Navier-Stokes model. The dependence of $\underline{F}$ on these parameters and the solution vector, $\underline{x}$, is represented in the set of discrete equations,

$$\underline{F}(\underline{x}; \mathrm{Re}, V, a) = 0. \tag{2.21}$$

2.6 Discretization of Boundary Conditions

The manner in which boundary conditions of the Navier-Stokes model are put into discrete form is described in this section. The discretization of boundary equations of the quasi-cylindrical model is discussed in Appendix E.

The gradient condition on ψ on S2 was approximated to second-order accuracy with a one-sided, finite-difference expression:

$$3\psi(i,J) - 4\psi(i,J-1) + \psi(i,J-2)$$

$$= 3\psi_o(J) - 4\psi_o(J-1) + \psi_o(J-2). \tag{2.22}$$

Gradient outflow conditions were approximated to first-order accuracy, also with one-sided, finite-difference expressions. Outflow conditions of second-order accuracy were experimented with, but did not lead to solutions appreciably different from solutions obtained with the outflow conditions of first-order accuracy. First-order accurate, finite-difference expressions were used to minimize the bandwidth of the equations resulting from the linearization of (2.21).

The inflow condition, $u(0,r) = 0$, provides an implicit condition on inflow vorticity. For this case (2.4), gives

$$-\frac{1}{r}\psi_z(0,r) = u(0,r) = 0, \tag{2.23}$$

or

$$\psi_z(0,r) = 0. \tag{2.24}$$

Equation (2.24) is discretized using a central-difference operator, and is combined with (2.18), to give at nodes on the inflow boundary

$$-r\eta_{(1,j)} = \frac{\psi_{(1,j+1)} + \psi_{(1,j-1)} - 2\psi_{(1,j)}}{h_r^2}$$

$$+ \frac{2(\psi_{(2,j)} - \psi_{(1,j)})}{h_z^2} - \frac{\psi_{(1,j+1)} - \psi_{(1,j-1)}}{2h_r}. \tag{2.25}$$

Chapter 3

Solutions of the Navier-Stokes Equations

In Chapter 2, a model for trailing vortices incorporating the Navier-Stokes equations was proposed which, after discretization of the problem, led to a system of nonlinear algebraic equations, (2.21). Solutions of (2.21) were computed for a variety of values of the Reynolds number, Re, and the vortex strength, V, and the results are presented in this chapter. Solutions paths were computed through the procedure outlined in Appendix B. Solution paths previously computed by Beran (1987) with the same trailing vortex model are also reported.

The first set of computations were performed to determine the sensitivity of solutions of (2.21) to variations in computational grid geometry for fixed values of the free parameters. These calculations provided the basis for choosing grid geometries for cases with different values of the free parameters. The next set of computations were aimed at obtaining solutions that could be compared with results computed by previous investigators. It was found that results compared favorably with past work.

Then, solution paths were computed using continuation in both Re and V, with $a = 0$. Typical results are presented and indicate that a trailing vortex of sufficient circulation will undergo a transition from an upstream state of slow, diffusive decay to a downstream state marked by large-amplitude, spatial oscillations of vortex radius and centerline axial velocity. Nonunique solutions are also computed.

Finally, results of calculations of flow through a pipe (a flow model very similar to the Navier-Stokes model proposed in Chapter 2) are presented and compared

with recent work, involving the time-dependent Navier-Stokes equations, by Brown and Lopez (1988). It was found that transition could cause the formation of a small "bubble" of reversed flow if $a > 0$ and if the vortex was of sufficient circulation. Again, nonunique solutions were computed.

Calculations were performed on the NASA Ames Cray-XMP. A summary of code performance is also provided in this chapter.

3.1 Sensitivity to Computational Grid Geometry

Several computations were performed to determine the size of the computational domain and the level of discretization necessary to compute grid independent solutions. Re, V and a were fixed at 200, 1 and 0, respectively. This set of parameter values was chosen since it is a case that has been investigated previously, and a case in which reversed flow occurs. Grid geometry parameters, R, Z, h_r and h_z were individually varied to determine their effect on the solution of (2.21). On the inflow boundary, $u(r) = 0$ is assumed.

First, the number of nodes in the axial direction, I, was varied while the number of nodes in the radial direction, J, domain radius, R, and domain length, Z, were kept constant at 27, 2, and 20, respectively. Figure (3.1) shows plots of axial velocity on the axis ($r = 0$) versus axial position for three values of I. Reversed flow is observed from $z = 1.2$ to about $z = 1.6$. Results obtained with $I = 105$ and $I = 209$ appear to be identical, and thus axial-node spacing probably need not be less than $\frac{20}{104}$. The case with the coarsest discretization, $I = 53$, is in error in the region where the flow begins to accelerate downstream of breakdown and at $z \approx 4.0$, where the flow again decelerates. However, all three discretizations yield the same breakdown position (defined as the point at which the flow becomes reversed) and outflow axial velocity.

Next, domain length, Z, was varied, while J, R and axial-node spacing, h_z, were fixed at 27, 2 and $\frac{20}{104}$, respectively. Results are presented in Figure (3.2). The solutions obtained with $Z = 20$ and $Z = 40$ are in excellent agreement. The

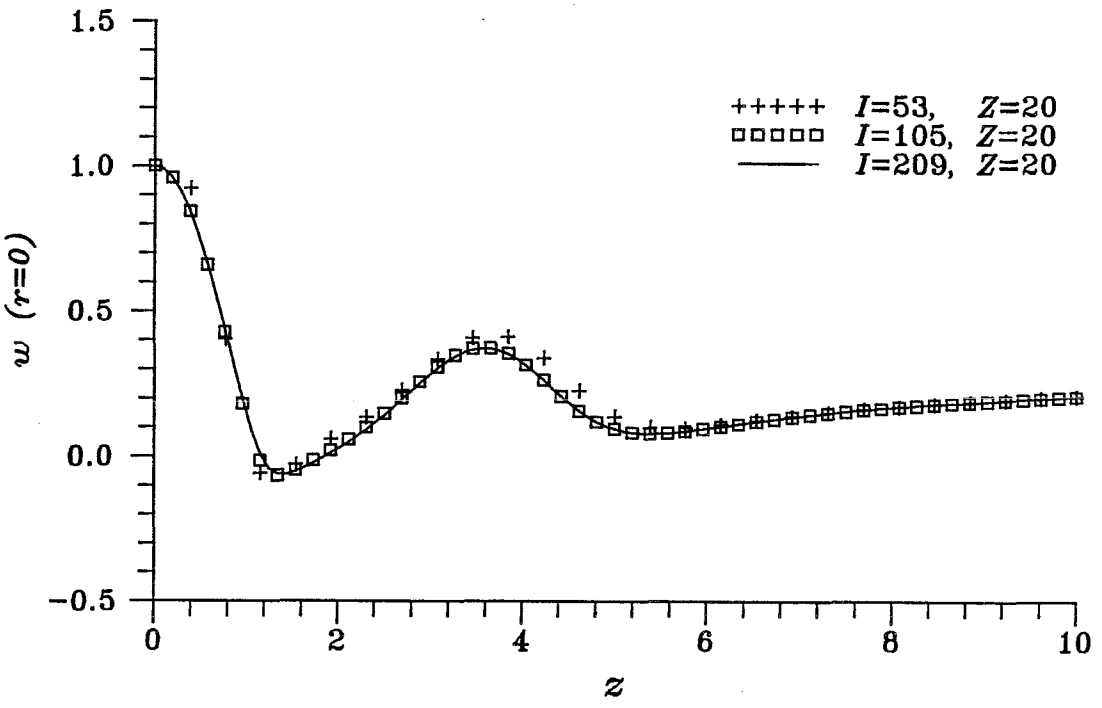

Figure 3.1 Effect of axial-node spacing on centerline axial velocity

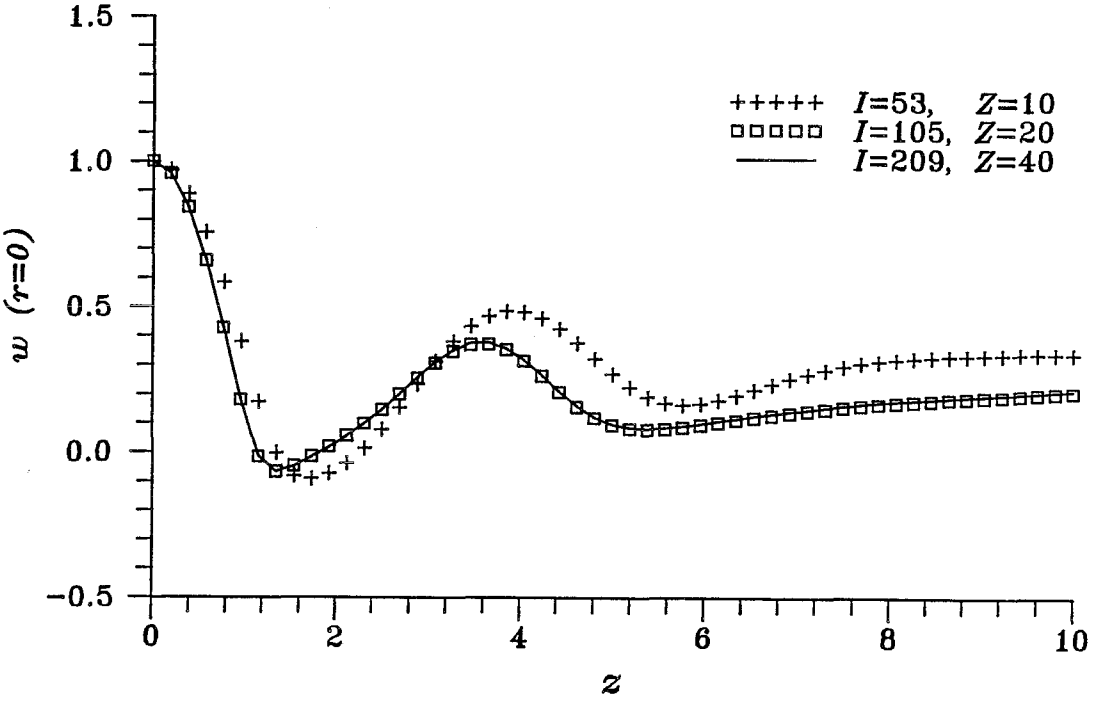

Figure 3.2 Effect of domain length on centerline axial velocity

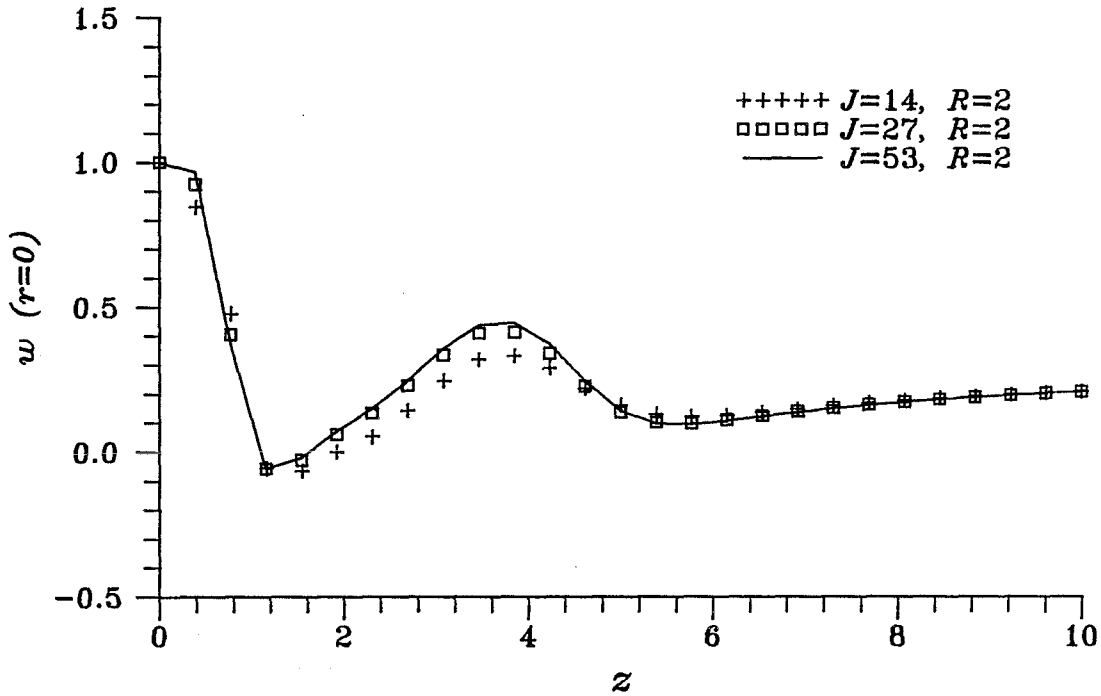

Figure 3.3 Effect of radial-node spacing on centerline axial velocity

solution obtained with the shortest domain, $Z = 10$, is quantitatively different from the other two solutions, yet similar qualitatively. For this choice of Reynolds number and vortex strength, a domain length of 20 is sufficient to obtain accurate solutions, but, as will be seen in Section (3.3.5), to obtain accurate solutions at higher Reynolds numbers, $Z > 20$ is required.

Sensitivity to node spacing in the radial direction, h_r, was examined by varying J while holding R, I and Z fixed at 2, 53 and 20, respectively. It was found above that a domain length of 20 yielded a solution independent of further increase of domain length. It was also found that for $J = 27$ and $Z = 20$, the solution for the case $I = 53$ was not independent of decrease in axial-node spacing. However, if for the case $I = 53$ a value of radial-node spacing is found such that the solution is independent of further decrease of radial-node spacing, then this should also be true for $I = 105$. Results for three different values of J are shown in Figure (3.3). The solutions with the two finest discretizations are in good agreement, although there are minor differences in centerline axial velocity near the inflow boundary

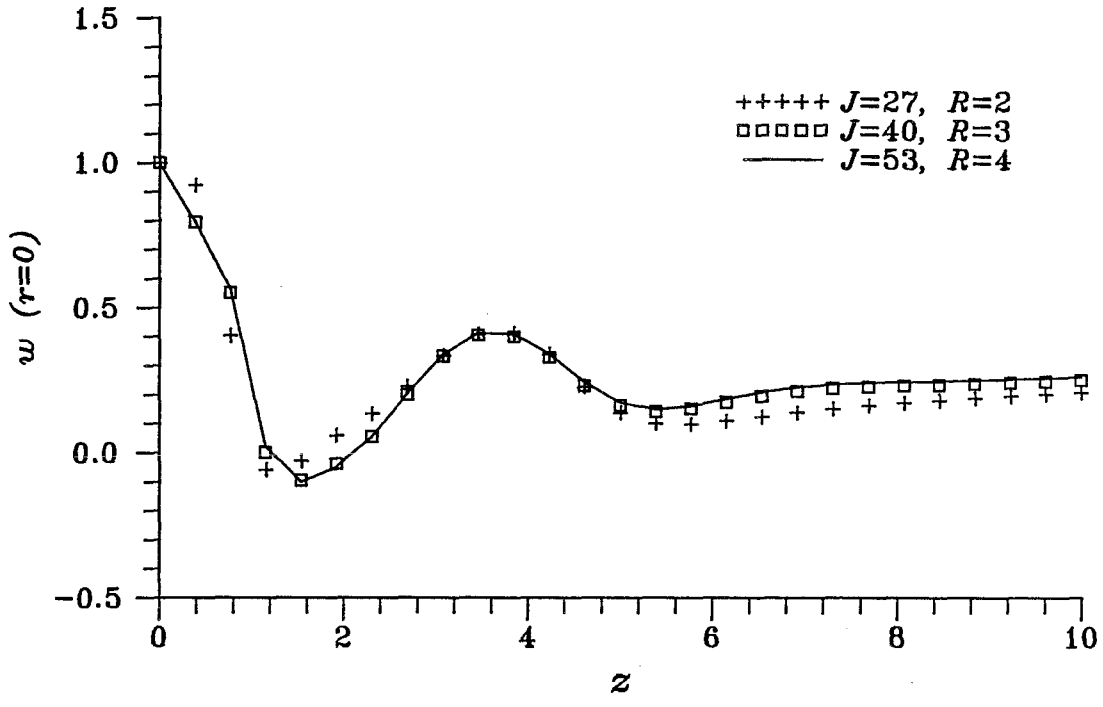

Figure 3.4 Effect of domain radius on centerline axial velocity

and in the vicinity of $z = 3.5$. The case with the coarsest discretization case, $J = 14$, agrees with the other two cases in the inflow and outflow regions but underestimates the recovery of the axial flow downstream of the reversed flow section. The results suggest that a radial-node spacing of $\frac{1}{13}$ is sufficient to define accurately the vortex burst. Predicted breakdown position and outflow velocity are the same in all three cases.

In the last set of computations, the domain radius, R, was varied, while h_r, I and Z were fixed at $\frac{1}{13}$, 53 and 20, respectively. Results are shown in Figure (3.4). The solution appears to be unaffected by increase of domain radius beyond 3.

The results reported above indicate that when $Re = 200$ and $V = 1.0$, solutions of (2.21) are independent of increase in computational domain size beyond $R = 3$ and $Z = 20$ and independent of increase in node number beyond $J = 40$ and $I = 105$.

The main difficulty in achieving fine-grid solutions was the large amount of computer memory needed to solve the linear systems of equations using Gaussian

elimination. For example, the computation of a solution to (2.21), for the case judged to be grid-insensitive, required 3.5 million words of computer memory, approximately the limit of main memory readily accessible on the computer on which calculations were performed.

When Reynolds number was specified to be much larger than 200, it was necessary to more than double the number of nodes in the axial direction to obtain smooth solutions (free of short-period, numerical noise). However, not enough computer memory was available to double the number of nodes in the axial direction *and* still have 40 nodes in the radial direction. Thus, for Reynolds number much larger than 200, solutions were computed on grids with a radial geometry of $R = 2$ and $J = 27$. It must be recognized that these solutions are not independent of increase in domain radius, as seen in Figure (3.4), but that these solutions should satisfactorily reproduce all the qualitative features of vortex evolution.

3.2 Comparison with Previous Work

The steady-state, spatial evolution of trailing vortices has been previously examined, using the Navier-Stokes equations, by Grabowski (1974); Hafez et al. (1986); Beran (1987); and Hafez et al. (1987). The flow was modeled in essentially the same way in each of the four studies, but there were significant differences in the way the governing equations were cast in finite-difference form and subsequently solved. Grabowski cast the governing equations in primitive variable form, approximated derivatives with central differences and used a nonuniform mesh with a finer discretization near the origin. The equations were integrated in time, using the artificial compressibility method of Chorin (1967), until convergence in time was achieved. Hafez et al. (1986) cast the equations in streamfunction, vorticity and circulation form, approximated derivatives with upwind differences and used a rectangular grid with constant node spacing. The equations were solved through an iterative relaxation technique. The approach of Beran (1987) is the subject of Chapter 2 and Appendix B. Virtually the same approach was taken by Hafez et

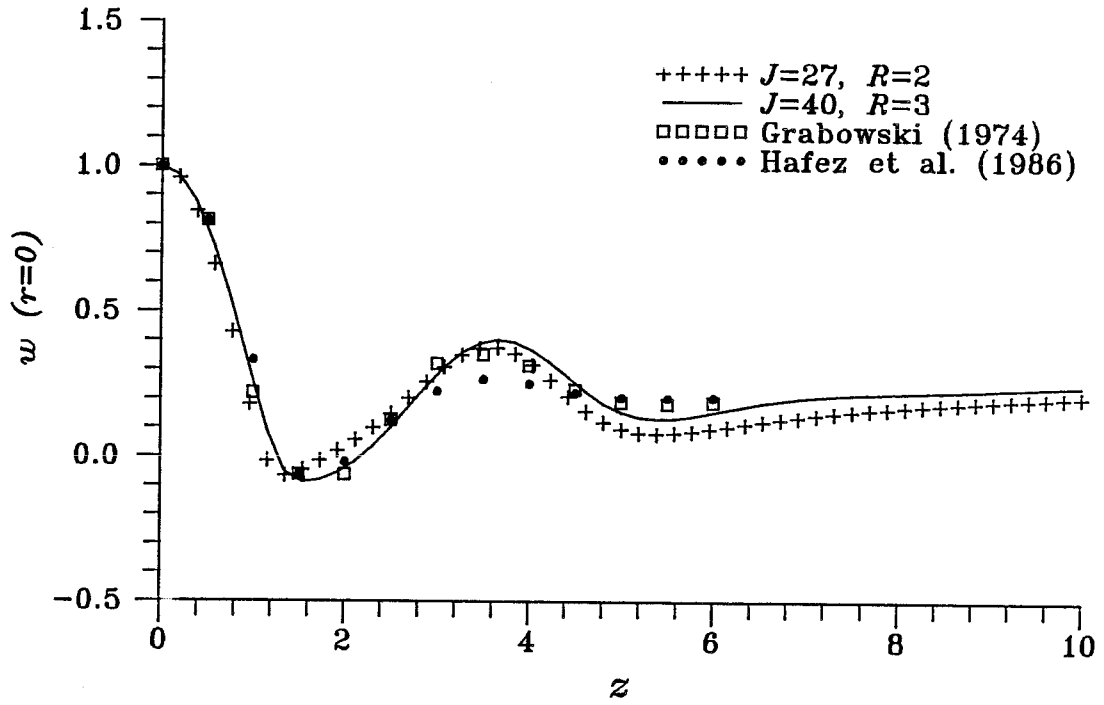

Figure 3.5 Comparison of centerline axial velocity profiles computed in three investigations for Re = 200, $V = 1.0$ and $Z = 20$

al. (1987).

Two solutions of (2.21) were computed by Beran, with $Z = 20$ and $I = 105$: one corresponding to $R = 2$ and $J = 27$ and the other corresponding to $R = 3$ and $J = 40$. It was found in Section (3.1) that a solution of (2.21) computed with the latter set of grid parameters would be insensitive to both grid refinement and grid enlargement, but that the former set of grid parameters would be used in the computation of solutions at higher Reynolds number.

Solutions are compared in Figures (3.5) and (3.6) for the case Re = 200 and $V = 1.0$, which was a case examined in each of the four investigations. Solutions computed with a domain length of 20 are compared in Figure (3.5). Computed data between the inflow boundary and about $z = 3$ are in good agreement. For $z > 3$, Hafez et al. (1986) predict a flattening of the profile of centerline axial velocity, possibly caused by their use of numerically diffusive, first-order accurate, difference operators. To a lesser extent, Grabowski's predicted axial velocity profile also flattens downstream of $z = 3$, a circumstance which could be attributed to

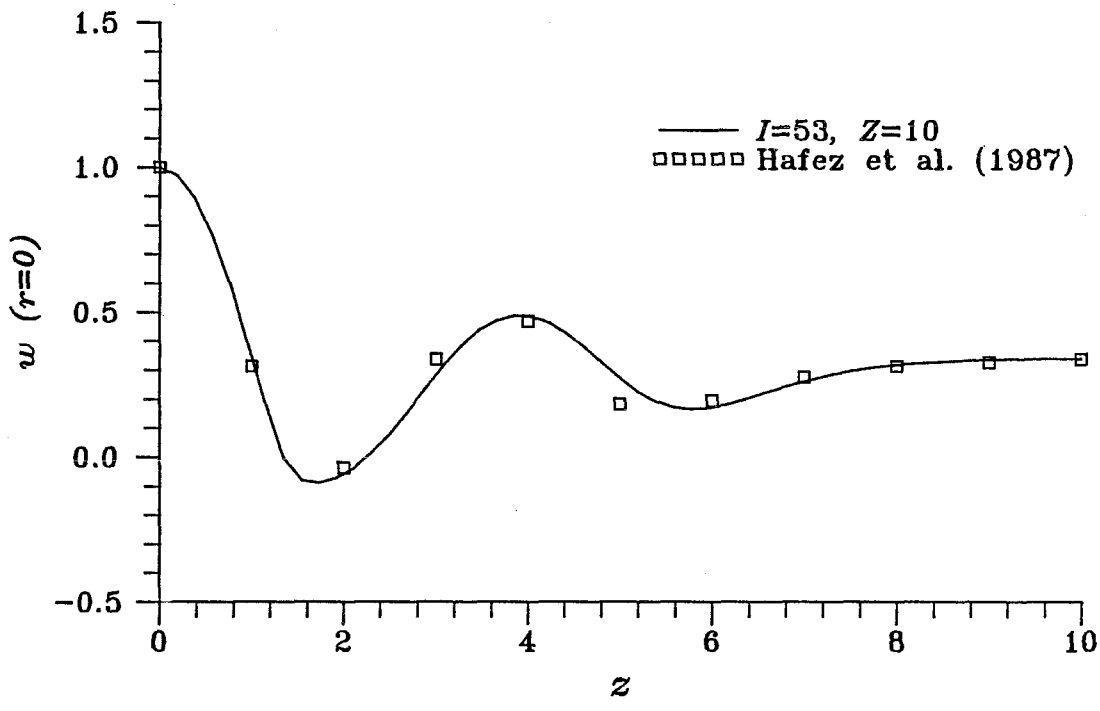

Figure 3.6 Comparison of centerline axial velocity profiles computed in two investigations for Re = 200, $V = 1.0$ and $Z = 10$

poorer grid refinement away from the domain origin. All results predict a local maximum in the centerline axial velocity around $z = 3.5$.

Solutions computed using a domain length of 10 are compared in Figure (3.6). The solutions are in good agreement over most of the domain, a fact that is not surprising, since solutions were obtained with essentially the same numerical algorithm. Results differ at $z \approx 5$; the error may be attributable to a difference in the way centerline axial velocity is computed, or to a difference in the grids employed in the two investigations.

3.3 Calculation of Solution Paths

Solution paths were computed for several different values of Reynolds number and vortex strength, assuming $a = 0$. These paths are the subject of this section. Solution paths were also computed using continuation in V, assuming that $a > 0$, for the problem of flow through a frictionless pipe. These solutions are discussed

in Section (3.6).

Out of the results presented in Section (3.3) come four main sets of observations. First, when Reynolds number is greater or equal to about 250 and V is increased from a small value ($V \leq 0.5$), a well-defined minimum in centerline axial velocity forms and moves upstream with further increase of V. When V is sufficiently large, the global minimum is trailed by other, less pronounced, local minima in centerline axial velocity. Upstream of the global velocity minimum, a pronounced change in the rate at which centerline axial velocity decays with axial position is observed. Referred to as "transition" in this work, the abrupt drop in centerline axial velocity marks the departure of the flow from a state involving slow decay of centerline axial velocity to a state involving large-amplitude, spatial oscillations of centerline axial velocity. A "transition point" is precisely defined in Section (3.4). As V increases, the transition point moves upstream and the minimum value of centerline axial velocity decreases.

Second, when $a = 0$ and when the minimum value of centerline axial is negative, or slightly positive, the transition point is at, or near the inflow boundary. As the transition point approaches the inflow boundary ($V \approx 0.8$), flow behavior with further increase of V depends on the Reynolds number and on the choice of boundary condition on inflow vorticity (see Section (2.2.1)). Generally, it is necessary to specify $a > 0$ to obtain a transition point that is far downstream of the inflow boundary and trailed by a recirculation region.

Third, when $V = 1.0$, $a = 0$, and Reynolds number is increased from 40, the flow first develops a single recirculation region when Re $\approx$ 50, and develops additional recirculation regions, downstream of the first, as Reynolds number is further increased. However, the formation of a transition point is not observed. The flow examined in Section (3.2), Re = 200 and $V = 1.0$, is an intermediate case in which a single, recirculation region is trailed by a global minimum in centerline axial velocity. At the minimum the velocity is positive, but becomes negative at higher Reynolds numbers. When Re = 829, the flow approximately represents

a wave train, as indicated by large-amplitude, spatial oscillations of centerline axial velocity. When $V = 0.777$, the same sequence of events is observed as Reynolds number is increased from 10, except that transition to an oscillatory state occurs within the computational domain and flow oscillations have a greater degree of symmetry about points at which there is an extrema in vortex radius. Also, reversed flow is not observed.

Fourth, when solutions are computed through continuation in V, starting at $V = 0$, with Re $= 200$ and $a = 0$, the solution path is found to fold back on itself twice, leading to nonunique solutions over a range of vortex strengths. Nonunique solutions are also computed for a range of Reynolds numbers with $V = 1.0$, but in this situation two solution paths exist that are disconnected.

3.3.1 Continuation in Re From 40 to 829 with V=1

A set of solutions was computed by continuation in Reynolds number for Re ranging between 40 and 829 with $V = 1.0$, $a = 0$, and the following choice of grid parameters: $I = 209$, $Z = 20$, $J = 27$, and $R = 2$. The same values of V and a were selected for the comparison case treated in Section (3.2). Also, the implicit condition on inflow vorticity, $u(0, r) = 0$, was enforced.

It was found that for $a = 0$, the specification of $V = 1.0$ caused the flow to become reversed almost immediately downstream of the inflow boundary. Consequently, large gradients in the flow were present at, and just downstream of, the inflow boundary. Use of the explicit condition on inflow vorticity

$$-r\eta(0, r) = \psi_{rr}(0, r) - \frac{\psi_r(0, r)}{r}, \tag{3.1}$$

led to similar results, but in violation of the assumption of quasi-cylindrical inflow. The implicit condition on inflow vorticity does not require axial gradients at the inflow boundary to be small.

Continuation was initiated by first finding a solution for Re $= 40$ with Newton's method. Reversed flow occurred for Reynolds numbers larger than about 50.

Contour plots of streamfunction are shown in Figure (3.7) for selected Reynolds numbers between 200 and 829. The sequence of contour plots indicates that as Reynolds number is increased, the flow tends toward a spatially oscillating system with multiple regions of reversed flow. A plot of centerline axial velocity for the case of highest Reynolds number, Re = 829, is shown in Figure (3.8). Solutions were not computed for Reynolds numbers higher than 829, since at this value the computations began to show evidence of short-period numerical noise as can be seen in Figure (3.8) for $z \approx 4.0$. The onset of noise occurred at lower Reynolds number when $I = 105$ was chosen in favor of $I = 209$, with all other parameter values kept the same.

Azimuthal velocity in the reversed flow region is shown in Figure (3.9) for the case with Re = 829. Azimuthal velocity was plotted against radial position for $z = 2.1$, the axial position of the "eye" of the first region of reversed flow. The azimuthal velocity profiles at the inflow and outflow boundaries are also shown in Figure (3.9). The latter two profiles are nearly identical as $r \rightarrow 2$, indicating that the vortex does not diffuse beyond the bounds of the computational domain.

The circulation perturbation norm, E_Γ (see Appendix B), is shown plotted against the inverse of Reynolds number in Figure (3.10) for Re ranging between 40 and 829. (The norm is plotted against the inverse of the Reynolds number instead of Re, since $\frac{1}{\mathrm{Re}}$ was chosen to be the free parameter in the continuation procedure.) Note that structural change in the flow, associated with the emergence of reversed-flow regions, does not correspond to any interesting behavior in the solution path.

Contour plots of azimuthal vorticity for selected Reynolds number between 200 and 829 are shown in Figure (3.11).

3.3.2 Continuation in V from 0 to 1.263 with Re=200

The computed solution path, $E_\Gamma(\mathrm{Re})$, presented in Section (3.3.1) for $V = 1.0$, was found to be free of limit points and bifurcation points over the range of

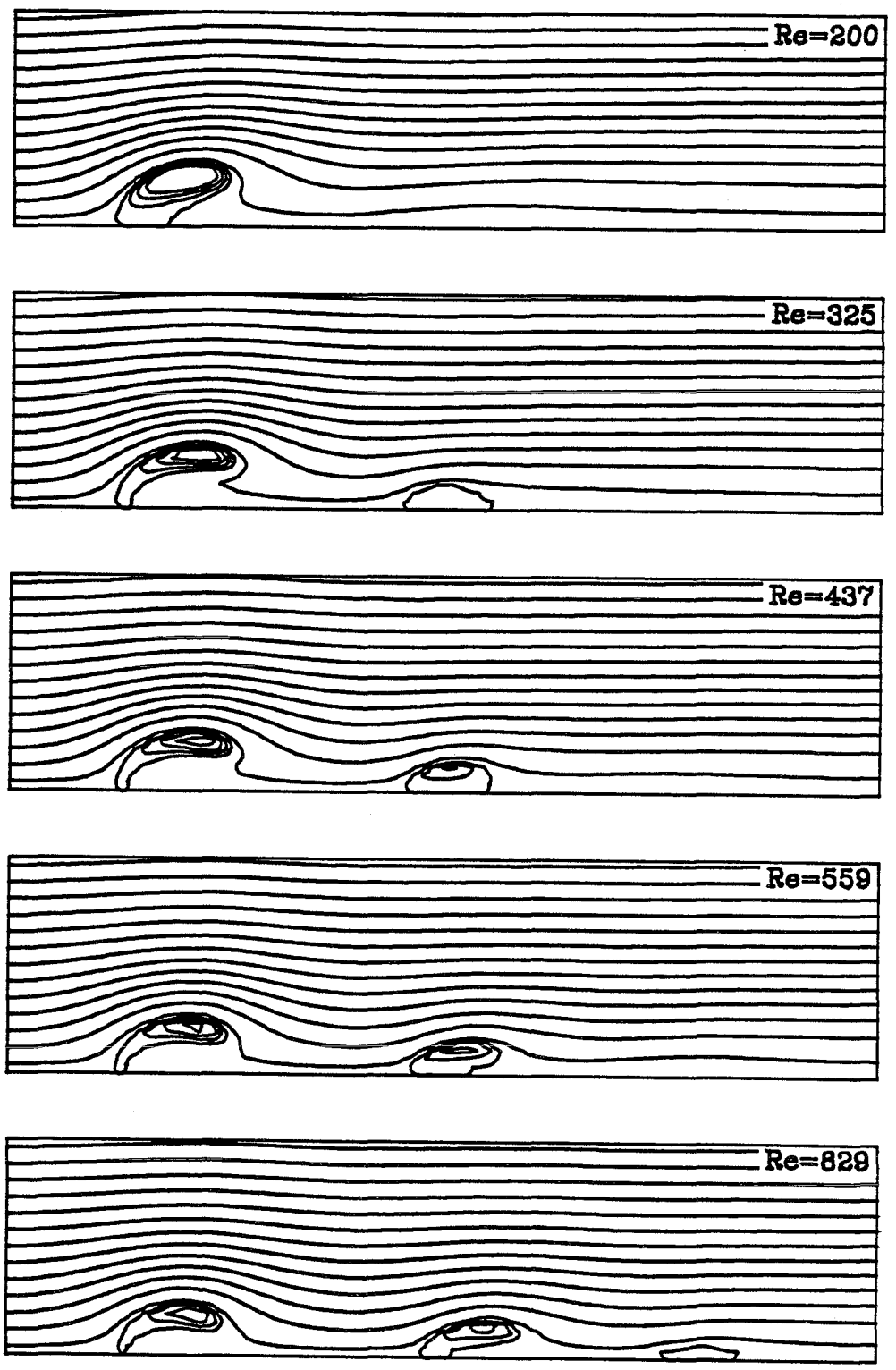

Figure 3.7 Contour plots of ψ for selected Reynolds numbers between 200 and 829 ($0 \leq r \leq 2$, $0 \leq z \leq 10$)

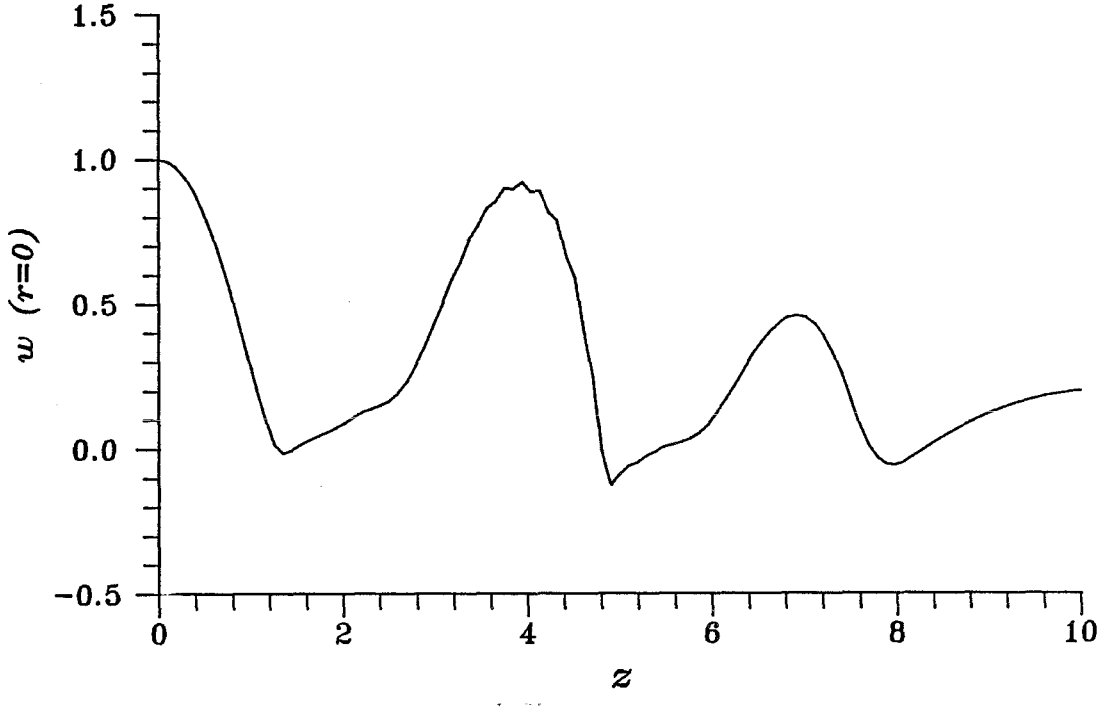

Figure 3.8 Centerline axial velocity versus axial position for Re = 829 and $V = 1.0$

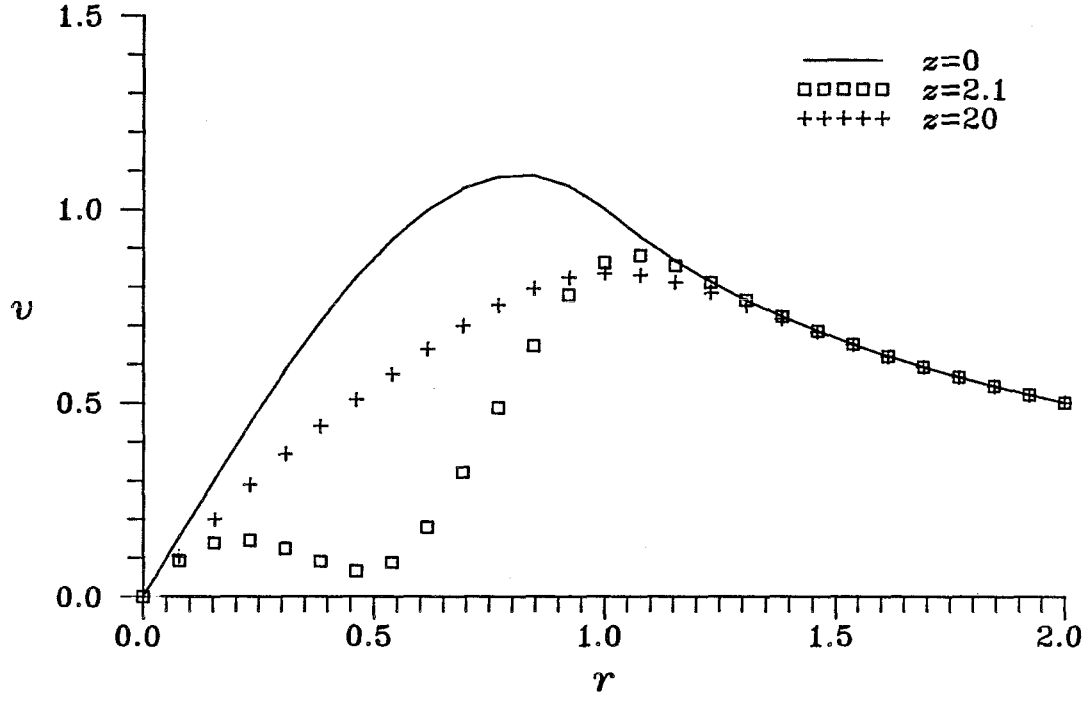

Figure 3.9 Azimuthal velocity versus radial position at three different stations for Re = 829 and $V = 1.0$

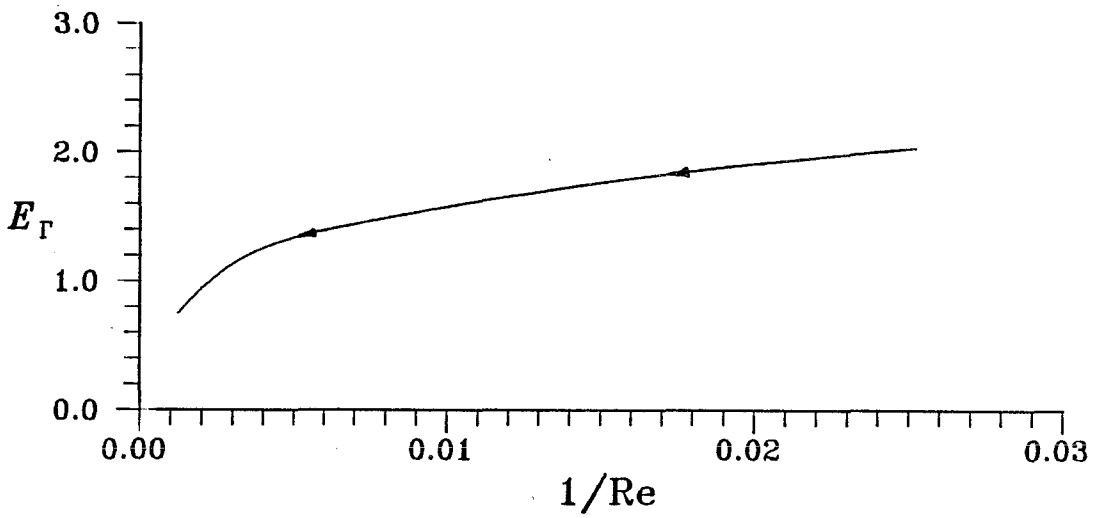

Figure 3.10 Solution path as represented by $E_\Gamma(\frac{1}{\mathrm{Re}})$ with $V = 1.0$

Reynolds numbers examined. As will be seen in Sections (3.3.8) and (3.3.9), this is also found true of solution paths resulting from continuation over a much wider range of Re with $V = 0.777$. However, nonunique solutions of the Navier-Stokes equations are revealed through continuation in V with $\mathrm{Re} = 200$. It is discovered that for V ranging between 0.899 and 1.158, three possible solutions exist for each value of V with $\mathrm{Re} = 200$. These results were previously reported by Beran (1986).

In this section, solutions are obtained by continuation in vortex strength for V ranging between 0 and 1.263, with $\mathrm{Re} = 200$ and $a = 0$. The grid parameters I, Z, J and R were specified to be 105, 20, 27 and 2, respectively. The choice of $I = 105$ led to a value of h_z sufficiently small to prevent the development of short-period numerical noise. As in Section (3.3.1), these solutions were computed using the implicit condition on inflow vorticity.

The solution path, $E_\Gamma(V)$, for the continuation run is shown in Figure (3.12). The direction of continuation is indicated by arrows marked on the solution path. Arclength, s, is chosen to parameterize the path; s increases in the direction of continuation. Starting at $V = 0$ and then following along the path, a limit point is encountered at $V = 1.158$, at which point the solution path folds back on itself and V begins to decrease with increasing s. The branch of solutions between $V = 0$ and $V = 1.158$ will be referred to as branch I. V continues to decrease with increasing

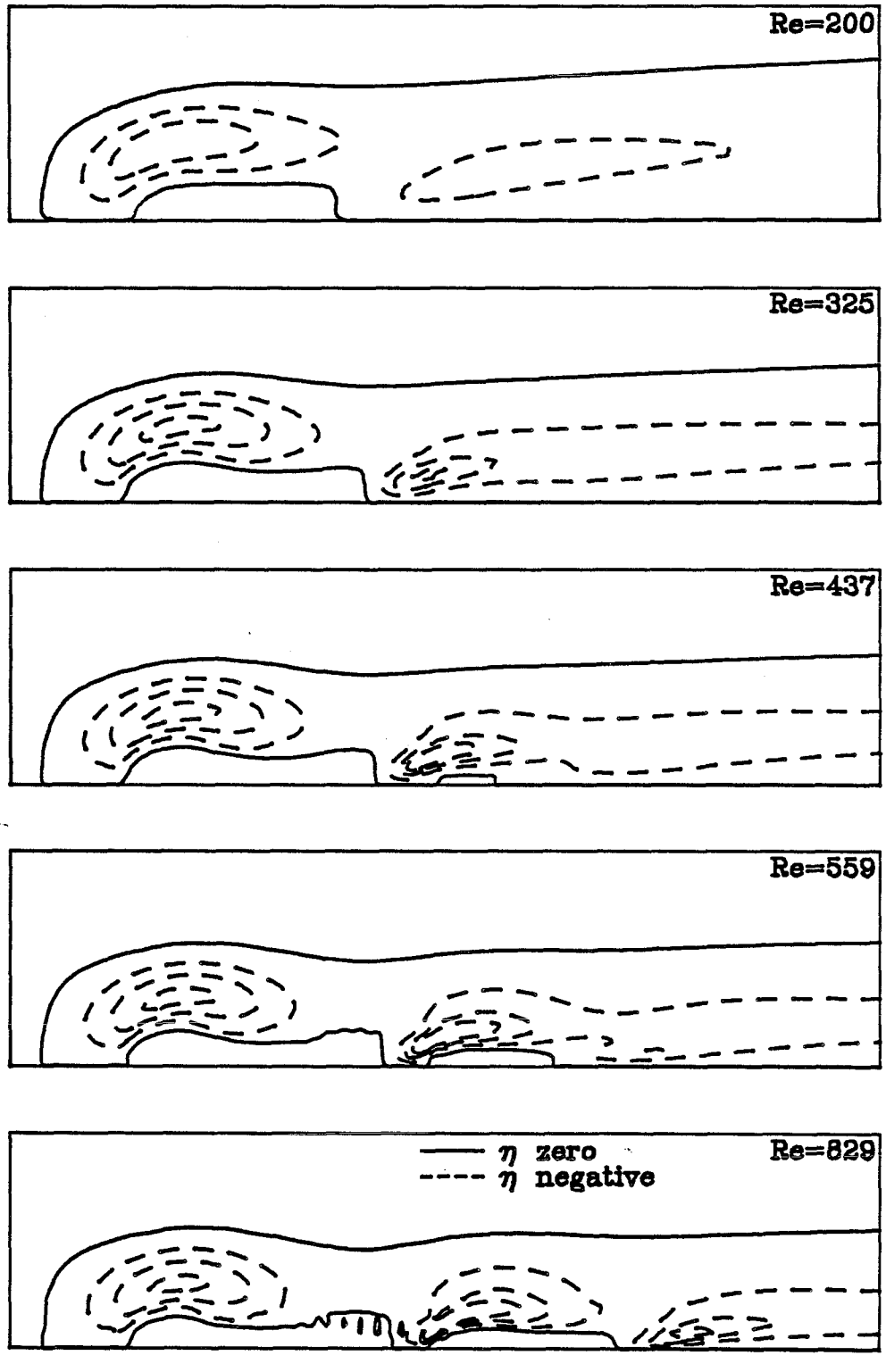

Figure 3.11 Contour plots of η for selected Reynolds numbers between 200 and 829 ($0 \leq r \leq 2$, $0 \leq z \leq 10$)

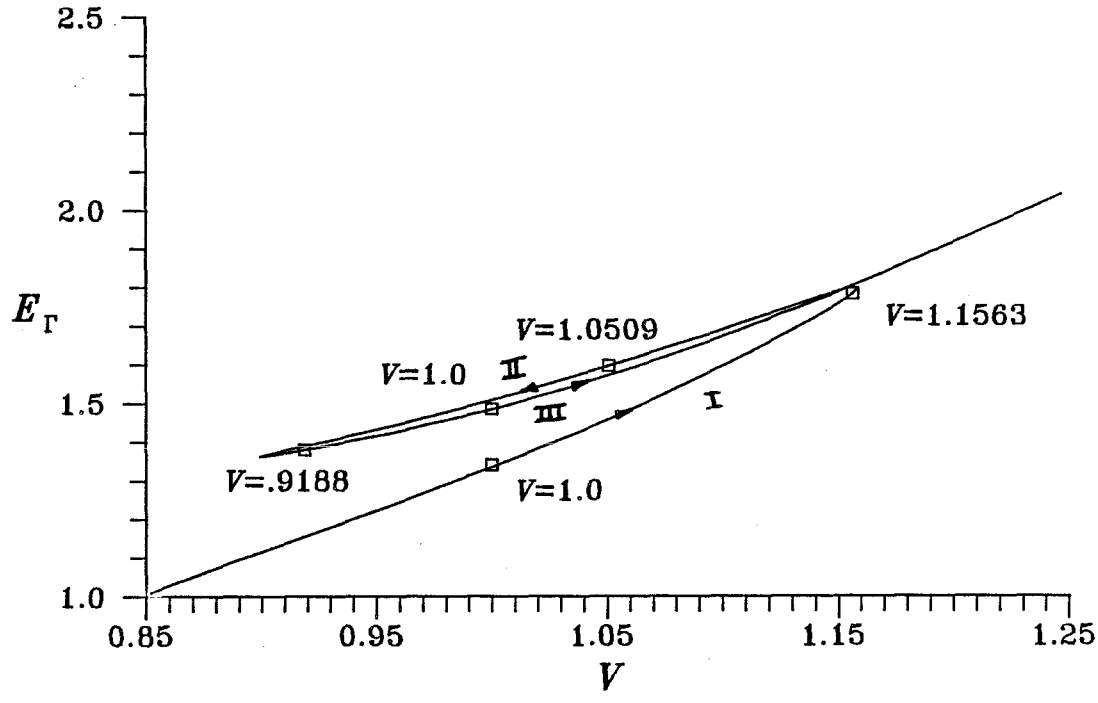

Figure 3.12 Solution path as represented by $E_\Gamma(V)$ with Re = 200

s until a second limit point is encountered at $V = 0.899$. The branch of solutions between the limit points will be referred to as branch II. Beyond this point, V increases with increasing s over the remaining portion of the computed solution path. This final branch will be referred to as branch III.

The sign of the determinant of the Jacobian matrix is found to change sign at both limit points, a necessary condition at simple limit points. The determinant is not found to change sign at any other points on the solution path. At $V = 0$, the flow is columnar, equivalent to the freestream flow, and stable to infinitesimal disturbances. Since the sign of the determinant of the Jacobian remains constant on branch I, bifurcation points corresponding to the change in sign of an odd number of eigenvalues of the Jacobian matrix cannot occur on this section of the path. On this branch, solutions will retain stability unless a Hopf bifurcation point or a bifurcation point, corresponding to the change in sign of even number of eigenvalues, is encountered. As the solution path passes through the first limit point at $V = 1.158$, there is an exchange of stability, and assuming branch I to

be stable, solutions on branch II must be unstable. There is no evidence that the stability of solutions on branch II changes. Stability is again exchanged as the path passes through the second limit point at $V = 0.899$. Similarly, there is no evidence of exchange of stability between the second limit point and the last point on the solution path.

Contour plots of ψ for selected values of vortex strength are shown in Figure (3.13). Selected solution points are marked in Figure (3.12). The point on branch I for $V = 1.0$ has already been described in Section (3.2). On branch I at $V = 1.1563$ (in the neighborhood of the first limit point), a toroidal streamsurface corresponding to $\psi = 0$ has lifted completely off the symmetry axis (in Figure (3.7) for $V = 1.0$ and $\mathrm{Re} = 200$, the streamsurface of $\psi = 0$ is attached to the symmetry axis). The reversed flow contained within the streamsurface moves in a clockwise sense, generating a prominent region of negative azimuthal vorticity. Contour plots of azimuthal vorticity for the cases shown in Figure (3.13) are presented in Figure (3.14). Solid lines in Figure (3.14) represent contours of zero azimuthal vorticity, while dashed lines represent contours of negative azimuthal vorticity.

The stability of columnar flows to rotationally symmetric disturbances is discussed in Appendix C. A sufficient condition for the stability of columnar flows to such disturbances, according to Howard and Gupta (1962), is

$$J(r) \geq 0.25 \quad 0 < r \leq R, \tag{3.2}$$

where

$$J(r) \equiv 2\Gamma \frac{\partial \Gamma}{\partial r} \left(\frac{\partial w}{\partial r} \right)^{-2} r^{-3}. \tag{3.3}$$

J is called the Richardson number and is a function of radial position in a columnar flow. Since (3.3) is a sufficient condition, a columnar flow may violate the condition, yet retain stability. Although the condition applies strictly only to columnar flows, it may still be useful when applied to flows with slowly varying core properties. For these cases, Richardson number is a function of radial position and

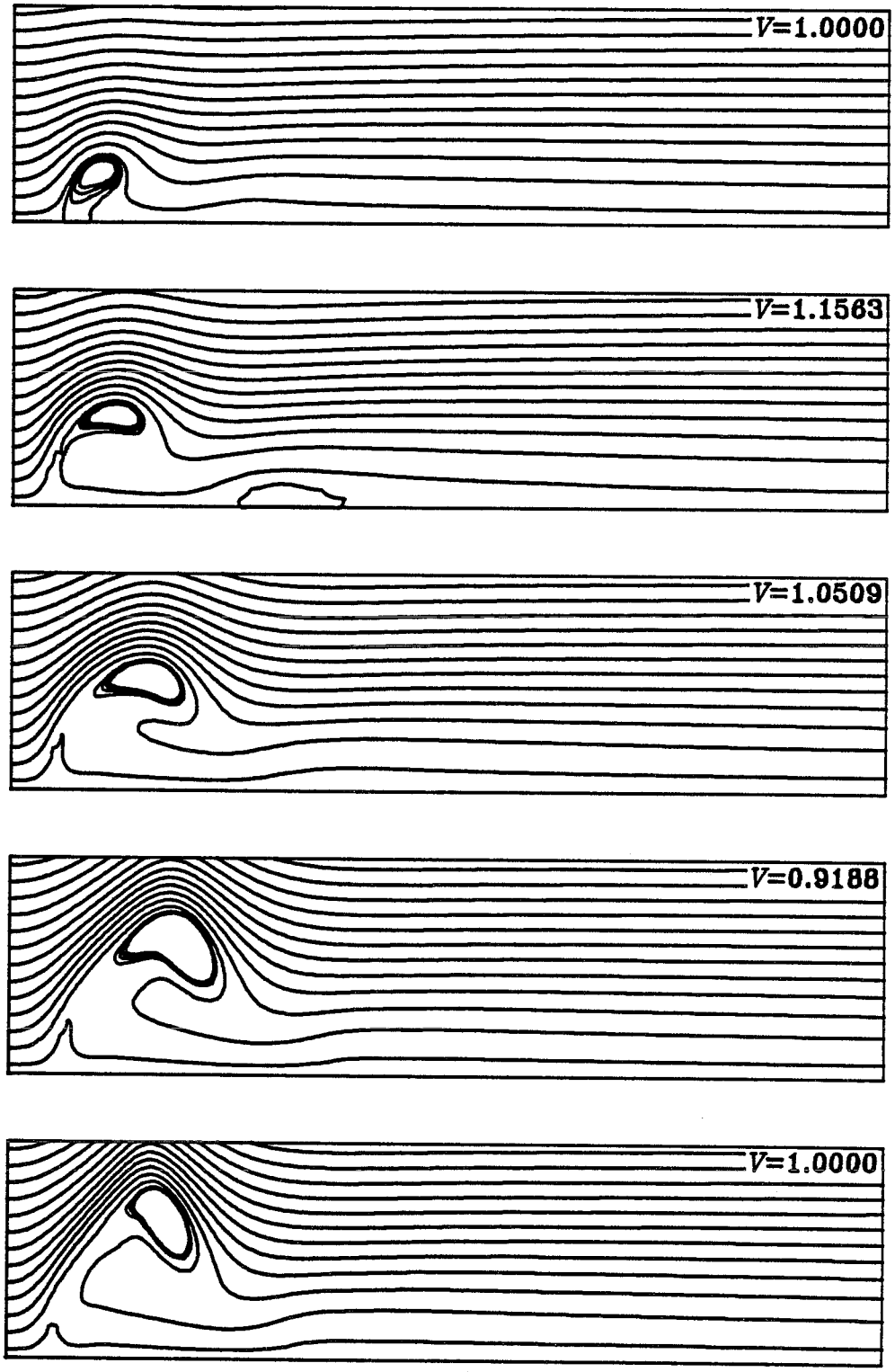

Figure 3.13 Contour plots of ψ for selected values of V between 0 and 1.263 with Re = 200 ($0 \leq r \leq 2$, $0 \leq z \leq 20$)

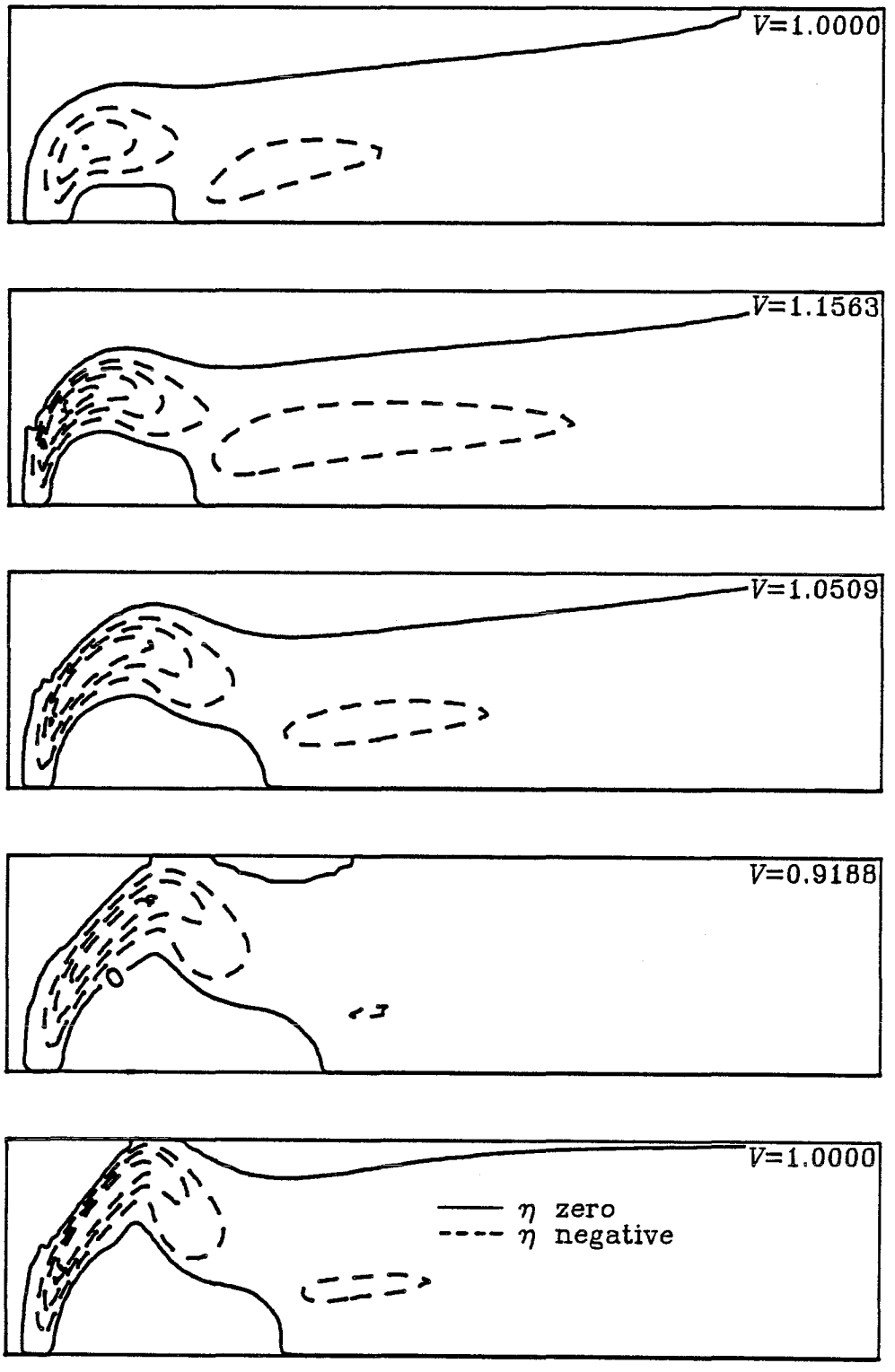

Figure 3.14 Contour plots of η for selected values of V between 0 and 1.263 with Re = 200 ($0 \leq r \leq 2$, $0 \leq z \leq 20$)

axial position. In an effort to determine if the exchange of stability occurring at the limit points observed on the solution path treated in this section is in any way related to meaningful changes in the Richardson number, $J(r,z)$ was computed for those solutions points marked in Figure (3.12). Contour plots of J are shown in Figure (3.15) for the five cases. Solid lines in Figure (3.15) represent contours of $J = 0.25$, while dashed lines represent contours for $J > 0.25$. It is observed that $J < 0.25$ in the regions of reversed flow, which occur in each of the five cases. Low values of Richardson number are computed in these regions because azimuthal velocity decreases with increasing radial position where the flow is reversed (see Figure (3.9)), leading to small radial gradients of circulation. $J < 0.25$ is also found in the upper-left corner of $\Re$ in each of the cases, although this appears to be due to truncation error, since in this part of the computational domain the radial gradients of both circulation and axial velocity nearly vanish (data were stored in single precision format, while computations were performed in double precision format).

The finding that $J < 0.25$ over some portion of $\Re$ in each of the cases is not inconsistent with the premise that some of the solutions are stable, since the condition (3.2) is only a sufficient condition. Also, as there is no significant qualitative difference between the contour plots of $J(r,z)$ for the five cases, it appears that Richardson number is not a useful parameter to descriminate between stable and unstable solutions.

There is a structural change of the flow as V is increased on branch I, which may lead to the limit point at $V = 1.158$ and the subsequent exchange of stability. When $V = 1.0$ on branch I, the reversed-flow region is "attached" to the symmetry axis, lying between a surface of $\psi = 0$ and the symmetry axis. As V increases, the center of the reversed flow region moves downstream and farther away from the symmetry axis. Also the stagnation points on the symmetry axis, located at the intersection points of the axis and the contour of $\psi = 0$, move towards each other. When $V = 1.1563$, just before the limit point, stagnation points are no

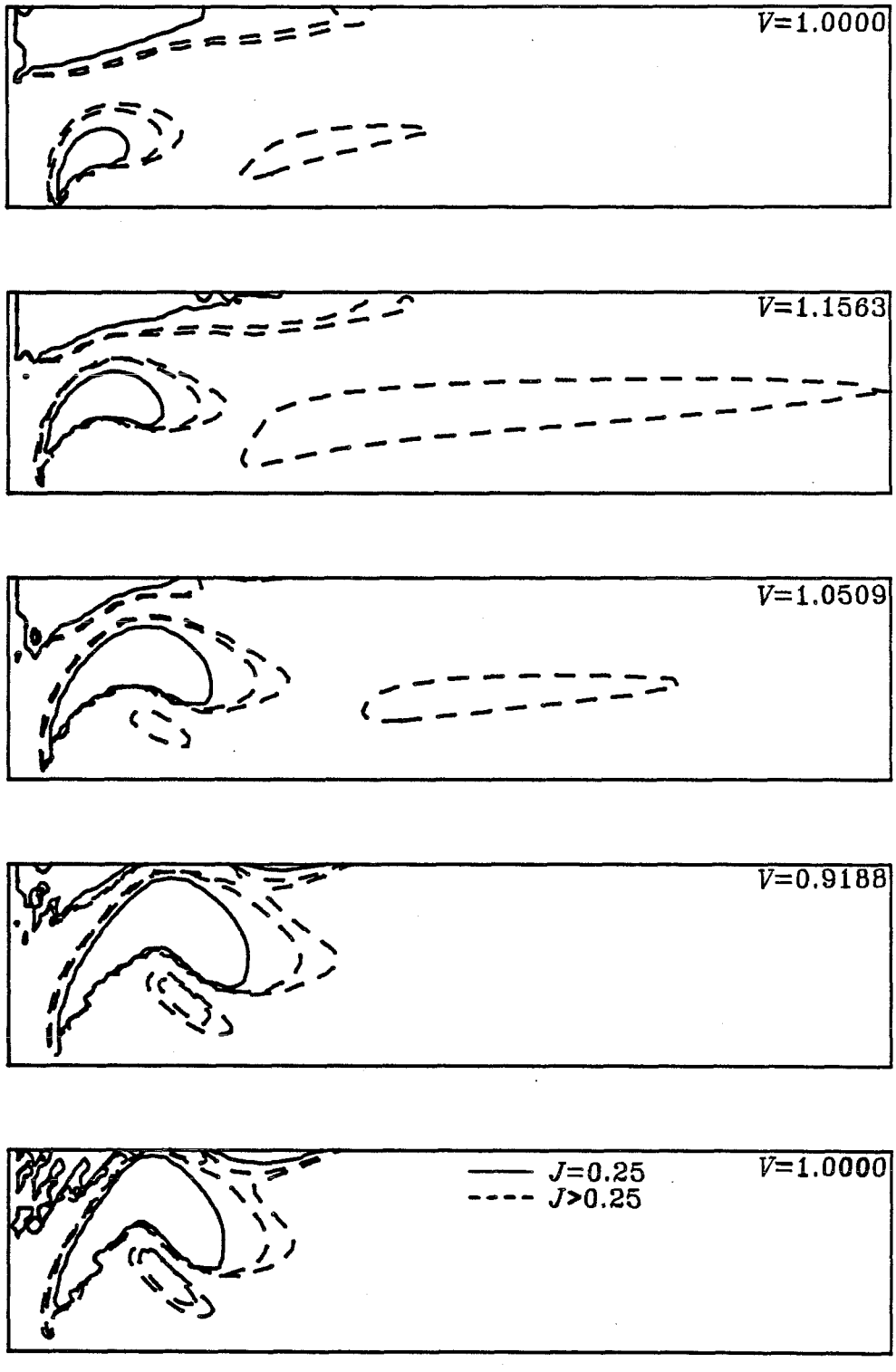

Figure 3.15 Contour plots of Richardson number, J, for selected values of V between 0 and 1.263 with Re = 200 ($0 \leq r \leq 2$, $0 \leq z \leq 20$)

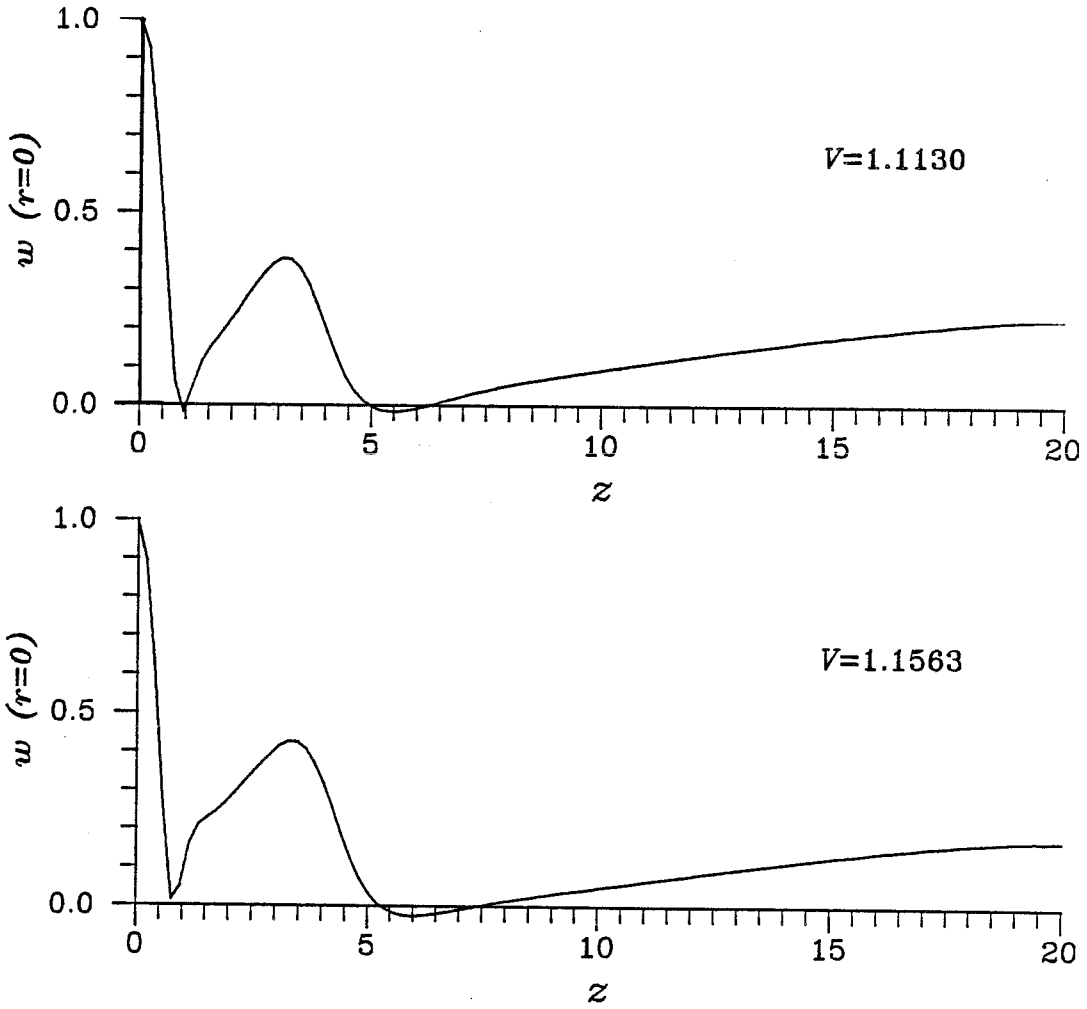

Figure 3.16 Centerline axial velocity versus axial position for $V = 1.1130$ and $V = 1.1563$ with $\mathrm{Re} = 200$

longer found on the symmetry axis, except far downstream of the inflow boundary where a second region of reversed flow has emerged. Centerline axial velocity is positive between the inflow boundary and the first of the two stagnation points belonging to this second region. Thus, the development of a limit point on the solution path at $V = 1.158$ may correspond to an adjustment of flow structure, required for the existence of solutions for $V > 1.158$ with regions of reversed flow completely detached from the symmetry axis.

Profiles of centerline axial velocity for two solution points, $V = 1.1130$ and $V = 1.1563$, on branch I are shown in Figure (3.16). A contour plot of ψ for the latter case is shown in Figure (3.13), while a similar plot for the former case

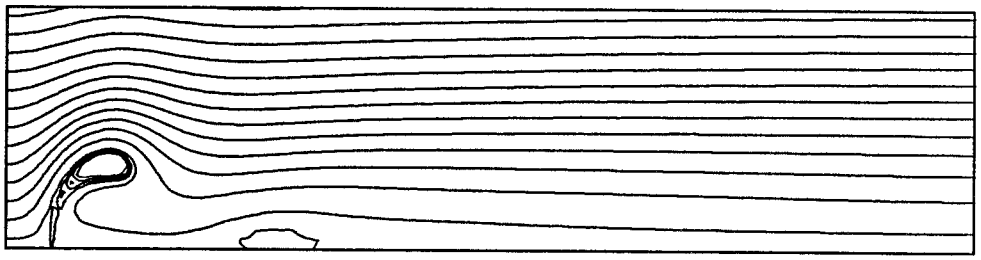

Figure 3.17 Contour plot of ψ for $V = 1.1130$ with Re $= 200$ ($0 \leq r \leq 2$, $0 \leq z \leq 20$)

is presented in Figure (3.17). Note that the profile of centerline axial velocity is shown in Figure (3.5) for $V = 1.0$. When $V = 1.0$ and $V = 1.1130$, the regions of reversed flow remain attached to the symmetry axis, and centerline axial velocity is negative between the stagnation points on the axis. When $V = 1.1563$, reversed flow on the symmetry axis is limited to the secondary region of reversed flow previously mentioned.

3.3.3 Continuation in Re from 200 to 560 with V=1.0 (Disconnected Branch)

In Section (3.3.2), nonunique solutions were found over a range of vortex strengths with Re $= 200$. For a value of V in this range, e.g., $V = 1.0$, the nonunique solutions must represent points on solution paths obtained when Re is varied and V is fixed. One branch of solutions was already found in Section (3.3.1), when Re was varied between 40 and 829 with $V = 1.0$. No limit points or bifurcation points were observed on this branch. It is found in this section that there exists a folded solution path that is disconnected from the path computed in Section (3.3.1).

The starting point for the continuation procedure was the solution point on branch III, presented in Section (3.3.2), for $V = 1.0$ and Re $= 200$. In this section the same values of I, Z, J and R were chosen as in the previous section; $a = 0$ was

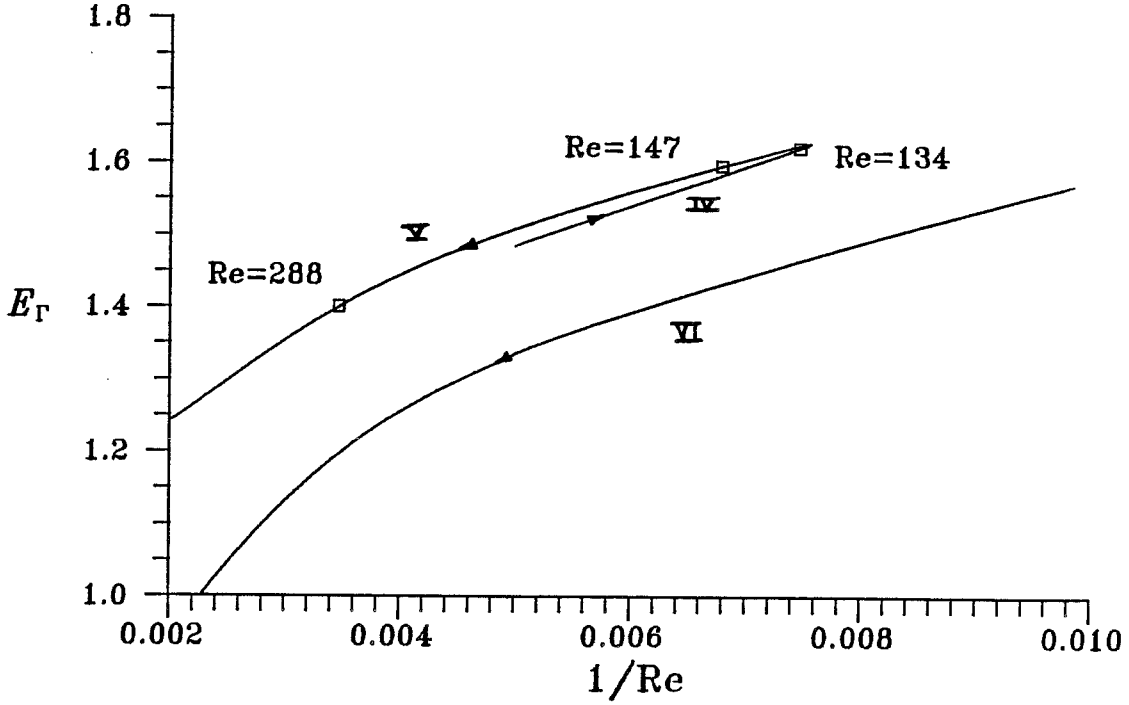

Figure 3.18 Solution path as represented by $E_\Gamma(\frac{1}{\mathrm{Re}})$ with $V = 1.0$

also specified. The disconnected solution path was computed by continuation in $\frac{1}{\mathrm{Re}}$ and is shown in Figure (3.18). Also shown in this figure is the branch of solutions reported in Section (3.3.1). Again, s is used to denote arclength and increases in the direction of continuation, shown in Figure (3.18).

From the starting point, Re decreases with increasing s. At Re = 132, a limit point is encountered, whereupon the solution path folds back on itself. The branch of solutions between the starting point and the limit point will be referred to as branch IV, and the branch on the top of the fold will be referred to as branch V. The path below both branches IV and V will be referred to as branch VI. Since the starting point for the continuation procedure discussed in this section is a point lying on branch III (see Section (3.3.2)), then branches IV and III lie on a common surface in the space formed by E_Γ, V and Re. Similarly branches V and II and branches VI and I lie on common surfaces. Thus, assuming that branches I, II and III are stable, unstable and stable, respectively, as discussed in the last section, then branches VI, V and IV have the same stability properties, respectively. All six

branches actually lie on the same solution surface, although this surface has two folds that separate three portions of the surface, corresponding to three branches when $V = 1.0$. It would be very interesting to compute the set of limit points on this folded surface, using a procedure similar to that developed by Fier (1985) to trace folds on solution sheets for the problem of flow between two infinite, rotating disks. With this technique, both V and Re would be free parameters, allowing both folds to be mapped onto the parameter space, (V, Re). Such an effort, not attempted in this work, would provide a global description of the solution surface. It is anticipated that if solution paths were computed via continuation in V in the manner of Section (3.3.2), for several values of Re below 200, then it would be found that as Re decreases, the difference in V between the two limit points would also decrease. Assuming this to be true, at some sufficiently small value of Re, both limit points would vanish, leaving a solution path free of limit points. It is further conjectured that the projection of the set of computed limit points on the (V, Re) plane would form two branches of points, possibly joined at a cusp point.

Contour plots of ψ for selected solution points on the path are shown in Figure (3.19). The selected points are marked in Figure (3.18).

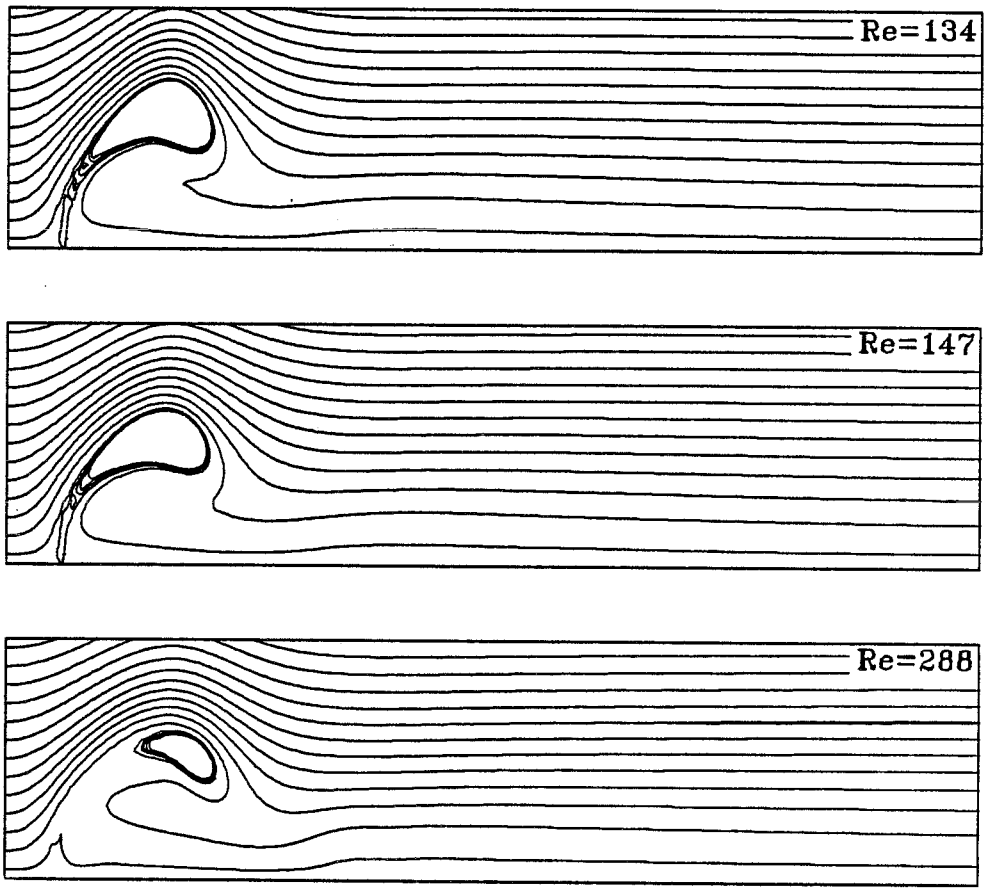

Figure 3.19 Contour plots of ψ for selected solution points on branches IV, V and VI with $V = 1.0$ ($0 \leq r \leq 2$, $0 \leq z \leq 20$)

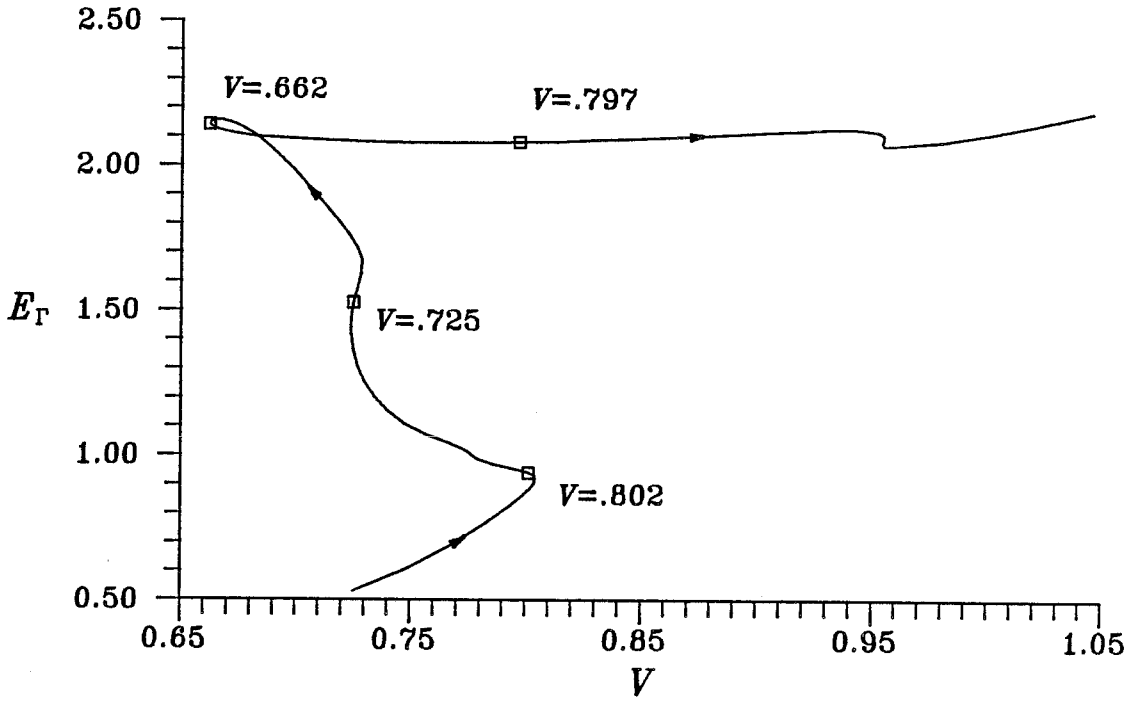

Figure 3.20 Solution path as represented by $E_\Gamma(V)$ with Re = 200

3.3.4 Continuation in V from 0 to 1.601 with Re=200 (Explicit Condition)

Solutions presented in Sections (3.3.1)—(3.3.3) were computed using the implicit condition on inflow vorticity. In this section, solutions are obtained using the explicit condition on inflow vorticity to determine if enforcement of this boundary condition also leads to nonunique solutions. It is found, through continuation in V, that nonunique solutions do indeed exist.

The parameters I, Z, J and R were specified to be 105, 20, 27 and 2, respectively, and Reynolds number was chosen to be 200; $a = 0$ was also specified. The starting point for the continuation procedure was the case of uniform flow, $V = 0$. The solution path computed is shown in Figure (3.20). Solution points of interest and the direction of continuation are marked in the figure.

Figure (3.20) indicates a more complicated behavior than that observed in Section (3.3.2). There are six limit points on the solution path. The solution space becomes more complex when the explicit condition on inflow vorticity is

enforced, possibly because when $V \approx 0.8$, large axial gradients in the flow occur at the inflow boundary, inconsistent with the assumption of quasi-cylindrical flow at that boundary. However, when $V << 1$, the flow at the inflow boundary is quasi-cylindrical. In some sense, there must be a change in the meaning of the explicit condition on inflow vorticity as V is increased. This point will be discussed further below.

Contour plots of ψ are provided in Figure (3.21) for the points marked in Figure (3.20). These plots show an evolution, as V is varied, of the structure of the reversed flow that is similar to the evolution described in Section (3.3.2). In general, the primary region of reversed flow occurs upstream of the point where it forms when the implicit condition is enforced. Profiles of centerline axial velocity are shown in Figure (3.22) for selected solution points. When V is less than about 0.78, the axial velocity decays slowly in the vicinity of the inflow boundary. In this region, the flow is approximately quasi-cylindrical. As V is increased, the extent of quasi-cylindrical flow in the vicinity of the inflow boundary diminishes rapidly until large axial gradients in the flow occur at the boundary. However, in this situation, the explicit condition constrains the axial velocity to decrease linearly with axial position near the inflow boundary (cf. Figure (3.22) for $V = 0.725$). Enforcement of the explicit condition implies that $u_z = 0$ at the inflow boundary and that by differentiation of the continuity equation

$$\frac{\partial w}{\partial z} + \frac{u}{r} + \frac{\partial u}{\partial r} = 0 \tag{3.1}$$

with respect to z, it is concluded that at the inflow boundary, $w_{zz} = 0$. Thus, the explicit condition can accommodate large axial gradients in the flow at the inflow boundary that involve a linear decrease of axial velocity with z. These flows are much different in character, however, than those obtained when the flow is quasi-cylindrical at the inflow boundary.

3.3.5 Continuation in V from .5000 to .8048 with Re=1000

Solutions of (2.21) were computed using continuation in vortex strength for V

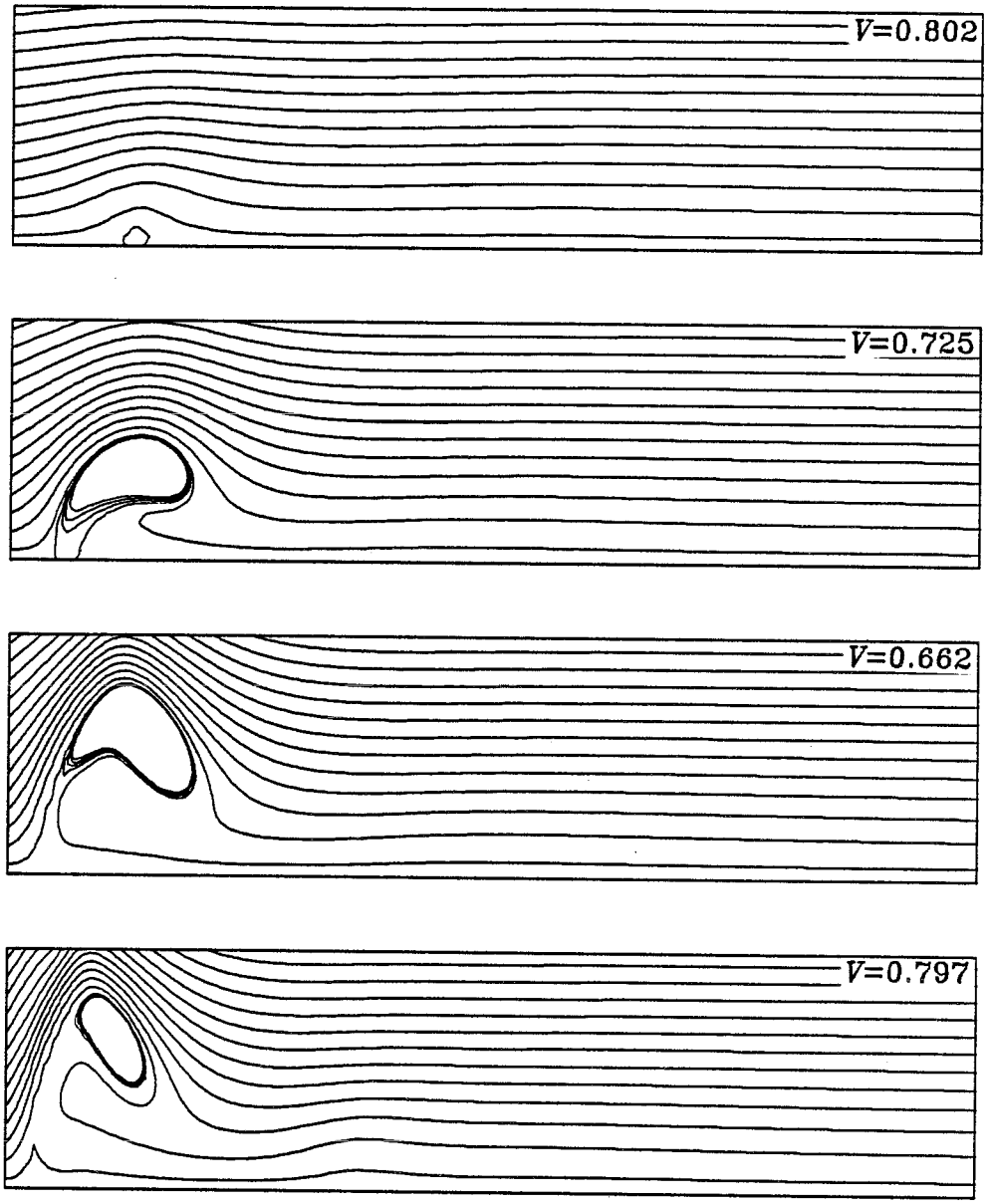

Figure 3.21 Contour plots of ψ for selected solution points on the solution path shown in Figure (3.20) ($0 \leq r \leq 2$, $0 \leq z \leq 20$)

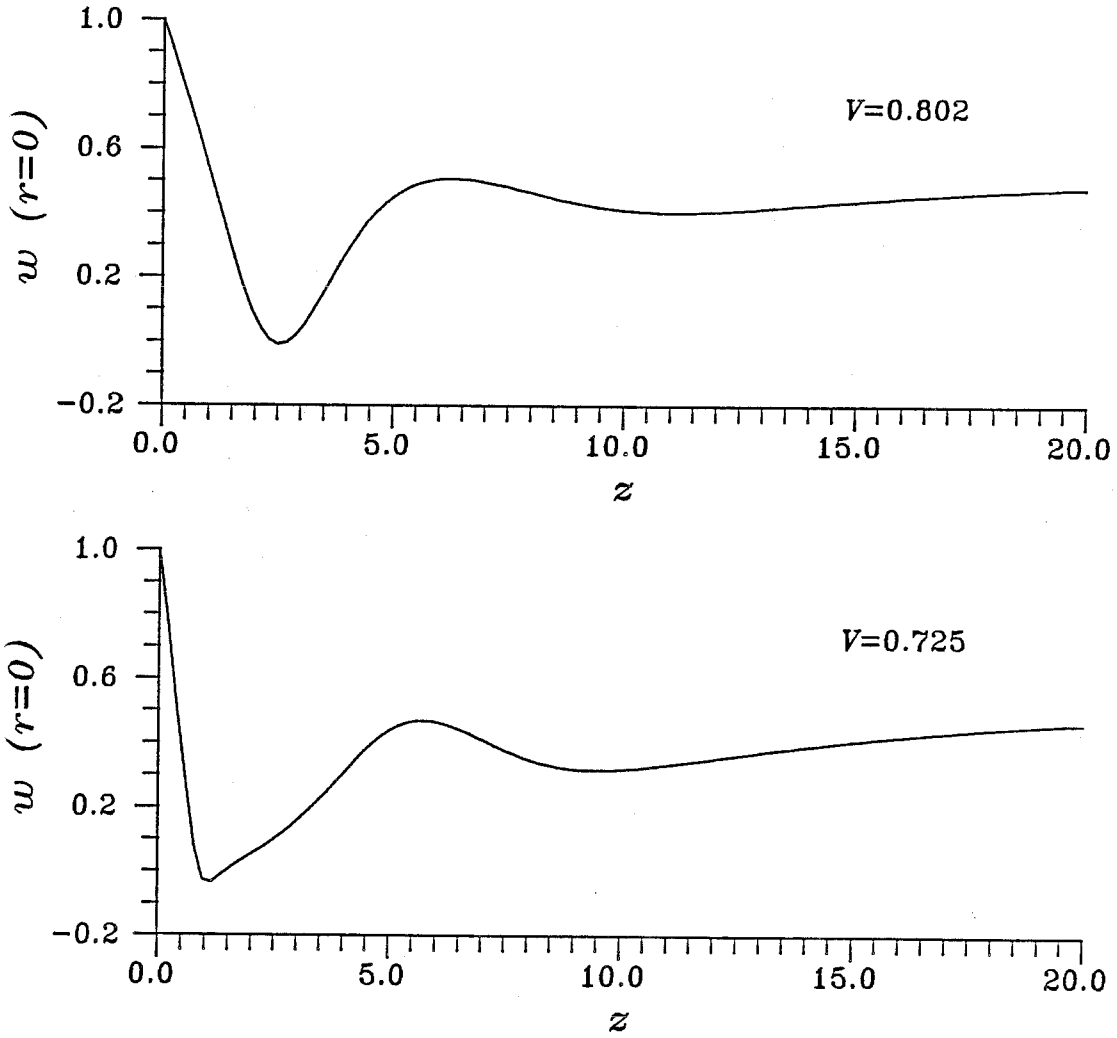

Figure 3.22 Centerline axial velocity versus axial position for $V = 0.802$ and $V = 0.725$ with $\mathrm{Re} = 200$

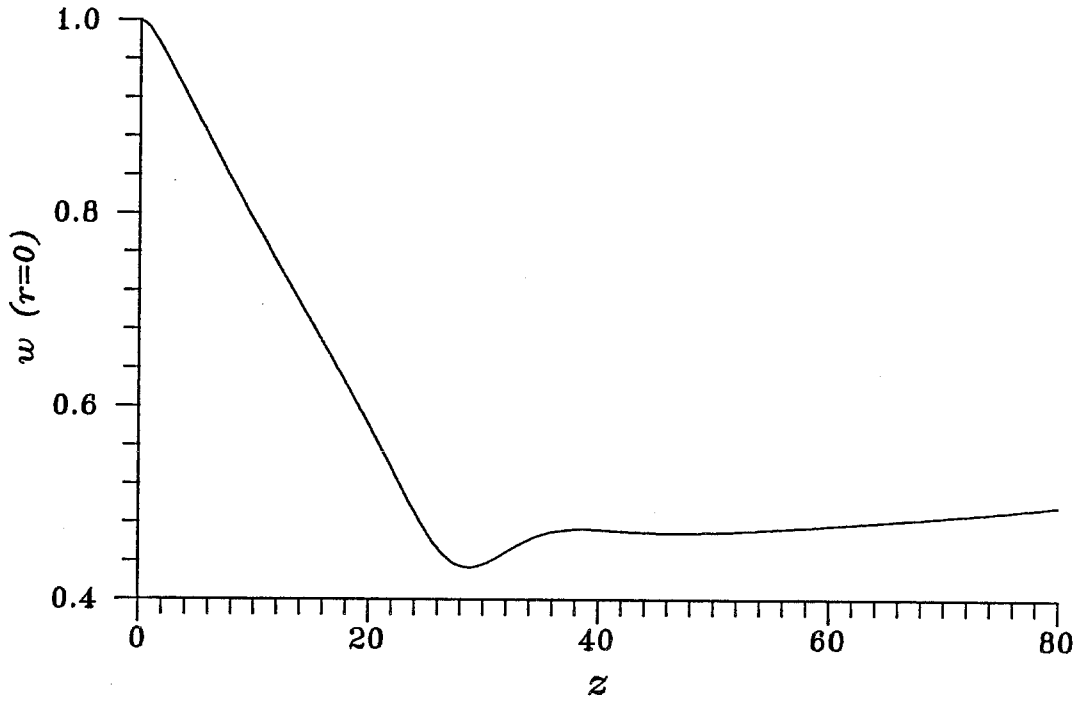

Figure 3.23 Centerline axial velocity versus axial position for $V = 0.7808$ with $\mathrm{Re} = 1000$

ranging between 0.5 and 0.8048, with $\mathrm{Re} = 1000$ and $a = 0$. The grid parameters I, Z, J and R were specified to be 209, 80, 27 and 2, respectively. The implicit condition on inflow vorticity, $u(0, r) = 0$, was enforced. Similar results for $\mathrm{Re} = 2000$ are obtained using the explicit condition on inflow vorticity and are discussed in Section (3.3.6).

Centerline axial velocity profiles for vortex strengths of 0.7808, 0.7955, and 0.8048 are presented in Figures (3.23), (3.24) and (3.25), respectively. Figure (3.23) shows that centerline axial velocity decays almost linearly until about $z = 28$, at which point the flow accelerates, resulting in a well-defined minimum in centerline axial velocity. The slow decay of centerline axial velocity upstream of $z = 28$ is due to the diffusion of axial vorticity into the surrounding irrotational flow as described in Section (4.1). Downstream of the minimum, an indistinct local maximum occurs at $z \approx 40$, and a similarly faint local minimum occurs at $z \approx 45$.

When V is increased from 0.7808 to 0.7955, less than a two-percent change, the minimum value of centerline axial velocity decreases significantly and the min-

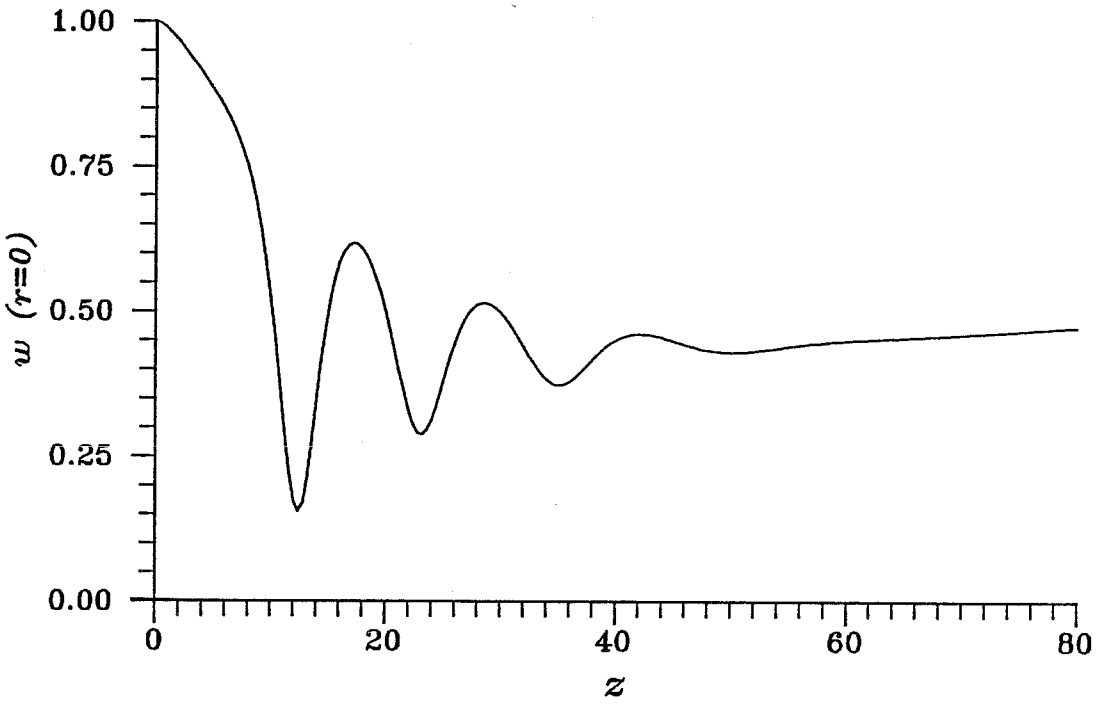

Figure 3.24 Centerline axial velocity versus axial position for $V = 0.7955$ with $\mathrm{Re} = 1000$

imum moves upstream to about $z = 12$, as shown in Figure (3.24). Three local maxima and three local minima are visible downstream of the global minimum. The centerline axial velocity at the outflow boundary is nearly the same, however, for both $V = 0.7808$ and $V = 0.7955$.

As V is increased further to 0.8048, the centerline axial velocity at the global minimum becomes negative and the minimum moves up to about $z = 6$, as shown in Figure (3.25). Three local maxima and three local minima occur downstream of the global minimum. The centerline axial velocity is nearly spatially periodic; oscillations are lightly damped and the oscillation period slowly increases with increased axial position. The centerline axial velocity at the outflow boundary is nearly the same in this case as for the other two cases, $V = 0.7808$ and $V = 0.7955$.

Reversed flow occurs when the transition point moves up to the inflow boundary. A transition point is not clearly apparent in Figures (3.23—3.25), since the transition point is nearly at the inflow boundary when $V = 0.7955$, but not yet in existence when $V = 0.7808$. The emergence of a transition point is clearly shown

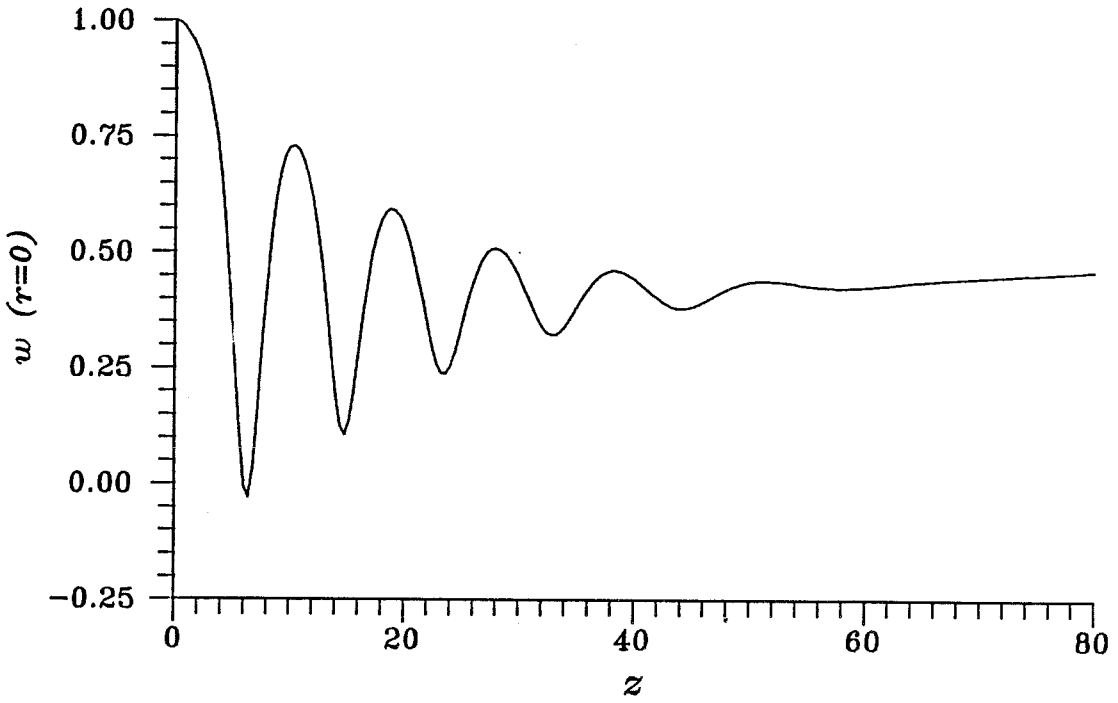

Figure 3.25 Centerline axial velocity versus axial position for $V = 0.8048$ with $\mathrm{Re} = 1000$

in Section (3.3.6).

Solutions are not presented for vortex strengths greater than 0.8048 because they showed evidence of short-period numerical noise. The development of numerical noise is attributed to the inability of the grid to resolve adequately the small length scale associated with the flow in the vicinity of the global minimum shown in Figure (3.25).

The flows represented in Figures (3.23—3.25) all have important regions of flow change downstream of $z = 20$, demonstrating the point made in Section (3.1), that computational domains longer than 20 core radii are required to model flows at Reynolds numbers exceeding 200.

3.3.6 Continuation in V from 0.10 to 0.7846 with Re=2000

Solutions of (2.21) were also computed using continuation in vortex strength for V ranging between 0.10 and 0.7846, with $\mathrm{Re} = 2000$ and $a = 0$. The grid parameters I, Z, J and R were specified to be 105, 80, 27 and 2, respectively. In

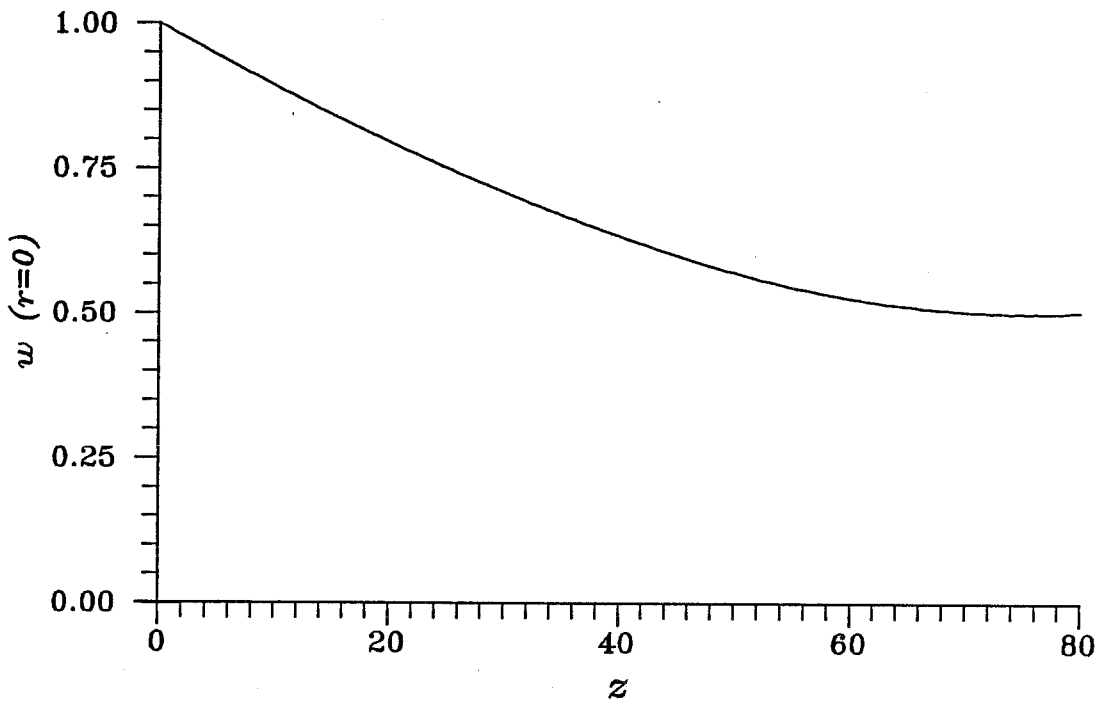

Figure 3.26 Centerline axial velocity versus axial position for $V = 0.7677$ with $\mathrm{Re} = 2000$

contrast with the inflow condition used in the last section, $u(0,r) = 0$, the explicit condition on inflow vorticity, (3.1), was enforced. With $a = 0$, (3.1) is equivalent to the specification of $\eta(0,r) = 0$.

For the case $V = 0.7846$, profiles of centerline axial velocity computed using both inflow conditions are compared.

Over most of the range of vortex strengths treated in this set of calculations, predicted flows are quasi-cylindrical for many core diameters downstream of the inflow boundary. In these cases, it is appropriate to enforce quasi-cylindrical flow at the inflow boundary, however it is artificial to enforce $u(0,r) = 0$.

Typical centerline axial velocity profiles for selected values of vortex strength between 0.7677 to 0.7846 are shown in Figures (3.26—3.29). In Figure (3.26) centerline axial velocity is seen to decay slowly over much of the length of the computational domain and it slowly starts to increase just upstream of the downstream boundary. At a slightly larger value of the vortex strength, $V = 0.7791$, a distinct minimum in the centerline axial velocity forms at $z \approx 44$, trailed by

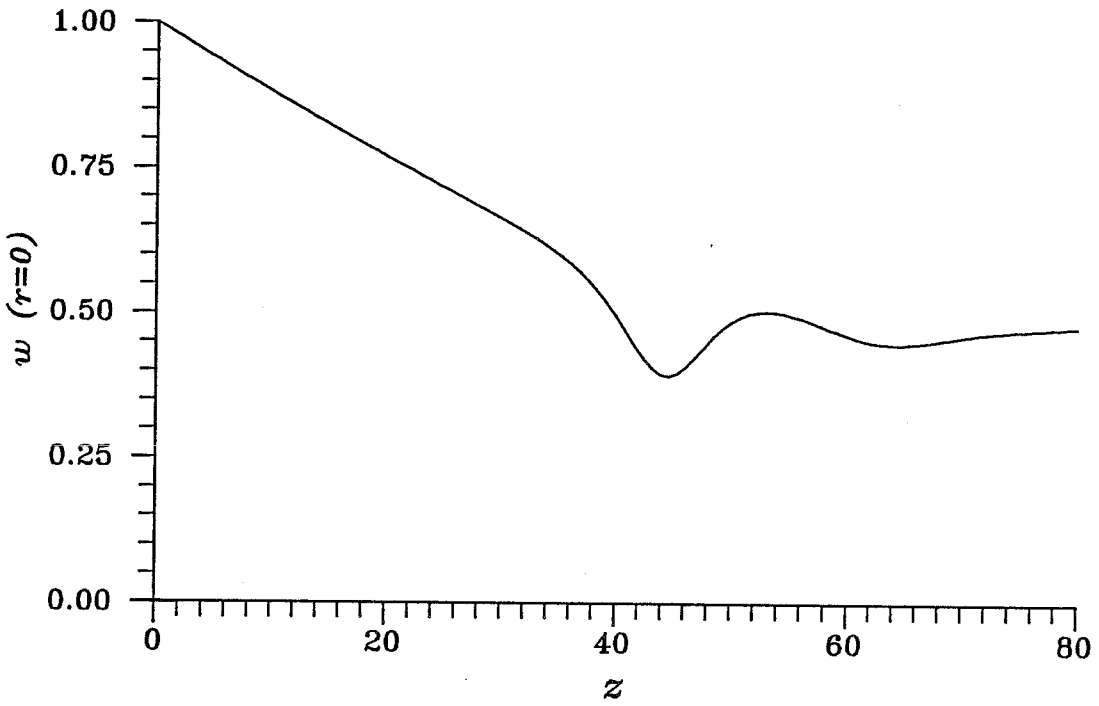

Figure 3.27 Centerline axial velocity versus axial position for $V = 0.7791$ with $\mathrm{Re} = 2000$

a local velocity maximum at $z \approx 53$ and a local velocity minimum at $z \approx 64$. The flow depicted in Figure (3.27) is much like the one depicted in Figure (3.23), except that in Figure (3.27) there is a noticeable change in the slope of the profile of centerline axial velocity at $z \approx 35$. This change in slope becomes more distinct when V is increased to 0.7823, as shown in Figure (3.28). The point at which the slope changes is defined to be the transition point. One way to view the transition point, discussed further in Section (3.4), is to consider the point to be the upstream bound on a wave train formed on the vortex.

The transition point is observed to move upstream as vortex strength increases as can be seen by comparing Figures (3.27) and (3.28). Wave amplitude also increases as V increases. Wave amplitude decreases with increasing downstream position, through the effect of viscosity, and flow wavelength increases with increased downstream position.

Transition point positions will be tabulated in Section (3.4) for the solutions presented in this section.

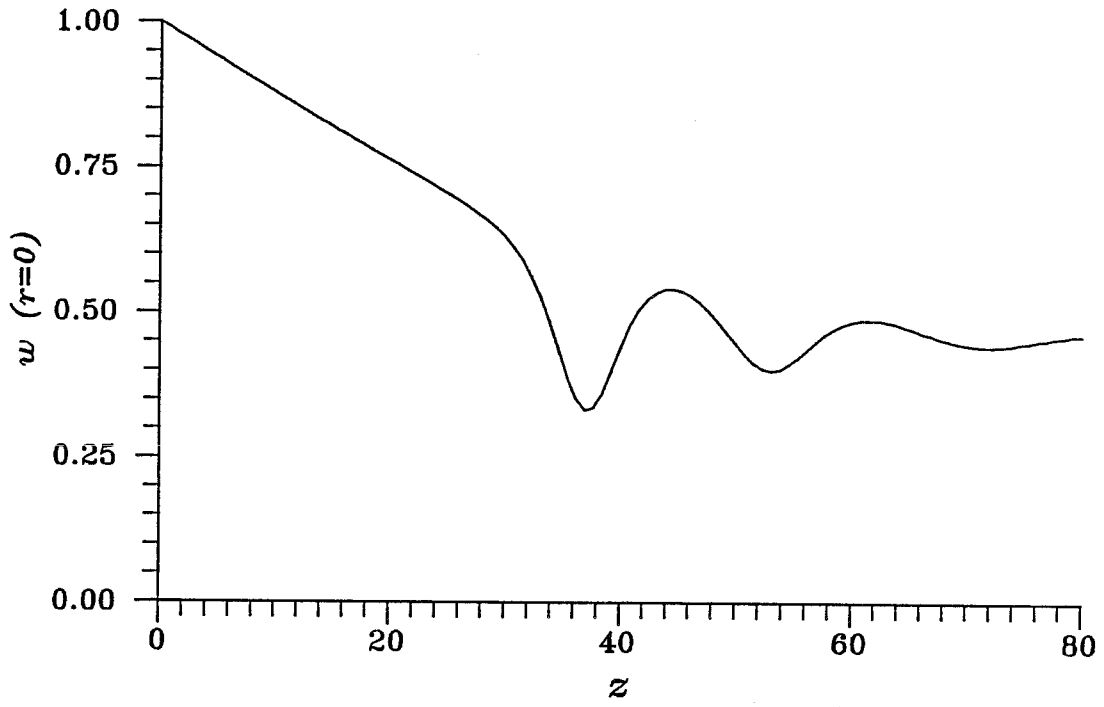

Figure 3.28 Centerline axial velocity versus axial position for $V = 0.7823$ with $\mathrm{Re} = 2000$

In Figure (3.29), centerline axial velocity profiles obtained using each of the two conditions on inflow vorticity with $V = 0.7846$ are shown. The implicit condition on inflow vorticity delays transition, shifting the computed maxima and minima downstream from those computed using the explicit condition on inflow vorticity. With the implicit condition on inflow vorticity, centerline axial velocity gradient decays linearly with axial position, despite having specified that the axial velocity gradient vanishes at the inflow boundary.

3.3.7 Continuation in Re from 2000 to 3239 for V=0.7846

The solution computed for the case, $\mathrm{Re} = 2000$, $V = 0.7846$ and $a = 0$ (see Figure (3.29)), was used as a starting point for continuation in Reynolds number. Solutions for Reynolds numbers up to 3239 were computed. Centerline axial velocity profiles for $\mathrm{Re} = 2767$ and $\mathrm{Re} = 3239$ are shown in Figure (3.30). The effects of increased Reynolds number include the delay of transition and the lengthening of the resulting wave train. These effects made it unreasonable to extend the

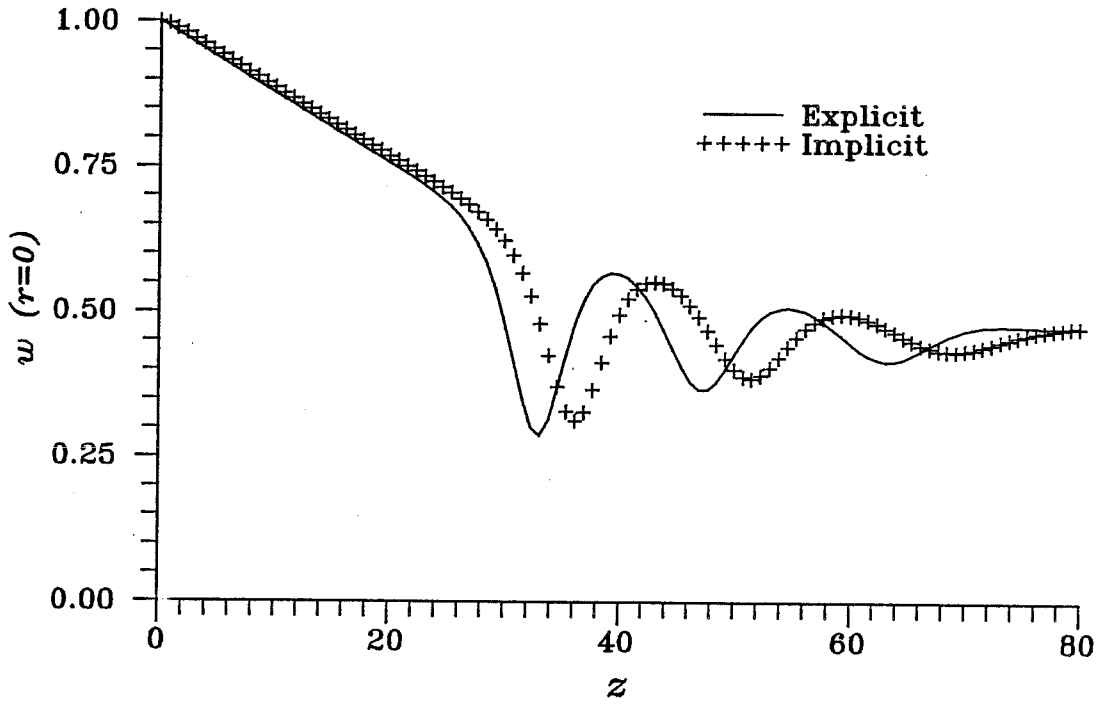

Figure 3.29 Centerline axial velocity versus axial position for $V = 0.7846$ with $\mathrm{Re} = 2000$ using two different conditions on inflow vorticity

continuation process beyond Re = 3239 because gradients associated with wave development at the downstream boundary began to conflict with the conditions specified at that boundary. Anomalous solutions were computed for Reynolds numbers larger than 3239 with $Z = 80$.

The relationship between Reynolds number and transition-point position is further examined in Section (4.4).

Oscillation wavelength, in the vicinity of the transition point, was found to be nearly independent of Reynolds number. The centerline axial velocity profiles of Figures (3.29) and (3.30) are plotted in Figure (3.31) with the centerline axial velocity profile for the case Re = 3239. The profiles are appropriately offset in the axial direction to align the global minima of the three profiles. Offset positions of the transition points, leading local maxima and global minima, were nearly the same. Alignment indicates that in the vicinity of the transition point, wave wavelength is nearly independent of Reynolds number and suggests that wave behavior is an inviscid phenomenon. For offset positions greater than about 45,

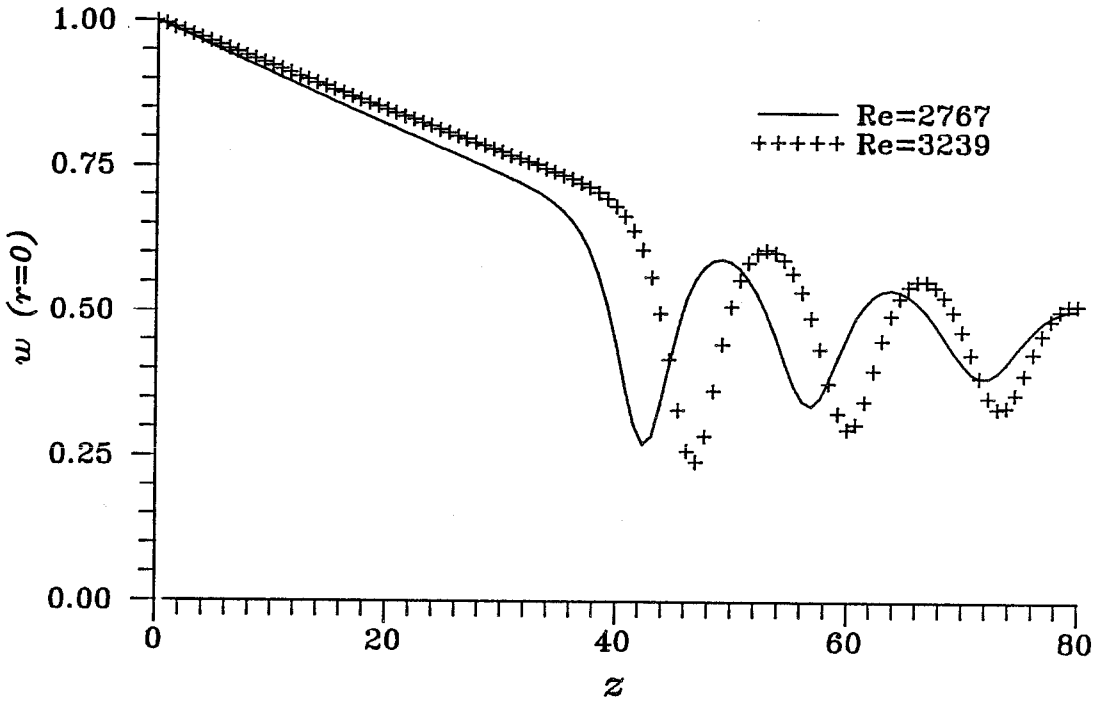

Figure 3.30 Centerline axial velocity versus axial position for Re = 2000, Re = 2767 and Re = 3239 with $V = 0.7846$

wavelength was not independent of Reynolds number, but this might be expected since it was seen in Figures (3.28) and (3.29) that over several periods, wavelength increases. Inspection of Figure (3.31) reveals that as Reynolds number increases, the rate of wavelength increase with downstream position decreases.

Figure (3.32) shows plots of azimuthal velocity versus axial position (for $r = 1$) for the three cases: Re = 2000, Re = 2767 and Re = 3239. The alignment of minima and maxima in this figure is identical to that observed in Figure (3.31).

3.3.8 Continuation in Re from 10 to 9977 with V=0.7770: Fine Grid

Several solutions were computed by continuation in Re for Reynolds number ranging between 10 and 9977 with V fixed at 0.7770. The grid parameters I, Z, J and R were specified to be 209, 300, 27 and 2, respectively. A plot of centerline axial velocity versus axial position is shown in Figure (3.33) for the highest Reynolds number solution, Re = 9977. Locations of computed data points were marked in the figure to demonstrate that the length scale of velocity oscillations

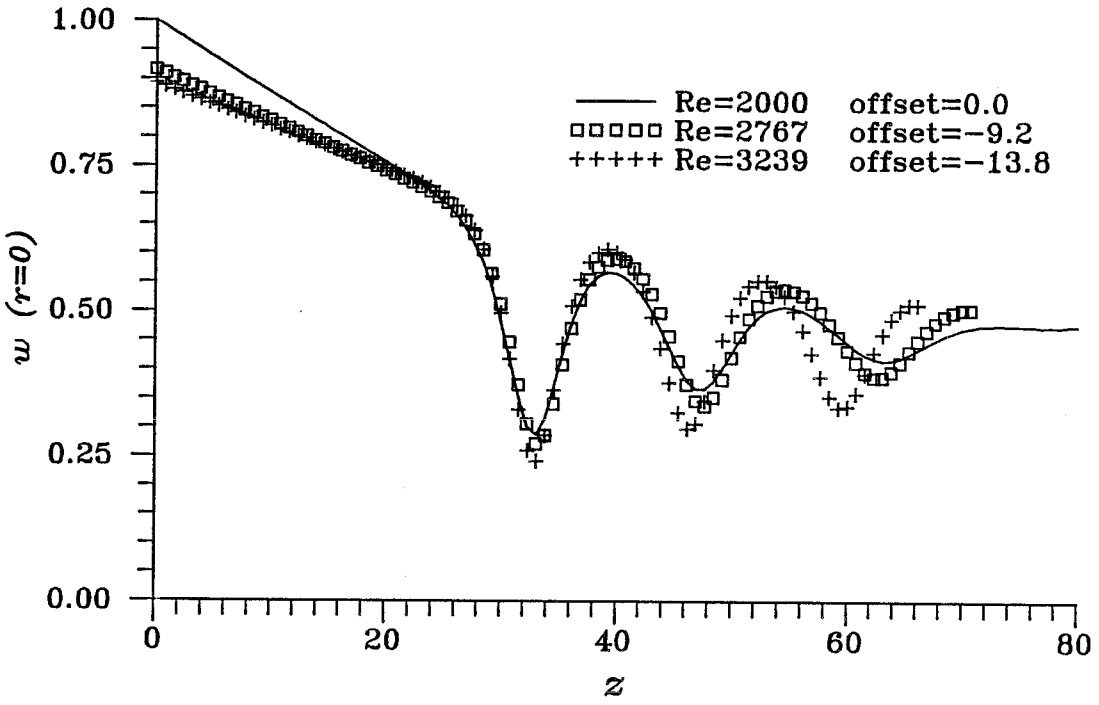

Figure 3.31 Centerline axial velocity versus **offset** axial position for Re = 2000, Re = 2767 and Re = 3239 with $V = 0.7846$

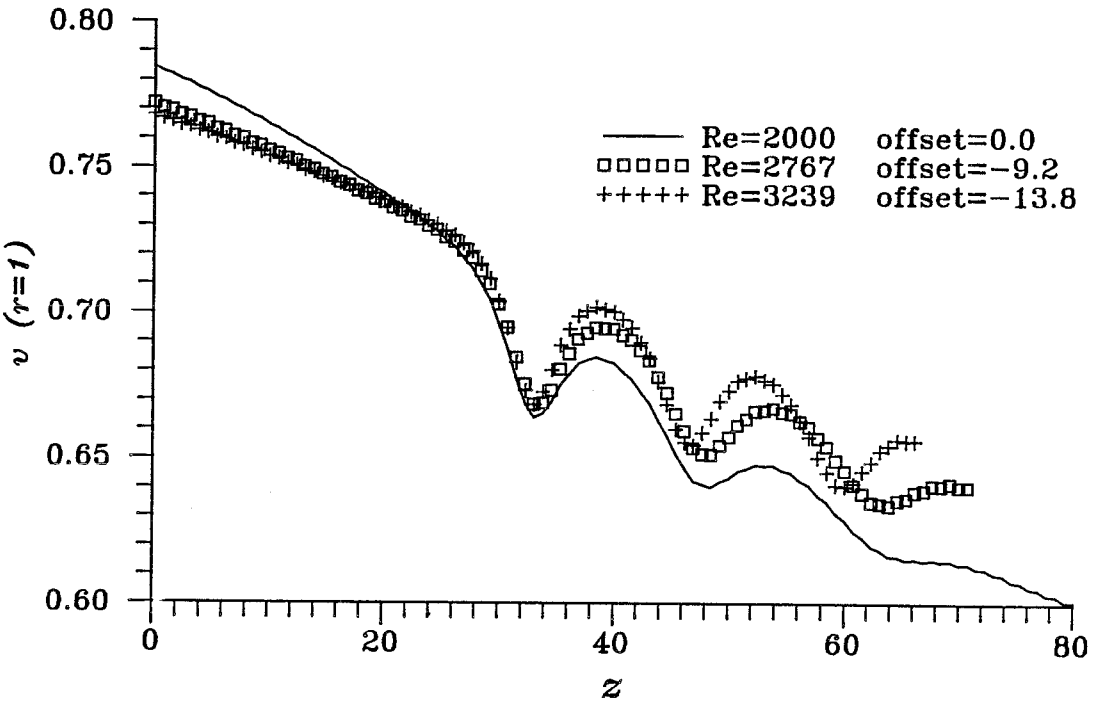

Figure 3.32 Azimuthal velocity ($r = 1$) versus **offset** axial position for Re = 2000, Re = 2767 and Re = 3239 with $V = 0.7846$

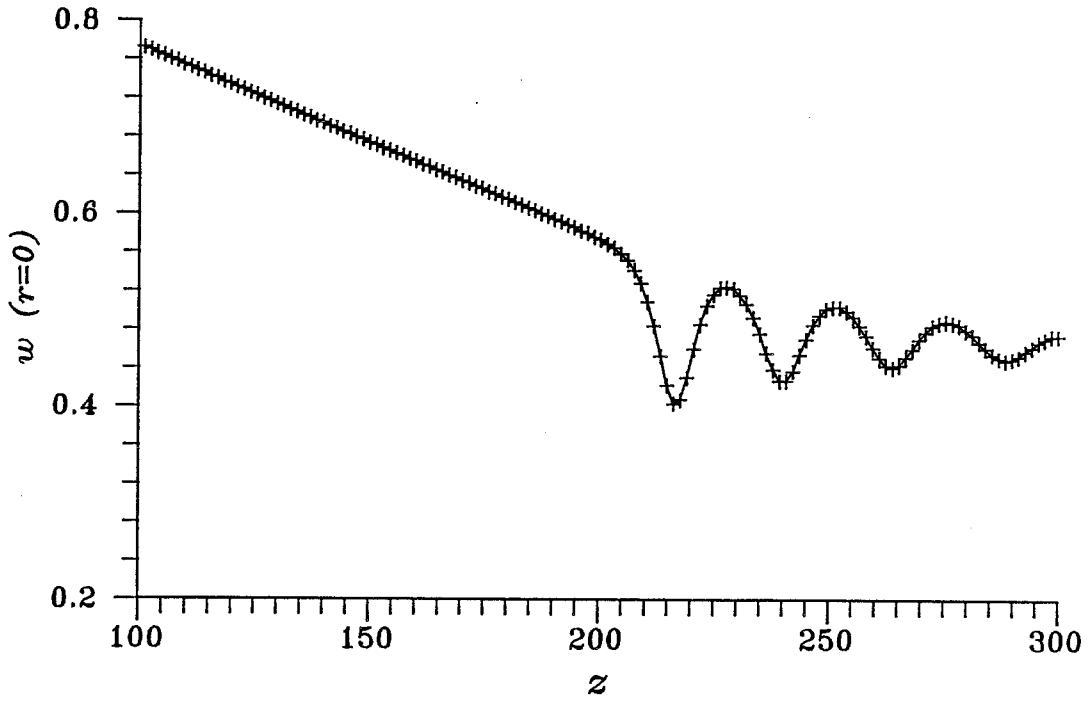

Figure 3.33 Centerline axial velocity versus axial position for Re = 9977 with $V = 0.7770$

was adequately resolved by the computational grid. Short-period, numerical noise was not observed at this high Reynolds number. Solutions are not presented for Re greater than 9977, since those solutions appeared to be significantly (and artificially) affected by the presence of the downstream boundary. The downstream boundary condition is satisfactory at lower Reynolds numbers, since then transition occurs sufficiently far upstream that the oscillatory flow downstream of transition is damped to a near columnar state in the vicinity of the outflow boundary.

The effect of increased axial-node spacing, h_z, on the solution with Re = 9977 is explored in Figure (3.34). Two profiles of centerline axial velocity are shown, one corresponding to $I = 105$ and the other, $I = 209$. Qualitatively, the profiles are quite similar — the solution with $I = 105$ successfully reproduces transition and the oscillatory flow downstream of transition. However, with $I = 105$, the computational grid does not adequately resolve flow gradients, leading to the emergence of short-period, numerical noise upstream of transition.

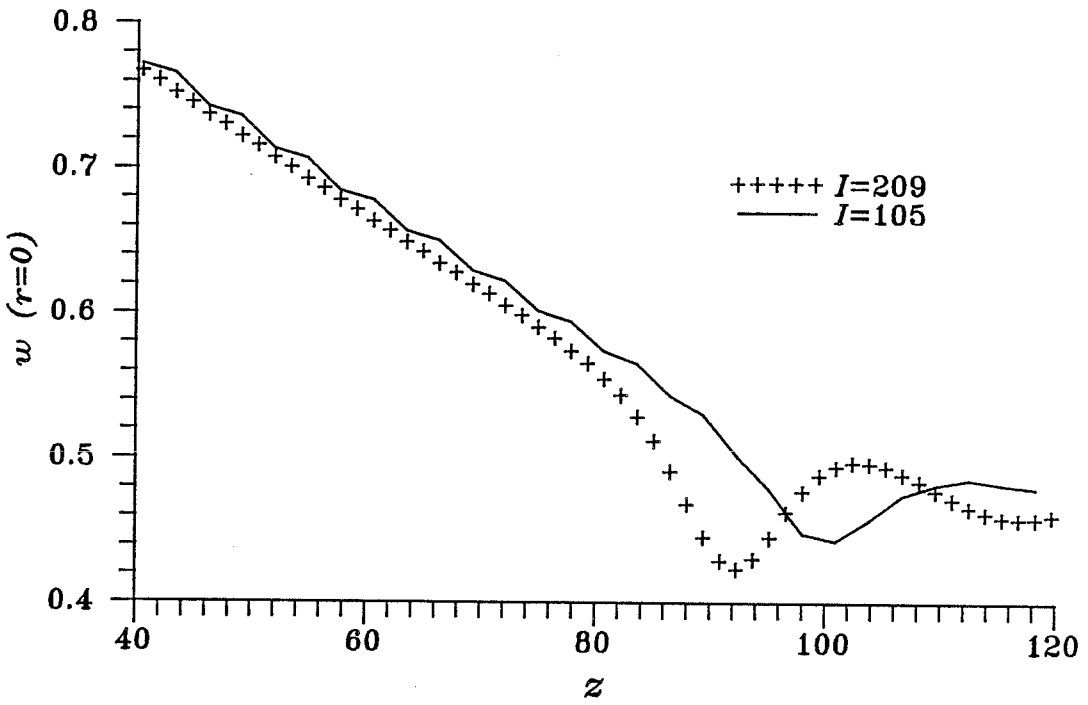

Figure 3.34 Centerline axial velocity versus axial position for Re = 3875 with $V = 0.7770$ using two different axial node spacings

3.3.9 Continuation in Re from 10 to 20440 with V=0.7770: Fine Grid

Solutions for Reynolds numbers greater than 10000 were obtained by lengthening the computational domain and decreasing the axial node spacing. It was reported in Section (3.3.8) that for these high Reynolds numbers (with V fixed), a longer domain is necessary to insure that flow oscillations are of negligible amplitude at the outflow boundary. It was also found, by experimentation, that it is necessary to reduce axial-node spacing to prevent the appearance of short-period, numerical noise when Reynolds number is much larger than 10000.

By increasing Z and decreasing h_z, solutions were computed through continuation in Re for Reynolds number ranging between 10 and 20440, with V fixed at 0.7770. In comparison with the grid parameters selected in Section (3.3.8), I and Z were increased to 833 and 600, respectively, and J was decreased to 14. The nearly fourfold increase in the number of nodes in the axial direction required a decrease in J because of the limited amount of available computer memory. With

$J = 14$, it is assumed that computed solutions are not independent of increased J (see Section (3.1)). However, since solutions with $J = 14$ capture all the physical behavior evident in solutions with $J = 27$, an increase in h_r does not invalidate the results.

Figure (3.35) shows centerline axial velocity profiles corresponding to three different solutions computed during the continuation process. The plots also include axial velocity profiles on the line $r = 4h_r$. For the sake of future discussion, the solutions for Re = 7063, Re = 15705 and Re = 20440 will be referred to as NS701, NS703 and NS705, respectively.

The effects of increased Reynolds number are: the downstream movement of the transition point, the lengthening of the resulting wave train, the increase of wave amplitude and the decrease in the rate of change of wave wavelength as a function of axial position.

The purpose of plotting off-centerline axial velocity with centerline axial velocity in Figure (3.35) is to show that local extrema of the profiles occurred at the same axial positions. This was found to be true, not only of the three cases presented in Figure (3.35), but of many of the other solutions discussed in Section (3.3). The exceptions to this general observation are those examined in Sections (3.3.1)—(3.3.4). In these solutions, for which reversed flow is present, the positions of minima are not coincident, as is apparent in Figure (3.6), showing that isolated regions of reversed flow are skewed with respect to the axis of symmetry and the inflow boundary.

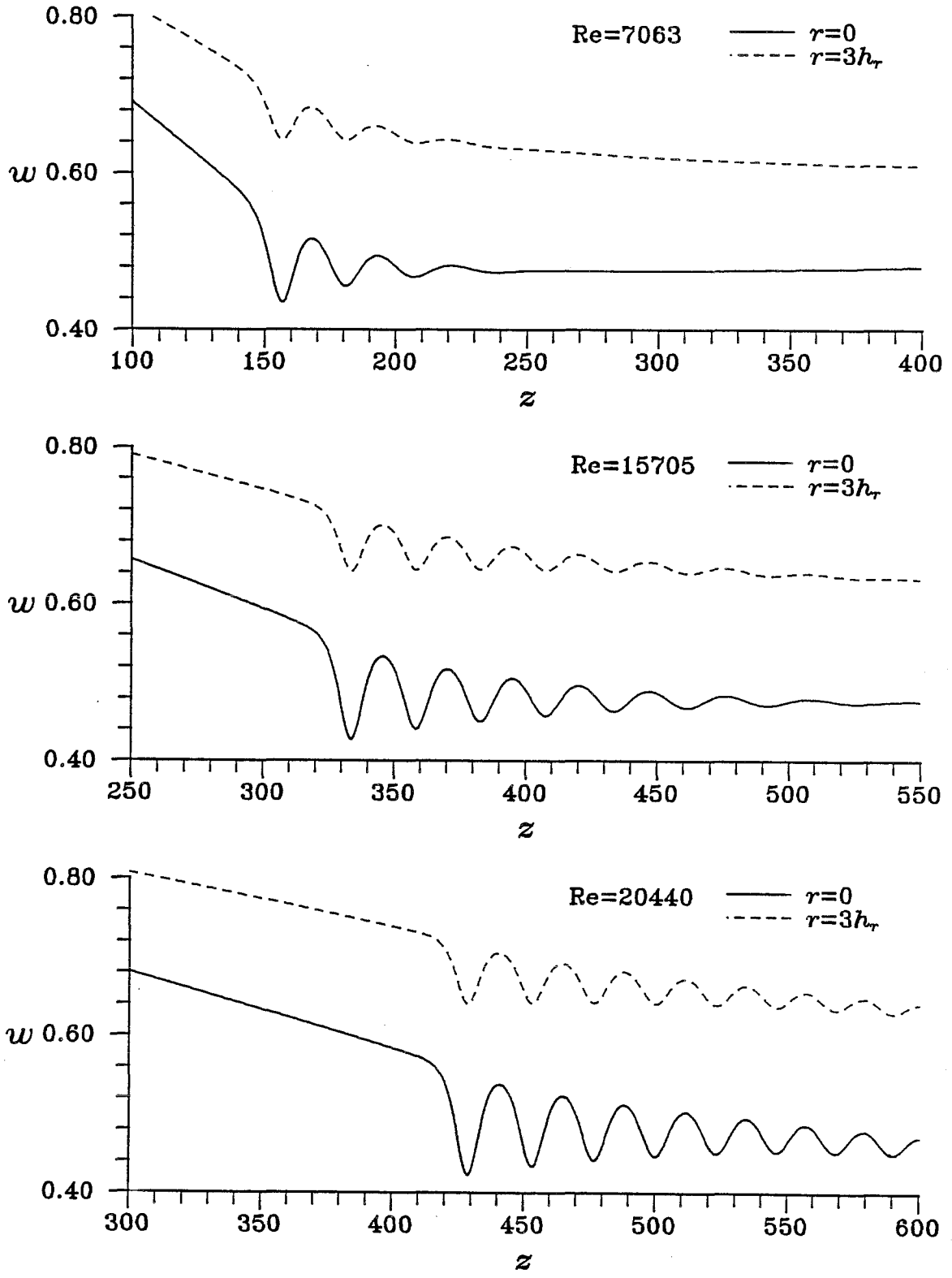

Figure 3.35 Axial velocity versus axial position along $r = 0$ and $r = 3h_r$ for Re = 7063, Re = 15705 and Re = 20440 with $V = 0.7770$

3.4 Definition of Transition Point

Several solutions of the Navier-Stokes equations were presented in the last section that exemplify the tendency of trailing vortices to make a transition between two distinctly different flow states. A "point" of transition was loosely defined as the location at which there is a significant change of slope in the centerline axial velocity profile. Closer examination of the solutions reflecting transition indicates, however, that there is a region, several core radii in length, over which the flow changes character. In this section a systematic and appealing definition of transition-point position, independent of the detailed behavior of the flow in the transition region, will be proposed. It is seen in Section (4.4) that use of this definition reveals a significant relationship between transition-point position and Reynolds number.

A tabulation of transition-point positions for many of the solutions computed in Section (3.3) is also included in this section.

It was observed from the results presented in Section (3.3.6) that as Reynolds number increases, the spatially oscillatory flow downstream of the transition region more closely approximates a periodic wave. Wave damping decreases and the axial extent of flow oscillation increases as Reynolds number increases. It was also found in Section (3.3.7) that wavelength of the oscillatory flow, as a function of axial position, is nearly constant, just downstream of transition, as Reynolds number is increased. Some of these observations can be quantified by tabulating the axial positions of local maxima and minima in the centerline axial velocity, as shown in Figure (3.35). By continuity, the positions of these extrema are equivalent to the positions at which radial velocity vanishes, since extrema of centerline axial velocity have the same positions as extrema of off-axis axial velocity (Figure (3.35)). However, the positions at which radial velocity vanishes are easier to discern than the extrema positions of axial velocity.

Plots of radial velocity versus axial position, along the lines $r = h_r$ and $r = 4h_r$ in Figure (3.36) for the cases NS701, NS703 and NS705. In each of the three plots,

extrema index (i)	NS701 ζ_i	NS703 ζ_i	NS705 ζ_i	extrema type
1	156.5	333.5	428.5	minimum
2	168.0	345.5	440.5	maximum
3	181.0	358.0	453.0	minimum
4	193.0	370.0	464.5	maximum
5	207.0	382.5	476.5	minimum
6	221.0	394.5	488.0	maximum
7	238.0	407.5	500.0	minimum
8	257.5	420.0	511.5	maximum
9	-	433.5	523.0	minimum
10	-	447.0	534.0	maximum
11	-	461.0	546.0	minimum
12	-	475.5	557.0	maximum
13	-	491.0	568.5	minimum
14	-	508.0	579.0	maximum
15	-	526.0	590.0	minimum
16	-	546.5	600.0	maximum

Table 3.1 Positions of radial velocity vanishing points and extrema classification for the cases NS701, NS703 and NS705

radial velocity is constant and positive, upstream of transition. As centerline axial velocity rapidly drops in the transition region, radial velocity increases. Since the flow is incompressible, an increase in mass flux in the radial direction must accompany a decrease of mass flux in the axial direction. Peak radial velocity is several times larger, in magnitude, than the constant value of radial velocity in the approach flow. As an extremum in centerline axial velocity is approached, radial velocity decreases in magnitude linearly, as a function of z, and vanishes at the position of the extremum.

The positions of points at which radial velocity vanishes (recorded to the nearest half of a core radius), ζ_i, and the type of axial-velocity extrema (i.e., minimum or maximum) represented are tabulated in Table (3.1) for the cases NS701, NS703 and NS705. Wavelength of flow oscillation, λ_i, as a discrete function of axial position, is determined by computing the distance between successive axial-velocity maxima and successive axial-velocity minima. Computed wavelengths are tabulated in

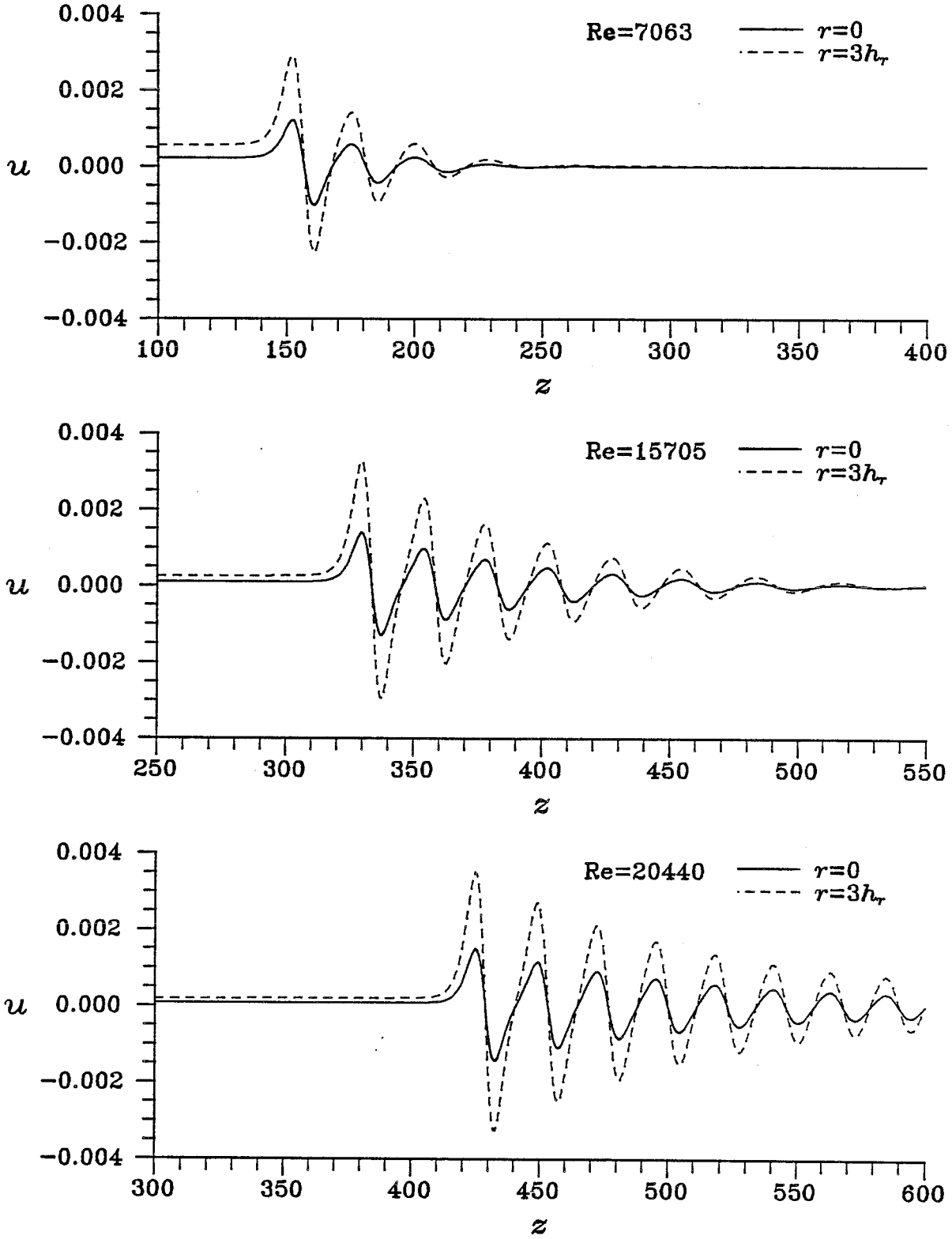

Figure 3.36 Radial velocity versus axial position along $r = h_r$ and $r = 3h_r$ for Re = 7063, Re = 15705 and Re = 20440 with $V = 0.7770$

wavelength index (i)	extrema pair	NS701 λ_i	NS703 λ_i	NS705 λ_i	extrema type
1	1-3	24.5	24.5	24.5	min-min
2	2-4	25.0	24.5	24.0	max-max
3	3-5	26.0	24.5	23.5	min-min
4	4-6	28.0	24.5	23.5	max-max
5	5-7	31.0	25.0	23.5	min-min
6	6-8	36.5	25.5	23.5	max-max
7	7-9	-	26.0	23.0	min-min
8	8-10	-	27.0	22.5	max-max
9	9-11	-	27.5	23.0	min-min
10	10-12	-	28.5	23.0	max-max
11	11-13	-	30.0	22.5	min-min
12	12-14	-	32.5	22.0	max-max
13	13-15	-	35.0	21.5	min-min
14	14-16	-	38.5	21.0	max-max

Table 3.2 Computed wavelengths from tabulated positions of successive minima and successive maxima for cases NS701, NS703 and NS705

Table (3.2) for cases NS701, NS703 and NS705. Comparison of λ_i between the cases NS701 and NS703 leads to two conclusions. First, λ_i increases at a slower rate with axial position as Reynolds number increases. Second, λ_1 is approximately the same in both cases, as was previously suggested by the overlay of offset velocity profiles in Figure (3.30). λ_1 is also approximately the same in all three cases. However, in case NS705, λ_i does not increase with axial position but instead decreases slowly. This inconsistent behavior is attributed to the presence of the outflow boundary. In part, the outflow boundary conditions demand that the centerline axial velocity experience a local maximum or minimum at that boundary, and since the flow in case NS705 is in an oscillatory state at the outflow boundary, the presence of that boundary must significantly affect global solution behavior.

The transition "point" of a trailing vortex is consistently observed to occur a distance λ_1 upstream of the leading local maximum in centerline axial velocity, when λ_i does not increase too quickly with axial position (i.e., when the Reynolds number is sufficiently large). For example, Figure (3.37) shows the profile of center-

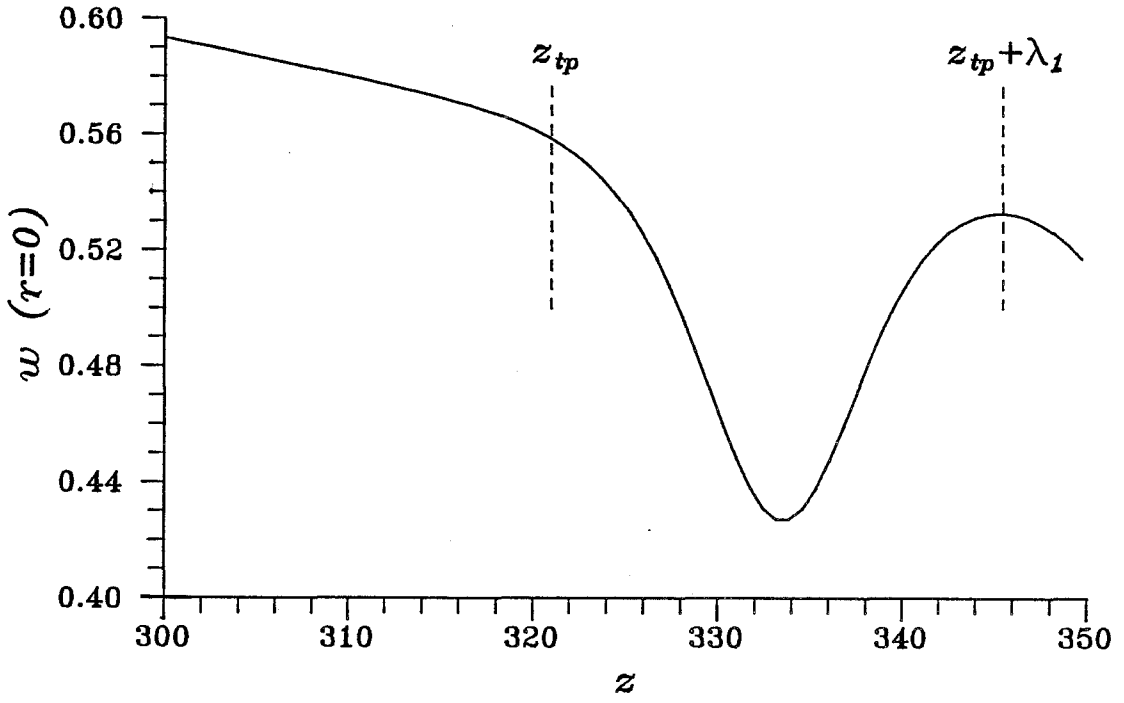

Figure 3.37 Centerline axial velocity profile for case NS703 in vicinity of transition point

line axial velocity in the vicinity of the transition point and a line intersecting the profile a distance λ_1 upstream of the velocity maximum at $z = 345.5$. Upstream of the intersection point, centerline axial velocity varies nearly linearly with axial position, departing only slightly from a linear path in the vicinity of the intersection point. Downstream of the intersection point, however, the centerline axial velocity rapidly decreases. In the rest of this work, the transition point will be *defined* to occur a distance λ_1 upstream of the global maximum of centerline axial velocity. The position of the transition point will be denoted by z_{tp}.

This definition of transition point location is also motivated by the observed character of the flow in the transition region. Referring again to Figure (3.36), the portion of the profile just downstream of the intersection point is qualitatively very similar to other profile segments downstream of local maxima. This makes sense, since with increasing Reynolds number, the flow upstream of transition more closely resembles a columnar flow in which $w_z = 0$, so that if the flow is to make a smooth transition to an oscillatory state, it should do so at a minimum or a

maximum of the resulting wave. However, since axial velocity invariably decreases downstream of the transition point, an axial-velocity minimum does not occur at that point. It is now postulated that the wave train resulting from transition is bounded on the upstream end by a flow state approximating an axial velocity maximum. The position of this flow state is approximately equivalent to z_{tp}, since flow wavelength was found to be nearly constant with respect to z in the vicinity of the transition region.

Values of λ_1 and z_{tp} for several of the solutions reported in Section (3.3) are tabulated in Table (3.3).

3.5 Criticality of Computed Flows

In this section the criticality of the solutions presented in Section (3.3.9) is determined using the approach outlined in Section (C.2). Benjamin (1962) introduced the notion of flow criticality in his conjugate-state theory of vortex breakdown; his ideas are discussed further in Chapter 1 and Appendix C. Benjamin's analysis was limited to axisymmetric, inviscid flows, but should be relevant to this work, since solutions for high Reynolds numbers are computed.

Flow criticality is a function of axial position. At a particular station, flow criticality is dependent only on $\psi(r)$ and $\Gamma(r)$ at the station, not on the axial gradients of these functions. Thus, axial gradients in the flow are assumed to be negligibly small (i.e., the Reynolds number is assumed to be sufficiently high). Flow criticality at a station is measured by the ability of an inviscid columnar vortex, with the same streamfunction and circulation profiles as at the station, to support *standing* waves of infinitesimal amplitude. Substitution of

$$\psi(r,z) = \psi_o(r) + \epsilon e^{ikz}\psi_1(r) \tag{3.2}$$

$$\eta(r,z) = \eta_o(r) + \epsilon e^{ikz}\eta_1(r) \tag{3.3}$$

$$\Gamma(r,z) = \Gamma_o(r) + \epsilon e^{ikz}\Gamma_1(r), \tag{3.4}$$

Run	Cont.	Re	V	a	I	J	Z	R	z_{tp}	λ_1	η_o
NS272	Re	200.	1.0000	0.0	209	27	20	2	-	-	i
NS276	Re	325.	1.0000	0.0	209	27	20	2	-	-	i
NS278	Re	437.	1.0000	0.0	209	27	20	2	-	-	i
NS280	Re	559.	1.0000	0.0	209	27	20	2	-	-	i
NS284	Re	829.	1.0000	0.0	209	27	20	2	-	-	i
NS329	V	1000.	0.7808	0.0	209	27	80	2	-	-	i
NS333	V	1000.	0.7955	0.0	209	27	80	2	6.5	10.5	i
NS339	V	1000.	0.8048	0.0	209	27	80	2	1.5	8.5	i
NS968	V	200.	1.1563	0.0	105	27	20	2	-	-	i
NS970	V	200.	1.0509	0.0	105	27	20	2	-	-	i
NS972	V	200.	0.9188	0.0	105	27	20	2	-	-	i
NS974	V	200.	1.0000	0.0	105	27	20	2	-	-	i
NS1121	Re	133.8	1.0000	0.0	105	27	20	2	-	-	i
NS1122	Re	147.2	1.0000	0.0	105	27	20	2	-	-	i
NS1124	Re	288.1	1.0000	0.0	105	27	20	2	-	-	i
NS403	V	2000.	0.7677	0.0	105	27	80	2	-	-	e
NS404	V	2000.	0.7791	0.0	105	27	80	2	33.0	20.0	e
NS405	V	2000.	0.7823	0.0	105	27	80	2	28.5	15.5	e
NS406	V	2000.	0.7846	0.0	105	27	80	2	25.0	14.5	e
NS409	Re	2767.	0.7846	0.0	105	27	80	2	34.5	14.5	e
NS410	Re	3239.	0.7846	0.0	105	27	80	2	39.5	13.5	e
NS481	Re	3875.	0.7770	0.0	209	27	300	2	78.0	25.0	e
NS483	Re	4221.	0.7770	0.0	209	27	300	2	94.0	23.5	e
NS487	Re	5970.	0.7770	0.0	209	27	300	2	122.0	24.0	e
NS491	Re	7289.	0.7770	0.0	209	27	300	2	149.5	23.5	e
NS493	Re	7929.	0.7770	0.0	209	27	300	2	162.5	23.5	e
NS495	Re	8536.	0.7770	0.0	209	27	300	2	175.0	23.5	e
NS497	Re	9118.	0.7770	0.0	209	27	300	2	187.5	23.5	e
NS500	Re	9977.	0.7770	0.0	209	27	300	2	205.0	23.0	e
NS700	Re	2104.	0.7770	0.0	833	14	600	2	39.5	24.5	e
NS701	Re	7063.	0.7770	0.0	833	14	600	2	143.5	24.5	e
NS702	Re	13143.	0.7770	0.0	833	14	600	2	268.5	24.5	e
NS703	Re	15705.	0.7770	0.0	833	14	600	2	321.0	24.5	e
NS704	Re	18095.	0.7770	0.0	833	14	600	2	369.5	24.5	e
NS705	Re	20440.	0.7770	0.0	833	14	600	2	416.0	24.5	e
NS981	V	200.	0.8017	0.0	105	27	20	2	-	-	e
NS983	V	200.	0.7251	0.0	105	27	20	2	-	-	e
NS986	V	200.	0.6620	0.0	105	27	20	2	-	-	e
NS988	V	200.	0.7969	0.0	105	27	20	2	-	-	e

Table 3.3 Recorded solutions and transition-point positions

into the Euler equations (see Appendix C for details) yields, for small ϵ, an eigenvalue problem for $\psi_1(r)$ and k^2. If all eigenvalues, k_i^2, are negative, then the flow cannot support standing waves and is supercritcial. If one or more eigenvalues are positive then the flow is subcritical.

Discrete spectra of eigenvalues were computed at each axial station for the solutions examined in Section (3.3.9). In Figure (3.38), the eigenvalue of maximum value, β, is shown plotted against axial position for the cases NS701, NS703 and NS705. In each case, it is observed that the flow is supercritcal between the inflow boundary and a point several core radii *downstream* of the transition point. The flows are driven towards a subcritical state by the rapid decrease of centerline axial velocity. Once the flows become subcritical, they remain subcritical throughout most of the remaining portion of the computational domain. Further investigation determined that transition occurred while the flow was supercritical in all other cases in which transition was observed.

3.6 Comparison with Unsteady Solutions of NS equations

Several investigators, including Krause et al. (1983); Hafez et al. (1987); Brown and Lopez (1988); and Menne (1988), have studied the unsteady characteristics of the breakdown of vortices in pipes and in unbounded flows through numerical integration of the time-dependent Navier-Stokes equations. These studies assumed the vortical flows to be rotationally symmetric. Nakamura et al. (1986) used the vortex filament method to simulate numerically simulate vortex breakdown without the assumption of rotational symmetry. The time-integration approach has successfully reproduced many aspects of the experimentally observed behavior of vortex breakdown, but in most investigations in which this approach was used, steady-state solutions with reversed flow were not found. Hafez et al. (1987) solved the time-dependent Navier-Stokes equations as well as the steady-state Navier-Stokes equations and found that steady-state solutions with reversed flow could be obtained through time integration. Furthermore, for the specific case of flow through

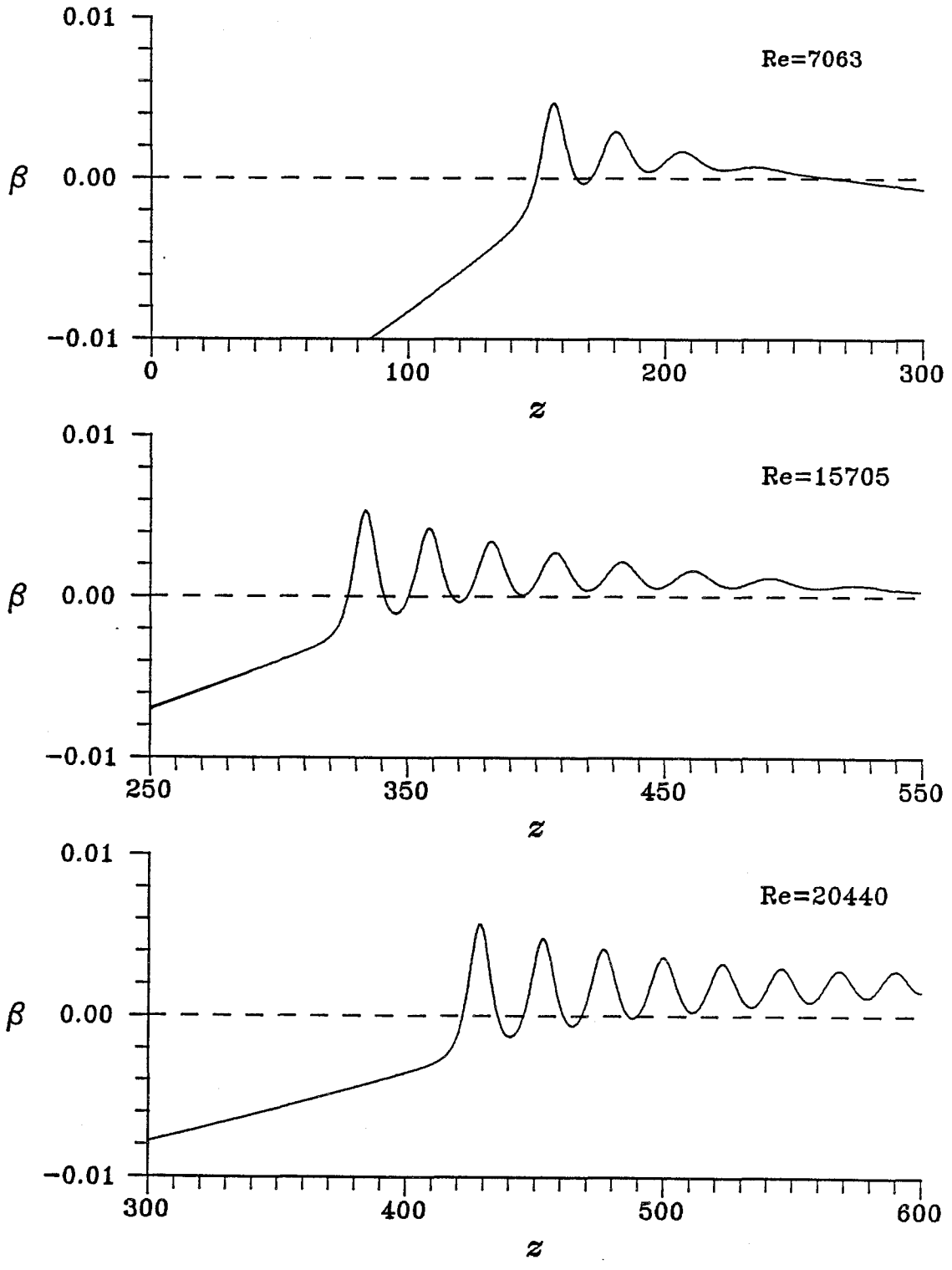

Figure 3.38 Maximum eigenvalue versus axial position for the three cases NS701, NS703 and NS705

a frictionless pipe (similar to the problem to be described in Section (3.6.1)) with Re = 400 and $V = 1.15$, they found the solution of the time-dependent equations, in the steady-state limit, to be equivalent to the solution of the steady-state equations, thus demonstrating the stability of the steady-state solution.

3.6.1 Comparison with Results of Brown and Lopez

It is not clear why steady-state solutions of the time-dependent equations have been difficult to obtain, although it appears that the transient behavior of the breakdown bubble, during its formation, leads the time-dependent solution to a periodic or quasi-periodic solution of the time-dependent equations. For example, the large-time behavior of a time-dependent solution of the Navier-Stokes equations, computed by Brown and Lopez (1988), for flow through a frictionless pipe was found to be approximately periodic (Lopez (1988)). In their evolutionary solution, two and sometimes three breakdown bubbles were found.

Since the flow model used by Brown and Lopez is quite similar to the Navier-Stokes model described in Chapter 2, only small changes in the latter model were necessary to allow a direct comparison between the time-dependent solution calculated by Brown and Lopez and solutions of the steady-state Navier-Stokes equations. The focus of this section is such a comparison.

As stated above, the flow model considered by Brown and Lopez is similar to the one described in Chapter 2. The only significant difference is that Brown and Lopez assumed flow through a frictionless pipe; on boundary S2, streamfunction was specified to be constant and $\frac{\partial v}{\partial r} = 0$ was enforced. On the inflow boundary, S1, Brown and Lopez specified the following conditions (these conditions have been put in nondimensional form, using core radius at the inflow boundary as a length scale and axial velocity at the inflow boundary, for $r \to \infty$, as a velocity scale):

$$\Gamma(0,r) = \Gamma_o(r) = \frac{V_c}{(1-e^{-1})}\left(1-e^{-r^2}\right) \equiv V\left(1-e^{-r^2}\right) \tag{3.5}$$

$$\psi(0,r) = \psi_o(r) = \frac{1}{2}r^2 + \frac{W_c}{2}\left(1-e^{-r^2}\right) \tag{3.6}$$

$$\eta(0,r) = \eta_o(r) = 2W_c r e^{-r^2}, \tag{3.7}$$

where $V \equiv \frac{V_c}{(1-e^{-1})} \approx 1.582V_c$ and $W_c \equiv a$. The circulation and streamfunction profiles, (3.5) and (3.6), reflect the following choice of azimuthal velocity, v, and axial velocity, w, profiles:

$$v_o(r) = \frac{V}{r}\left(1 - e^{-r^2}\right) \tag{3.8}$$

$$w_o(r) = 1 + ae^{-r^2}. \tag{3.9}$$

The vorticity boundary condition, (3.7), is derived from the definition of azimuthal vorticity, $\eta = u_z - w_r$, assuming quasi-cylindrical flow at the inflow boundary. Brown and Lopez specified conditions on S3 and S4 similar to those described in Section (2.3.1).

Solutions of the steady-state equations were obtained using the boundary conditions of the Brown and Lopez model. The Neumann condition on v on the S2 boundary was placed in discrete form, using a second-order accurate, one-sided difference expression. Brown and Lopez integrated the time-dependent Navier-Stokes equations, assuming Re = 250, $V_c = 1.50$ or $V \approx 2.373$, and $W_c = 1.25$. Their choice of grid parameters was $I = 351$, $Z = 35$, $J = 51$ and $R = 5$. Solutions of the steady-state equations were computed with continuation in V for V ranging between 0.5 and 2.5672, with Re = 250. Solutions were also computed by continuation in V after obtaining a solution at $V = 2.4718$ through continuation in Reynolds number. The grid parameters I, Z, J and R were specified to be 105, 45, 27 and 3, respectively. Unfortunately, because of limited computer memory, solutions could not be obtained for a computational mesh as refined as that used by Brown and Lopez. It was found, however, over the course of preliminary calculations, that the computational domain needed to be lengthened from 35 to 45 to prevent the development of spurious solutions.

Solutions were first computed by continuation in V from $V = 0.5$ to $V = 2.5672$. A portion of the computed solution path, for V between 2.3692 and 2.5672, is

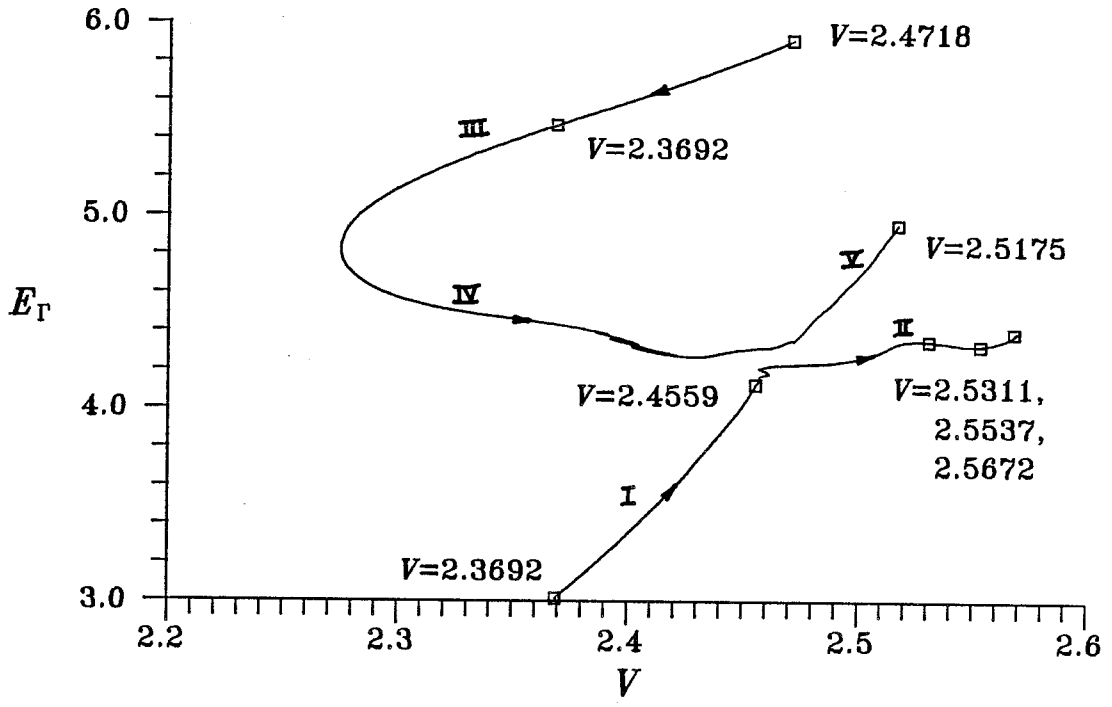

Figure 3.39 Solution paths as represented by $E_\Gamma(V)$ with Re = 250

shown in Figure (3.39). It lies below a second path, which was obtained through a different continuation procedure to be described below. Contour plots of ψ for selected points marked on the former path are included in Figure (3.40), and corresponding plots of centerline axial velocity versus axial position are shown in Figure (3.41).

At $V = 2.3692$, approximately the vortex strength assumed by Brown and Lopez, the flow is quasi-cylindrical throughout $\Re$. This is a quite different picture than that predicted by the time-dependent solution, which was found to contain prominent regions of reversed flow. As V was increased to 2.4559, a transition point developed. The transition point is located at $z \approx 10$, and the flow downstream of the transition point is observed to contain a small bubble of reversed flow. As V is increased beyond 2.4559, four indistinct limit points are found in the neighborhood of $V = 2.46$. Solutions following these limit points indicate the presence of a significant amount of numerical noise, the magnitude of which increases with increased V. Also, beyond the limit points, the solution path is of a

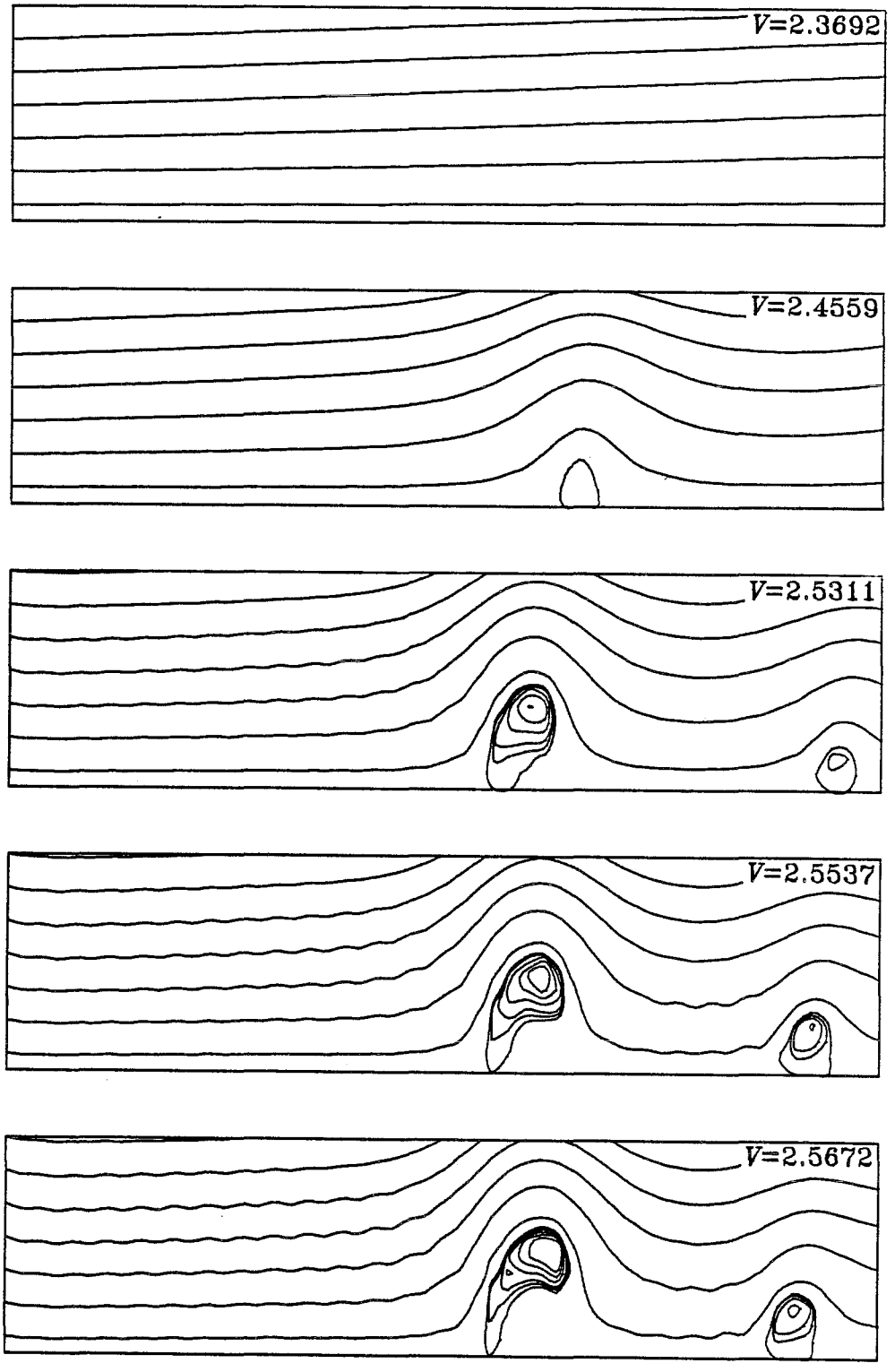

Figure 3.40 Contour plots of ψ for selected points on lower solution path shown in Figure (3.39) ($0 \leq r \leq 1.5$, $0 \leq z \leq 22.5$)

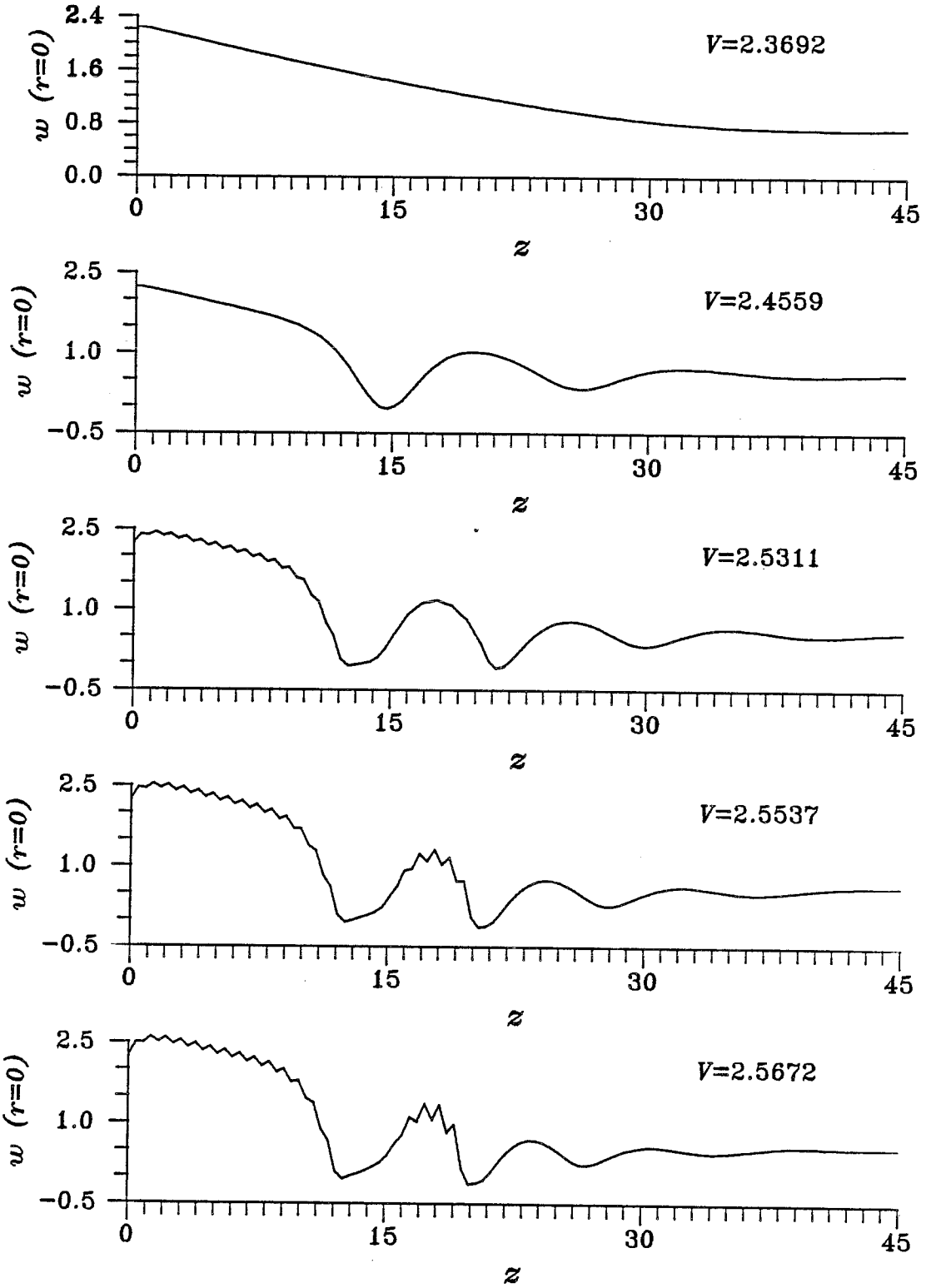

Figure 3.41 Centerline axial velocity versus axial position for selected points on lower solution path shown in Figure (3.39)

markedly different slope than the portion of the path between the solution points at $V = 2.3692$ and $V = 2.4559$.

The point at $V = 2.3692$ appears to represent a stable solution of the Navier-Stokes equations. Between the initial point on the solution path, $V = 0.5$, and the point at $V = 2.3692$, no bifurcation points or limit points are observed. The flow for the case $V = 0.5$ is nearly columnar. Also, the Howard and Gupta condition, (3.2), which is a sufficient condition for the stability of columnar flows, is found to be satisfied throughout $\Re$, when $V = 2.3692$. This does not prove the stability of the solution point but strongly suggests it, since the axial gradients of flow quantities for this solution point are everywhere small.

Length scales in the flow at $V = 2.4559$ are adequately resolved by the computational mesh, and the solution at this point is smooth. However, solutions for $V > 2.46$ are not smooth and exhibit short-period, numerical noise. Further investigation indicated the presence of numerical noise even when the number of nodes in the z-coordinate direction, I, was more than doubled (with a corresponding decrease in J).

Just prior to the development of noise, as signalled by the passage through a set of limit points, a small bubble of reversed flow arose, as seen in Figure (3.40) for $V = 2.4559$. It is noted that at the point at which reversed flow develops, the flow is quasi-cylindrical over several core diameters between the inflow boundary and the transition point. In contrast, transition points occurred near the inflow boundary in the solutions examined in Section (3.3) that contained reversed flow. Further work must be done to determine precisely why the initial development of reversed flow, when the upstream flow is quasi-cylindrical, is a limiting state beyond which steady-state solutions, with physical meaning, cannot be computed through continuation in V.

A second solution path, shown in Figure (3.39), was traced by finding a solution point not on the path described above. This point was computed by first executing continuation in V from 0.5 to 2.4718 with $\mathrm{Re} = 100$. During this procedure several

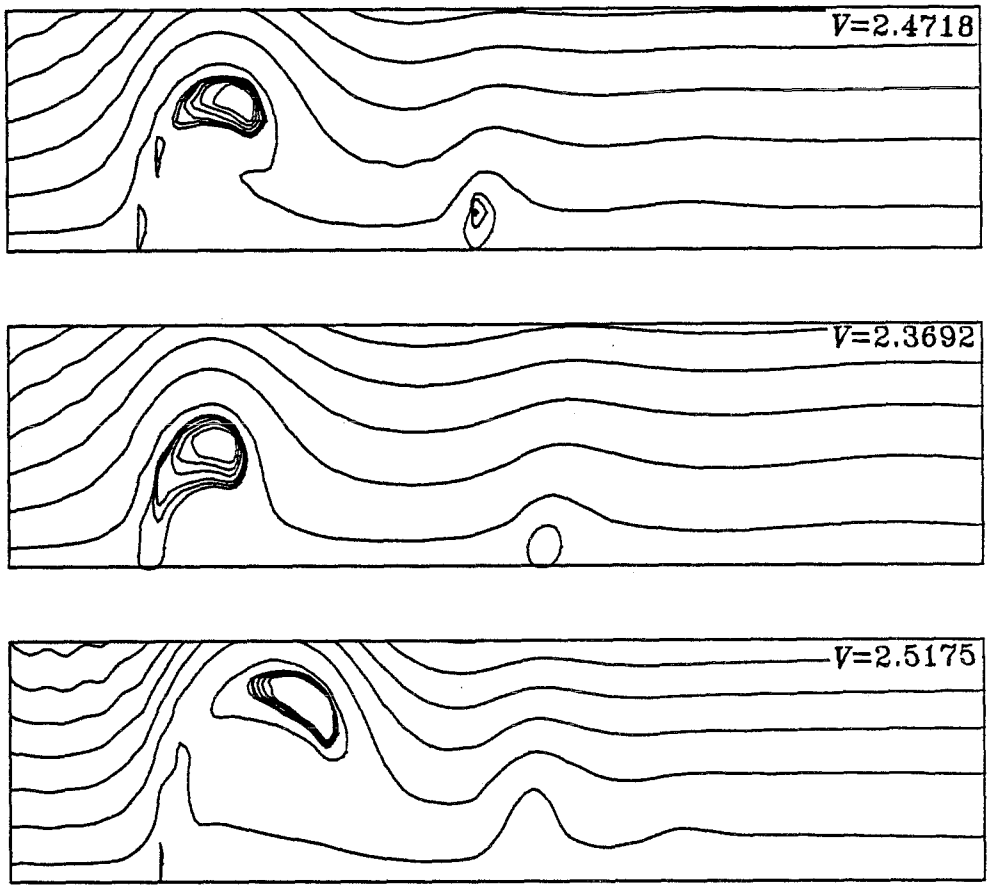

Figure 3.42 Contour plots of ψ for selected points on upper solution path shown in Figure (3.39) ($0 \leq r \leq 1.5$, $0 \leq z \leq 22.5$)

limit points were encountered, but numerical noise was not observed. Reversed flow was observed, but in these cases the flow was not quasi-cylindrical between the inflow boundary and the breakdown bubble. Continuation in Reynolds number was then performed, using the solution point found for Re = 100 as a starting point, to compute a solution point for Re = 250 and $V = 2.4718$. The latter point is marked in Figure (3.39). With this point a second solution path was computed via continuation in V.

Contour plots of ψ for selected points on the second path are shown in Figure (3.42). Corresponding profiles of centerline axial velocity are included in Figure (3.43). A limit point was found at $V = 2.2748$, when the solution path was followed in the direction of decreasing V, starting at $V = 2.4718$. Midway between

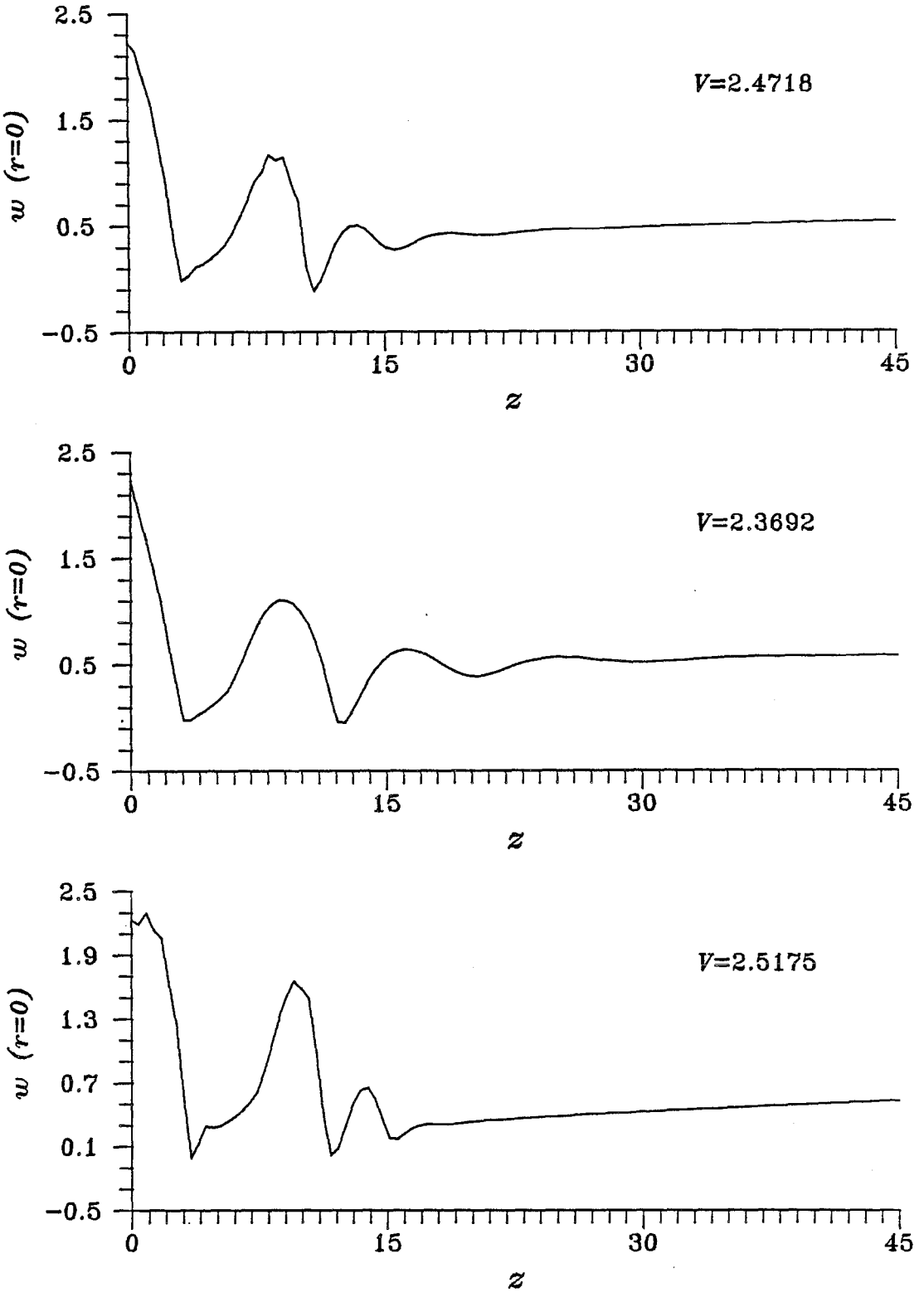

Figure 3.43 Centerline axial velocity versus axial position for selected points on upper solution path shown in Figure (3.39)

the limit point and the starting point, a solution was computed for $V = 2.3692$, the same vortex strength for which a solution was computed on the lowermost solution path. However, in the solution on the upper path, two regions of reversed flow are found that are similar in appearance to the two reversed flow regions observed in the large-time solution presented by Brown and Lopez. (Note that in the contour plots of streamfunction shown in both Figures (3.40) and (3.42), the r-coordinate direction is stretched with respect to the z-coordinate direction so that the breakdown bubbles appear "wider" than those bubbles shown in Figure (3.7).) One difference between the steady-state solution and the large-time solution calculated by Brown and Lopez is that the breakdown bubbles in the steady-state solution are upstream of the corresponding bubbles in the large-time solution. However, in the time sequence of contour plots provided by Brown and Lopez, it is apparent that the bubbles were still moving upstream at the largest time for which plots were provided.

Beyond the limit point at $V = 2.2748$, V increases with increasing arclength. On the lower branch of the fold, the breakdown bubbles occur at about the same axial positions as on the upper branch. Numerical noise is observed in solutions when V exceeds about 2.4. The onset of noise is signalled by passage through another set of limit points, encountered in the neighborhood of $V = 2.4$. At $V \approx 2.47$, the path takes an abrupt change in direction. The new direction is nearly parallel to the direction of the portion of the lower path between the solution points at $V = 2.3692$ and $V = 2.4559$.

Since the algorithm used in this work was incapable of locating Hopf bifurcation points, the stability of the solutions on the upper path is open to question. If such points are present on the upper path, then the inability of the time-integration algorithm to compute solutions, equivalent to equilibrium solutions on the path in the large-time limit, is not surprising. However, this does not explain why the time-integration algorithm failed to compute the equilibrium solution on the lower path at $V = 2.3692$, which is assumed to be stable. The answer may be that

for the initial condition chosen for the integration of the time-dependent equations (columnar flow – defined by the flow specified at the inflow boundary), the resulting transient flow develops reversed flow, and that the region of reversed flow grows and moves upstream through the physical mechanisms discussed in the report by Brown and Lopez. Once fully developed, the breakdown bubble could sustain themselves by achieving a periodic or quasi-periodic state. This description is at odds, though, with the calculations of Hafez et al. (1987), in which a solution, steady in the large-time limit, was found with reversed flow.

Future work should be directed towards the determination of the sensitivity of large-time solutions of the time-dependent equations to the choice of initial conditions. For example, it is possible that if the circulation at the inflow boundary were to be slowly increased in time, starting at time $t = 0$ with the case of no swirl, then reversed flow would not develop, and the solution point at $V = 2.3692$ on the lower path could be computed. Another goal of future work should be the determination of the lower bound on vortex strength for which breakdown bubbles are sustained in the flow in the large-time limit. Such a bound might be related to the limit point at $V = 2.2748$, shown in Figure (3.39).

3.7 Calculation Statistics

Linear systems of equations resulting from each Newton iteration were solved using Gaussian elimination with partial pivoting. Advantage of the banded structure of the Jacobian matrix was taken to minimize the usage of computer resources. The bandwidth of each Jacobian matrix was $6J+3$. The column-by-column, node-ordering scheme, $k = (i-1)J + j$, was chosen over row-by-row node ordering to reduce the bandwidth, anticipating that in most cases it would be necessary to have I greater than J.

Each Newton iteration required approximately $18J^2I$ words of computer memory and involved approximately $108J^3I$ floating-point operations. For $J = 40$ and $I = 105$, Newton iterations were completed in 5 cpu seconds at a computation rate

of 90 million floating-point operations per cpu second and required approximately 3.5 million words of main computer memory.

Chapter 4

Behavior of Flow up to Transition

In Chapter 3, solutions of the Navier-Stokes equations for the evolution of trailing vortices are presented. It was found that trailing vortices with sufficiently large circulation clearly experience a transition between two states. The flow state upstream of the transition point is characterized by slow growth of vortex core radius and slow decay of centerline axial velocity. Results presented in this chapter indicate that the flow in this region is well represented by the quasi-cylindrical (QC) equations and that transition-point position is linearly dependent on Reynolds number, with vortex strength constant. Solutions of the QC equations are computed, using the algorithm outlined in Appendix E, and are compared with solutions of the Navier-Stokes equations presented in Chapter 3. For a particular choice of Reynolds number and inflow conditions, it is found that failure of the QC equations is a necessary and sufficient condition for transition. Solutions of the QC equations were computed on a Zenith Z-248 microcomputer.

4.1 Description of the Behavior of Quasi-Cylindrical Flows

In the absence of vortex bursting, the behavior of a trailing vortex at high Reynolds number is well approximated by the QC equations. These equations are analogous to the boundary-layer equations governing the flow over a solid surface, and are derived (see Appendix A) assuming that axial gradients of flow quantities are small compared to the corresponding radial gradients.

In this section, discussion will be based on computed solutions of the QC equa-

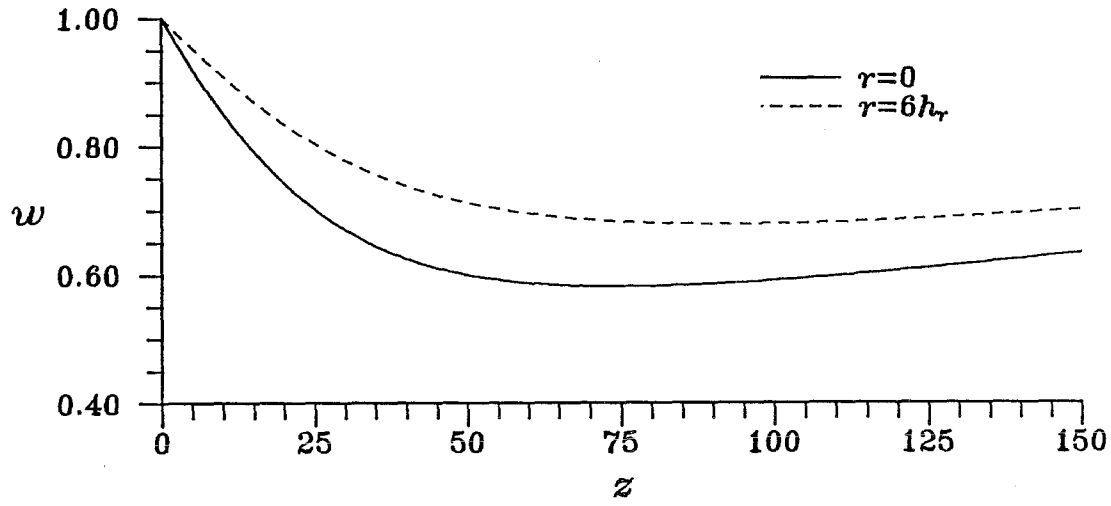

Figure 4.1 Centerline and off-centerline profiles of axial velocity for Re = 1000 and $V = 0.73$

tions for two values of vortex strength with Re = 1000 and $a = 0$. The first solution was obtained for $V = 0.73$, and centerline and off-centerline profiles of axial velocity for this case are shown in Figure (4.1). The grid parameters I, Z, J and R were specified to be 301, 150, 27 and 2, respectively. The second solution was obtained for a slightly larger vortex strength, $V = 0.80$, and centerline and off-centerline profiles of axial velocity for this case are shown in Figure (4.2). Grid parameters I, Z, J and R were specified to be 101, 50, 27 and 2, respectively. Note that in both Figure (4.1) and (4.2), the off-centerline profile is measured at a radial position of $r = 6h_r$, where h_r is the node spacing in the radial coordinate direction, which is approximately in the middle of the vortex core.

The two cases are distinguished by the failure of the QC equations at $z \approx 14$, when $V = 0.80$. Failure of the QC equations is discussed in more detail in Appendix D. Large error introduced in the jump across the singularity causes the computed flow downstream of the singularity to be invalid. Upstream of the singularity, the axial velocity fields of the two cases are qualitatively identical, although axial velocity decays at a faster rate, with respect to axial position, when $V = 0.80$ than when $V = 0.73$.

The decay of centerline axial velocity is a result of the coupling between the

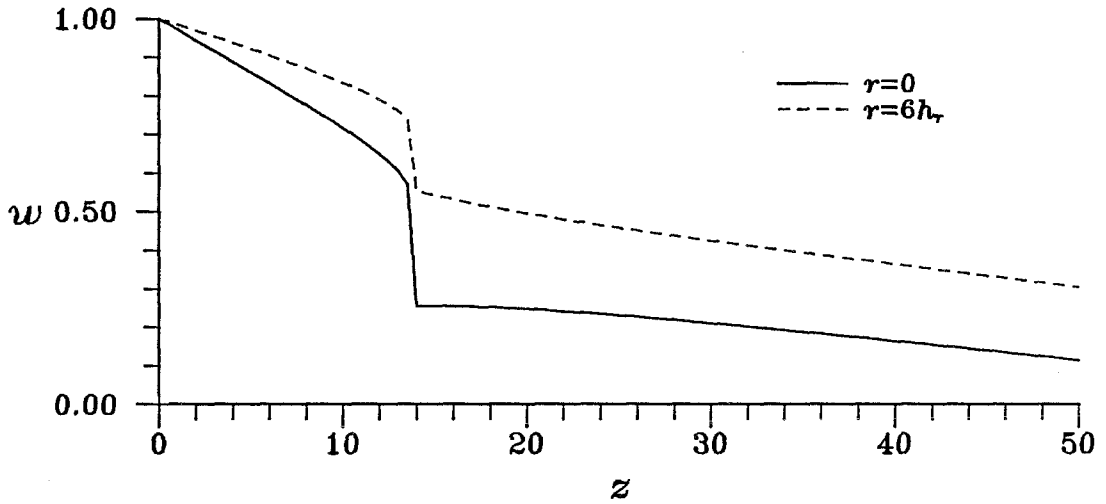

Figure 4.2 Centerline and off-centerline profiles of axial velocity for Re = 1000 and $V = 0.80$

circulation field and the pressure field as previously discussed by Hall (1972), and Grabowski and Berger (1976). This coupling is clearly evident in the quasi-cylindrical form of the radial momentum equation,

$$\frac{\partial p}{\partial r} = \frac{\Gamma^2}{r^3}, \tag{4.1}$$

which is an expression of balance between the centrifugal acceleration of a fluid particle and the radial pressure gradient. If circulation is specified as a function of radial position at a particular station, then (4.1) may be integrated to compute the pressure profile at the same station, assuming that p vanishes in the far-field. Since circulation monotonically increases with radial position at stations between the inflow boundary and the failure point, pressure is everywhere negative within the vortex and at each station is minimum at $r = 0$. On the symmetry axis the pressure is given by

$$p(z,0) = -\int_0^\infty \frac{\Gamma^2}{r^3} dr, \tag{4.2}$$

and the gradient of the pressure along the symmetry axis is given by

$$\frac{\partial p}{\partial z}(z,0) = -\int_0^\infty \frac{2\Gamma}{r^3}\frac{\partial \Gamma}{\partial z} dr. \tag{4.3}$$

Diffusion of the axial component of vorticity, $\frac{1}{r}\frac{\partial \Gamma}{\partial r}$, causes circulation to decrease with axial position along lines of constant r as vorticity diffuses away from

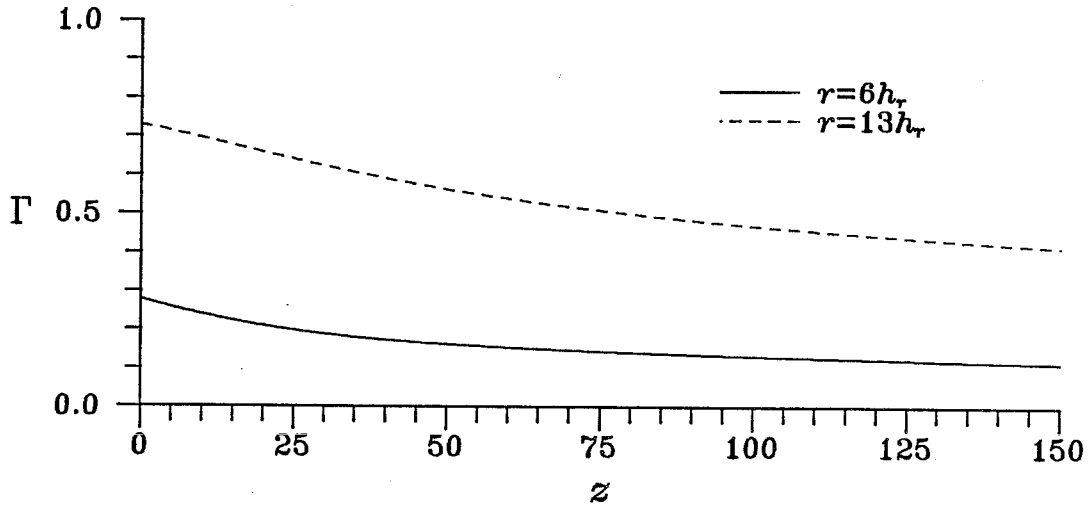

Figure 4.3 Off-centerline profiles of circulation for Re = 1000 and $V = 0.73$

the symmetry axis and into the surrounding irrotational flow. Thus, the integral in (4.3) is negative and the axial gradient of centerline pressure is positive or "adverse." Off-centerline profiles of circulation for $V = .73$ and $V = .80$ are shown in Figures (4.3) and (4.4). In each figure, profiles are shown along lines of $r = 6h_r$ and $r = 13h_r$, corresponding to points approximately in the middle of the vortex core and at the boundary of the core, respectively. Figures (4.3) and (4.4) verify that circulation decreases with axial position and also show that the axial gradient increases (becomes less negative) with axial position. The combined effect is a decrease in the magnitude of the integral in (4.3) and a corresponding decrease in the axial gradient of centerline pressure.

The axial momentum equation, evaluated on the symmetry axis, is

$$w\frac{\partial w}{\partial z} + \frac{\partial p}{\partial z} = \frac{1}{\mathrm{Re}}\frac{\partial^2 w}{\partial r^2} \quad (r = 0). \tag{4.4}$$

At the inflow boundary $\frac{\partial^2 w}{\partial r^2} = 0$, assuming $a = 0$, and the adverse pressure gradient, which develops through the process described above, causes the centerline axial velocity to decrease with axial position. Therefore, the flow downstream of the inflow boundary can be characterized as a wakelike flow with a deficit in axial velocity in the vortex core. A negative gradient of axial velocity in the core must be accompanied by a positive mass flux across surfaces of constant r in the core

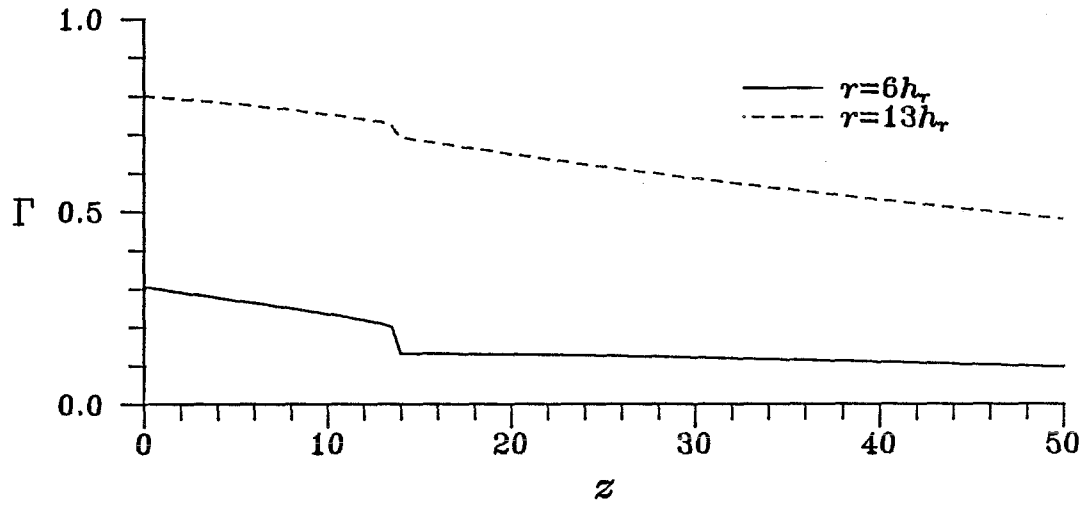

Figure 4.4 Off-centerline profiles of circulation for Re = 1000 and $V = 0.80$

through mass conservation. Thus, for some distance downstream of the inflow boundary, the radial velocity is positive within the vortex core.

Another effect of positive radial velocity is the convection of vorticity away from the symmetry axis, an effect which further contributes to the decay of circulation and to the development of an adverse pressure gradient in the vortex core. This contribution represents part of a weak feedback loop, since an increase in the axial pressure gradient leads to an increase of the radial velocity in the core. Shear forces, however, prevent a rapid growth of the vortex and arise in response to the axial velocity deficit in the core. These forces, expressed analytically as the viscous term of the axial momentum equation, act to increase the axial velocity in the core to the freestream velocity in the same way that viscous stresses correct the axial velocity deficit in a nonswirling wake (Grabowski and Berger (1976)).

Referring again to (4.4), the viscous term on the right-hand side of the equation will be positive in the neighborhood of the symmetry axis because of the deficit in axial velocity. As the axial gradient in centerline pressure decreases because of decay of both circulation and the axial gradient of circulation in the vortex, a point will be reached, provided that the flow remains supercritical, at which the viscous term balances the pressure gradient. At this point the axial gradient in centerline axial velocity vanishes. Downstream of this point, axial velocity on the symmetry

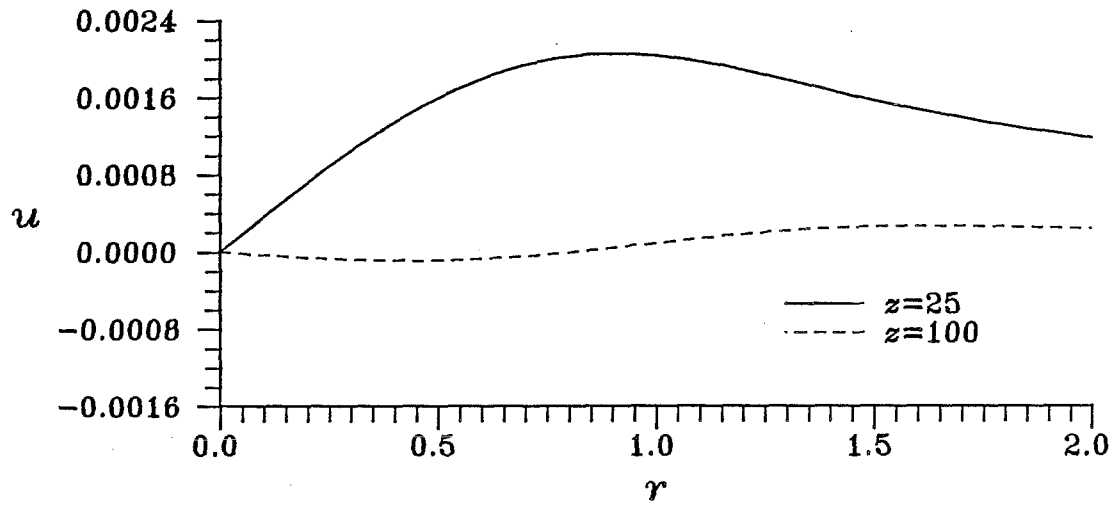

Figure 4.5 Profiles of radial velocity at $z = 25$ and $z = 100$ for Re $= 1000$ and $V = 0.73$

axis begins to increase and by continuity, radial velocity in the neighborhood of the symmetry axis becomes negative. Furthermore, with increased axial position, the viscous term continues to dominate the adverse pressure gradient so that axial velocity in the core asymptotically approaches the freestream velocity as evident in Figure (4.1).

Profiles of radial velocity at two different axial stations, $z = 25$ and $z = 100$, are shown in Figure (4.5) for the case $V = 0.73$. When $z = 25$, the radial velocity is positive throughout the vortex, as would be expected, since at this station axial velocity in the core is decreasing with axial position. The second station, $z = 100$, is downstream of the point at which a global minimum in axial velocity is achieved on the symmetry axis and at this station, radial velocity is negative throughout much of the core.

The caveat noted above warns of the singularity present in the QC equations. As demonstrated in Appendix D, radial velocity diverges as a critical station is approached. Thus, if a critical station is encountered before viscous stress dominates the adverse pressure gradient in the core, the QC equations fail, and the subsequent behavior of the vortex cannot be computed. This is the situation depicted in Figure (4.2). However, upstream of the failure point, the behavior of the flow

is qualitatively identical to the behavior of swirling flows with smaller circulations in which failure does not occur.

4.2 Comparison of Solutions of Navier-Stokes and QC Equations

In this section, solutions of the QC equations are presented and compared with solutions of the Navier-Stokes equations. Comparison verifies that the QC equations accurately model trailing vortex-evolution upstream of transition, and provides an additional validation of the procedure by which the Navier-Stokes equations are solved.

Integration of the QC equations in the direction of increasing z, the timelike coordinate, fails when the flow becomes critical, i.e., when the flow can locally support waves of infinitesimal amplitude (Hall (1967, 1972)). Upstream of this failure, the flow is supercritical, and the flow cannot support such waves. In a practical sense, the failure of the integration procedure is a result of the rapid appearance of large radial velocities in the vicinity of the critical station, as shown in Appendix D. The axial position at which the integration procedure fails will be denoted by z_{cr} (the critical station), and is distinct from the axial position at which transition occurs, z_{tp}. In all cases examined, z_{cr} is greater than z_{tp} when parameters common to the quasi-cylindrical and Navier-Stokes models (i.e., Re, V and a) are the same, reflecting the observation (Section (3.5)) that transition occurs in supercritical flow.

Within the framework of the quasi-cylindrical model, the flow downstream of z_{cr} can be computed. However, in this portion of $\Re$, the solutions appear to lack any physical significance, based on comparison with solutions obtained with the Navier-Stokes equations. Trigub (1985) has noted that flows on either side of the critical station cannot be analytically connected, while flows across the singularity appearing in the two-dimensional, boundary-layer equations may be analytically connected.

Finally, z_{cr} is found to vary linearly with Reynolds number as predicted by the

Run	Re	V	a	I	J	Z	R	z_{cr}
TV403	2000.	0.7677	0.0	105	27	80	2	-
TV403a	2000.	0.7677	0.0	209	27	80	2	-
TV404	2000.	0.7791	0.0	105	27	80	2	46.9
TV404a	2000.	0.7791	0.0	209	27	80	2	46.5
TV405	2000.	0.7823	0.0	105	27	80	2	42.3
TV405a	2000.	0.7823	0.0	209	27	80	2	41.9
TV406	2000.	0.7846	0.0	105	27	80	2	39.2
TV406a	2000.	0.7846	0.0	209	27	80	2	39.2
TV407	1000.	0.7846	0.0	105	27	80	2	20.0
TV408	1500.	0.7846	0.0	105	27	80	2	30.0
TV409	2767.	0.7846	0.0	105	27	80	2	53.8
TV410	3239.	0.7846	0.0	105	27	80	2	63.1
TV403b	2000.	0.7690	0.0	209	27	160	2	-
TV403d	2000.	0.7710	0.0	209	27	160	2	-
TV403f	2000.	0.7730	0.0	209	27	160	2	-
TV403g	2000.	0.7741	0.0	105	27	80	2	-
TV403h	2000.	0.7749	0.0	105	27	80	2	-
TV403i	2000.	0.7759	0.0	105	27	80	2	53.8
TV403j	2000.	0.7768	0.0	105	27	80	2	51.2
TV403k	2000.	0.7778	0.0	105	27	80	2	48.8

Table 4.1 Solutions of QC equations and computed values of z_{cr}

similarity analysis outlined in Appendix A. In Section (4.4), the same relationship is found to hold true between transition position, z_{tp}, and Re. Table (4.1) contains a summary of those computed solutions presented in this section and Section (4.3), including parameter values and observed positions of integration failure.

4.2.1 Comparisons for Varying V

Solutions of the QC equations are compared with solutions of the Navier-Stokes equations for V ranging between 0.7677 and 0.7846 with Re = 2000. Comparisons are made with cases NS403, NS404, NS405 and NS406 (see Table (3.3)). Solutions of the QC equations and the Navier-Stokes equations are obtained, using equivalent grids. Solutions of the QC equations are also obtained using a mesh with I doubled over that used in cases NS403-6. Plots of centerline axial velocity versus axial position are shown in Figure (4.6) for four values of vortex strength: 0.7677

(TV403), 0.7791 (TV404), 0.7823 (TV405) and 0.7846 (TV406). The profiles of centerline axial velocity corresponding to cases NS403 and TV403 are nearly identical. For this choice of vortex strength, 0.7677, transition is not apparent in the solution of the Navier-Stokes equations, nor is failure of the QC equations observed. At the outflow boundary, $Z = 80$, the centerline axial velocities differ by a mere 0.24%. Decreasing the axial-node spacing had no effect on the solution of the QC equations. Both transition and integration failure are evident when V is increased to 0.7791. Upstream of transition, all profiles of centerline axial velocity are in excellent agreement. In this region, centerline axial velocity computed using the QC equations is slightly smaller in magnitude than predicted by the Navier-Stokes equations. The difference vanishes as the upstream boundary is approached and grows slowly as the transition point is approached. Failure of the QC equations occurs at $z = 46.9$, several core radii downstream of transition. The failure is marked by a sudden drop in centerline axial velocity.

The fine-grid solution of the QC equations for $V = 0.7791$, TV704a, is not noticeably different from the coarse-grid solution, TV704, upstream of $z = 46.5$, the point at which the QC equations fail in case TV704a. Failure in case TV704 occurs at $z = 46.9$, or one grid point beyond the failure point in case TV704a. Downstream of the failure points, the solutions are quite different, however. In case TV704, centerline axial velocity continues to decay smoothly beyond the failure point, while in case TV704a, centerline axial velocity varies unsystematically downstream of the failure point. Neither solution reproduces the wave evident in the profile of centerline axial velocity computed using the Navier-Stokes equations.

The failure points of cases TV704 and TV704a are located approximately midway between the positions of the global minimum and the first local maximum in centerline axial velocity of case NS704. When V is increased to 0.7823, and further to 0.7846, the failure points move downstream, relative to the transition point. For $V = 0.7846$, the failure points of cases TV706 and TV706a are located at about the same position as the first local maximum in centerline axial velocity of case

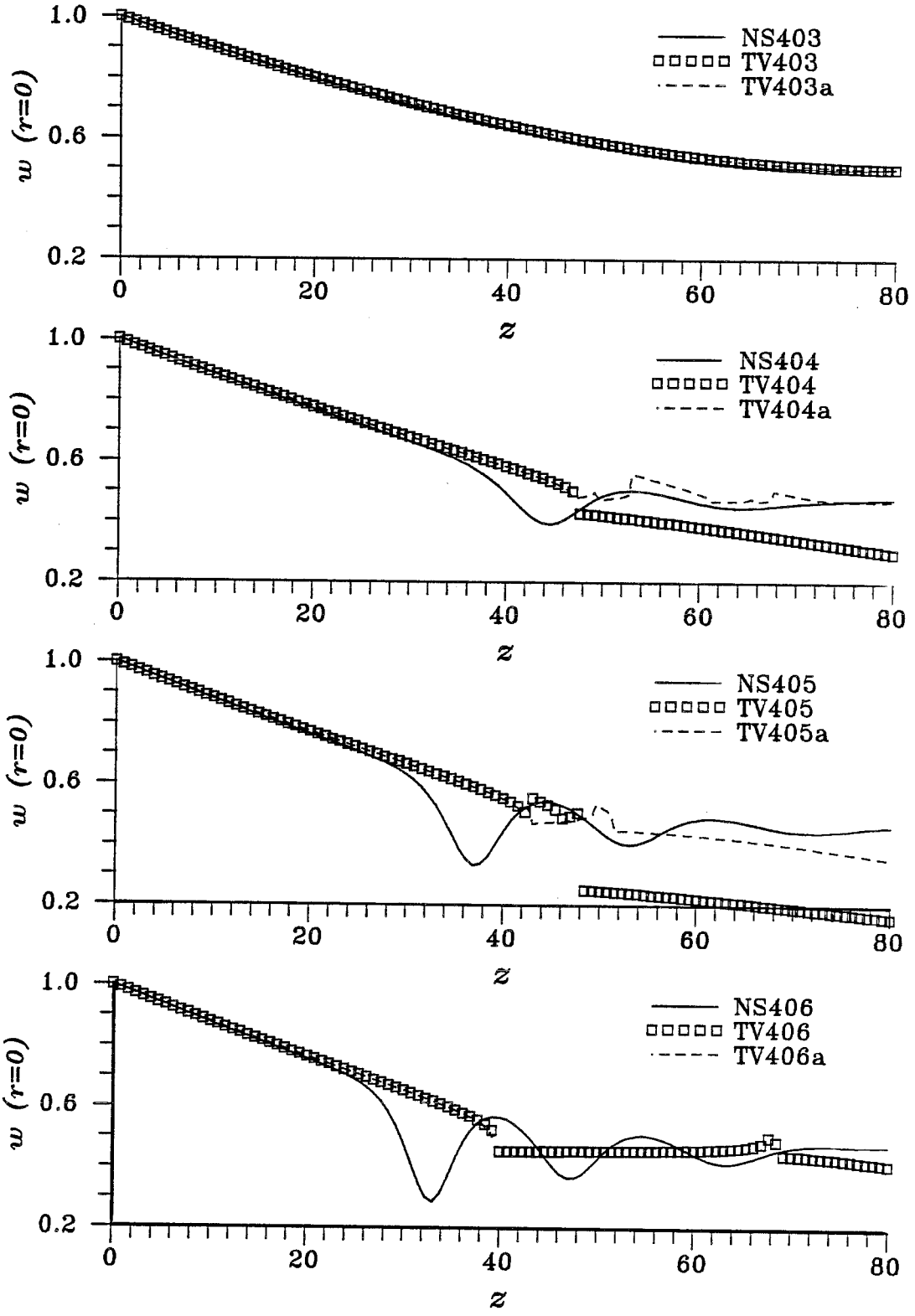

Figure 4.6 Comparison of profiles of centerline axial velocity computed using QC equations and Navier-Stokes equations for varying V

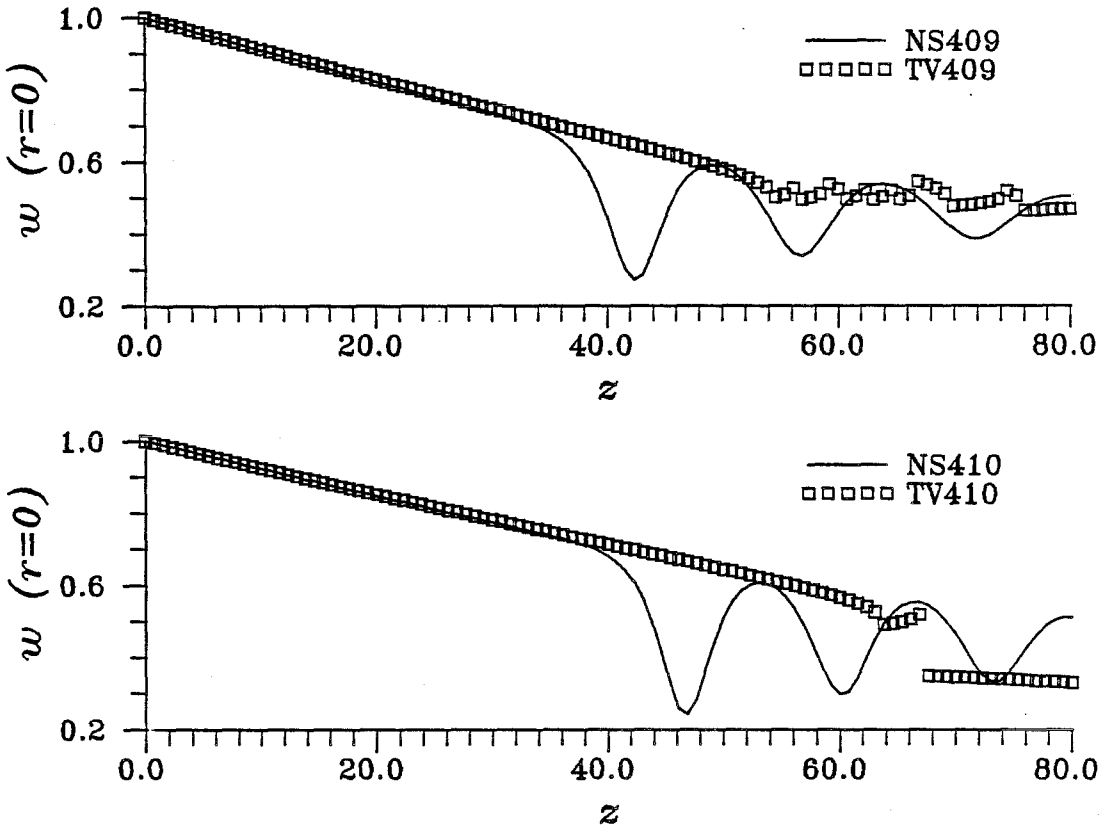

Figure 4.7 Comparison of centerline axial velocity profiles computed using QC equations and Navier-Stokes equations for varying Re

NS706. Thus, as V increases, or equivalently, as wave amplitude increases, the wave predicted by the Navier-Stokes model penetrates farther into supercritical flow.

4.2.2 Comparisons for Varying Re

Solutions of the QC and Navier-Stokes equations are now compared for Re equal to 2000 (TV406, NS406), 2767 (TV409, NS409), and 3239 (TV410, NS410) with $V = 0.7846$. Solutions of the QC equations were obtained only with $I = 105$, the same value of I used in cases NS406-10, since it was found in Section (4.2.1) that increasing I to 209 did not have a noticeable effect on solutions of the QC equations upstream of integration failure. Plots of centerline axial velocity versus axial position are compared in Figure (4.7). In each of the three plots shown

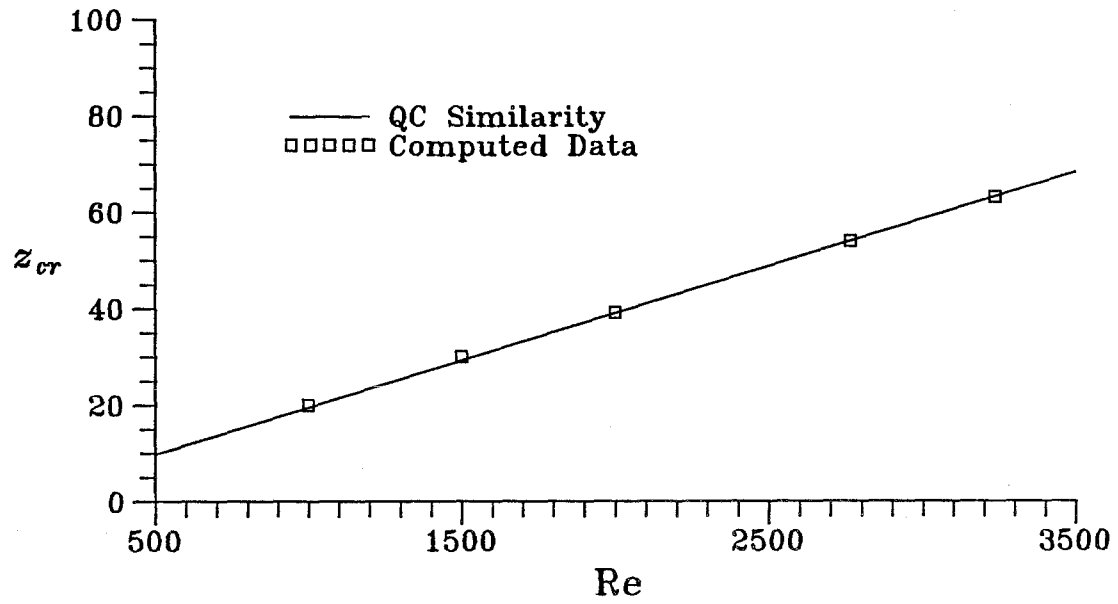

Figure 4.8 z_{cr} versus Reynolds number for cases TV406-10

in Figure (4.7), the point at which the QC equations fail is located downstream of transition. The distance between the failure point and the transition point increases with increased Reynolds number. This observation can be attributed to the linear relationships between transition-point position and critical-station position and Reynolds number, deduced by the similarity analysis outline in Appendix A. Equation (A.44) predicts that

$$z_{cr1} = z_{cr2}\frac{\mathrm{Re}_1}{\mathrm{Re}_2} \tag{4.5}$$

$$z_{tp_1} = z_{tp_2}\frac{\mathrm{Re}_1}{\mathrm{Re}_2}. \tag{4.6}$$

Equation (4.5) is verified in Figure (4.8), in which z_{cr} is plotted versus Reynolds number for Re ranging between 1000 and 4000. Data points are obtained from Table (4.1) for cases TV406-10. A line given by the equation

$$z_{cr} = \mathrm{Re}\left(\frac{z_{cr}}{\mathrm{Re}}\right)_{\mathrm{Re}=3239}, \tag{4.7}$$

on which the data point corresponding to case TV410 lies, is also plotted in Figure (4.8). The data points corresponding to cases TV406-9 are accurately predicted

by this line, as should be expected of a valid procedure for the integration of the QC equations. The linear relationship between transition point position and Reynolds number is also shown to hold in Figure (4.13). Since z_{tp} and z_{cr} are related to Re by the same linear relationship, the difference between these positions must also be linearly related to Re. Thus, for example, if Re doubles, the distance between the two points doubles. As it was found in Chapter 3 that flow wavelength in the vicinity of the transition point is nearly independent of Reynolds number, the number of wave periods occurring between the transition point and the critical point will also increase as Re increases.

4.3 Relationship Between Transition and Integration Failure

The onset of transition and the ensuing development of wavelike flow evident in solutions of the Navier-Stokes are intimately linked to the failure of the integration of the QC equations. In Section (4.2), several solutions of the Navier-Stokes equations were presented in which large-amplitude, spatial oscillations of centerline axial velocity were observed. When compared with these solutions, solutions of the QC equations were found to contain abrupt changes in centerline axial velocity at points downstream of transition. Failure of the QC equations was observed in every case except case TV403, and for the parameter values chosen in this case, transition did not occur in the corresponding solution of the Navier-Stokes equations, NS403.

The purpose of this section is to investigate the failure of the QC equations when transition first occurs in solutions of the Navier-Stokes equations as V is varied. It is found that the QC equations fail at the same value of V for which transition is first evident. Thus, failure of the QC equations serves as a useful, necessary, and sufficient condition for the onset of transition in solutions of the Navier-Stokes equations. For more complicated problems than those examined in this work (e.g., asymmteric flows), it may be sufficient to obtain solutions of the parabolized Navier-Stokes equations instead of the full Navier-Stokes equations, if

Run	Re	V	a	I	J	Z	R	Matching QC Case
NS1252	2000.	0.7741	0.0	105	27	80	2	TV403g
NS1253	2000.	0.7749	0.0	105	27	80	2	TV403h
NS1254	2000.	0.7759	0.0	105	27	80	2	TV403i

Table 4.2 Solutions of Navier-Stokes equations examined in Section (4.3)

all that must be determined is whether transition does or does not occur and if so, a rough estimate of z_{tp}.

Additional solutions of the Navier-Stokes equations were computed over a very small range of vortex strengths, starting with $V = 0.7677$ (the vortex strength chosen in case NS403), using continuation in V with Re = 2000. Parameter values for these cases are tabulated in Table (4.2).

Cases TV403g-i and cases NS1252-4 are compared in Figure (4.9). It was found by experimentation that solutions of the QC equations were independent of increase of I beyond 105, and thus $I = 105$ was chosen for cases TV403g-i. Cases NS1252 and TV403g ($V = 0.7741$) are compared first in Figure (4.9). Centerline axial velocity for case NS1252 is minimum at $z = 61.5$. Downstream of this point velocity monotonically increases with axial position. A very similar situation is obtained in case TV403g. The profiles are in excellent agreement upstream of $z \approx 20$ and slowly diverge downstream of this point. In the neighborhood of $z = 62$, the profile for case TV403g changes slope and is nearly flat for $z > 62$. Although difficult to observe in the figure, the profile has a small, negative slope in the "flat" region and has a minimum downstream of the outflow boundary, found by increasing the domain length with axial-node spacing, h_z, held constant. Downstream of the minimum, centerline axial velocity slowly increases.

The change in slope does not appear to be a manifestation of a failure of the QC equations, but instead appears to be part of a limiting process as V is increased from 0.7677. For this value of V, the profile (shown in Figure (4.6)) does not have a "flat" region; centerline axial velocity decreases gradually until a minimum is achieved downstream of $z = 80$, after which velocity gradually increases.

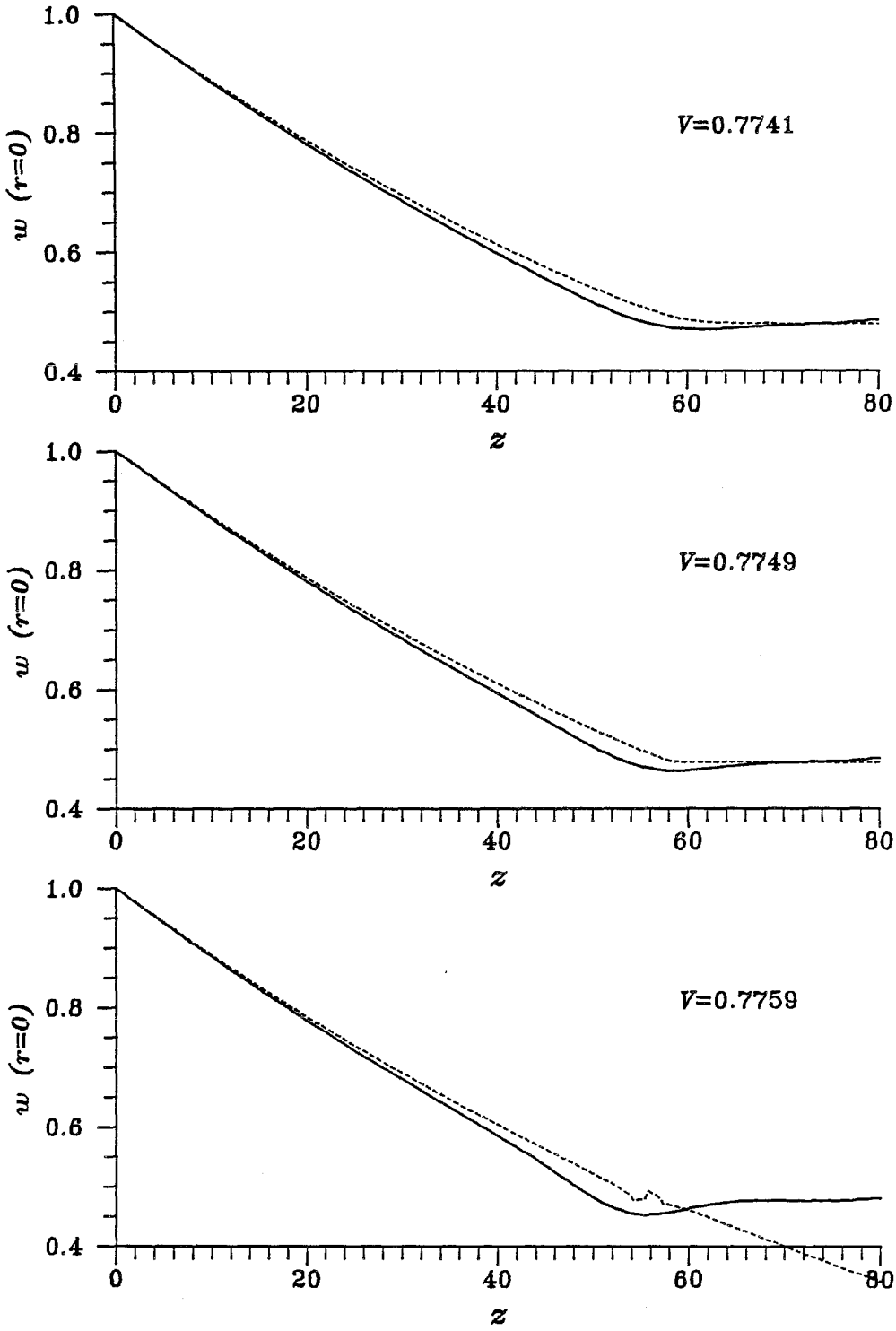

Figure 4.9 Comparison of centerline axial velocity versus axial position for solutions of Navier-Stokes equations (solid line) and QC equations (dashed line)

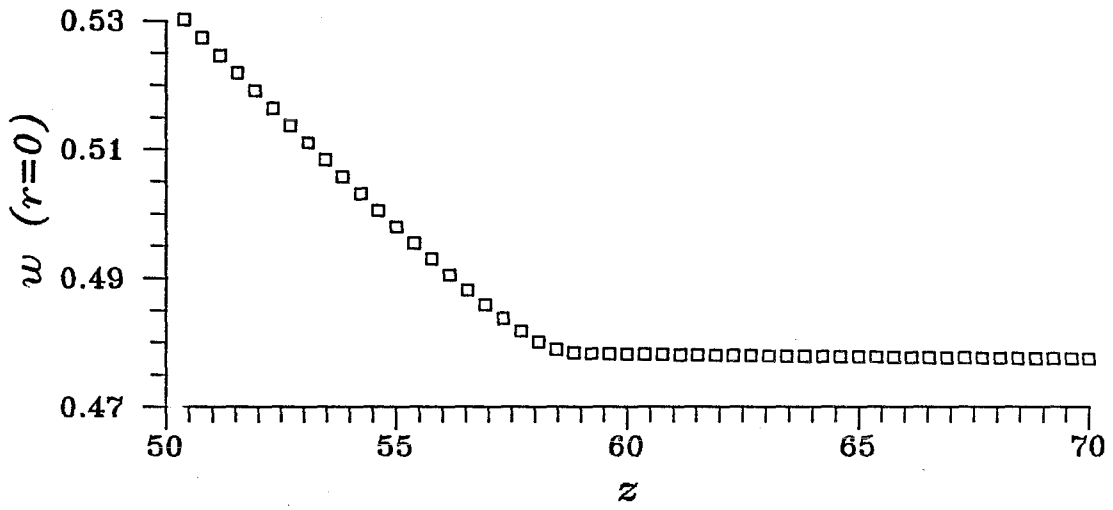

Figure 4.10 Centerline axial velocity versus axial position for case TV403h

When V is increased to 0.7749, case TV403h, the change in slope of the velocity profile occurs over only three or four grid points. An enlarged view of the portion of the profile in the vicinity of the slope change is shown in Figure (4.10) (computed data points are plotted). The profile is nearly flat between $z = 59$ and the outflow boundary. Additional calculations showed that centerline axial velocity begins to increase beyond $z = 80$. The profile of centerline axial velocity for case NS1253 has a minimum at $z = 58.5$, within the range in which the profile corresponding to case TV403g changes slope. Downstream of the minimum, velocity monotonically increases, but in the neighborhood of $z = 73$, an inflection point is nearly formed, resulting in a reduced rate of velocity increase in that neighborhood.

Cases TV403i and NS1254 are compared in the final plot of Figure (4.9). For these cases, $V = 0.7759$. Failure of the QC equations is evident at $z = 54$ and marked by high-frequency changes in centerline axial velocity. Downstream of the failure point, the flow computed with the QC equations is not physically meaningful, and the solution rapidly diverges from the flow computed using the Navier-Stokes equations. The profile of centerline axial velocity corresponding to case NS1254 has a global minimum at $z = 55.5$ and a local minimum around $z = 76$. The second minimum occurs at about the same axial position at which the near-inflection point occurred for $V = 0.7749$. Although the transition point is indis-

tinct in case NS1254, a definite change in profile slope can be observed around $z = 46$. Such a change of slope is not observed when $V = 0.7749$. Failure of the QC equations occurs downstream of the transition point by approximately 10 core radii.

With further increase of vortex strength, the transition point and the global minimum become more pronounced, as documented in Figure (4.6). The QC equations are also observed to fail when $V > 0.7759$. Neither transition nor failure of the QC equations was observed when $V < 0.7759$. Thus, for the particular example examined in this section, in which Re = 2000 and $a = 0$ where specified, failure of the QC equations is a necessary and sufficient condition for the onset of transition.

4.4 Flow Behavior at Transition as a Function of Re

It is found that axial and azimuthal velocity profiles at the transition point are nearly independent of changes in Re when V is fixed and Re is sufficiently large. In these cases, z_{tp} varies linearly with Reynolds number so that the similarity relations, derived in Section (A.6) assuming quasi-cylindrical flow, are satisfied at $z = z_{tp}$. z_{tp} does not appear to be dependent on axial gradients of the axial and azimuthal velocity profiles. Thus, a criterion or set of criteria based on the functional form of the axial and azimuthal velocity profiles should determine whether a flow makes a transition to an oscillatory state.

The flow properties at z_{tp} of those solutions of the Navier-Stokes equations presented in Section (3.3.9) are compared in this section. These solutions were examined since they were obtained for large Re, and as Re increases, transition is more pronounced and the flow upstream of the transition point better approximated by the QC equations. Figure (4.11) shows plots of axial velocity profiles at z_{tp} for three different cases: NS703 (Re = 15705), NS704 (Re = 18095) and NS705 (Re = 20440). Refer to Table (3.3) for a tabulation of z_{tp} for various solutions of the Navier-Stokes equations. The profiles shown in Figure (4.11) are nearly

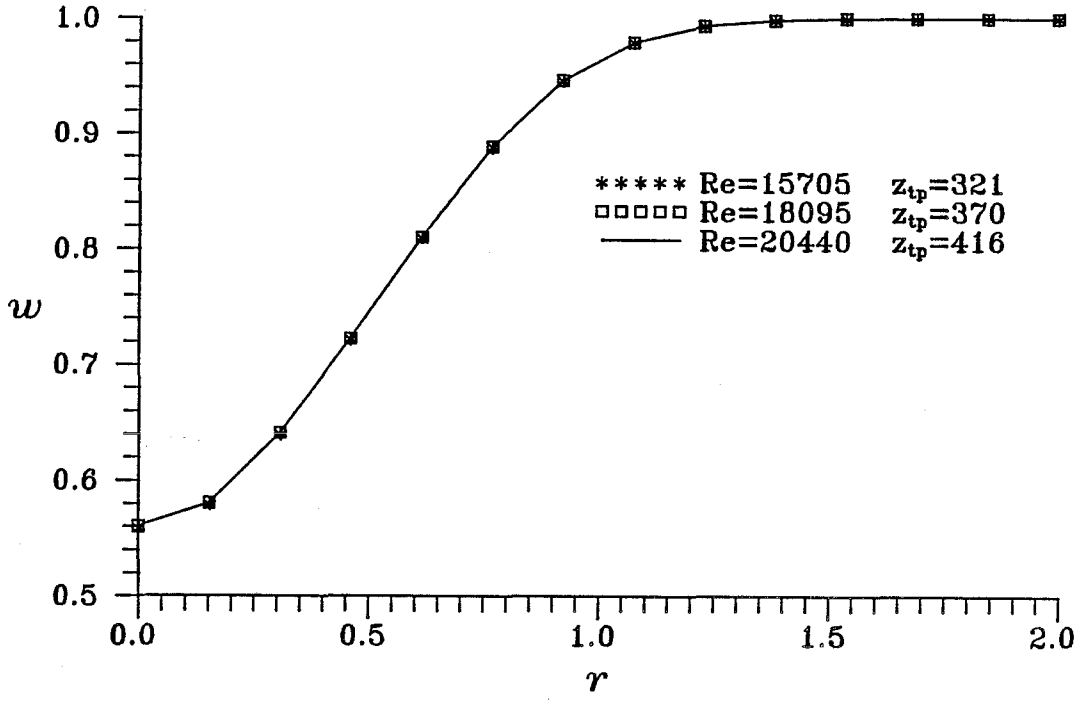

Figure 4.11 Axial velocity profiles at z_{tp}: Re = 15705, 18095 and 20440

identical. The same is also true of azimuthal velocity profiles at z_{tp}, as shown in Figure (4.12).

It was determined in Section (A.6) that for equivalent inflow boundary conditions, solutions of the QC equations (2.13—2.15) satisfy the similarity relationships (A.45—A.47) as Re is varied. If velocity profiles at z_{tp} are to satisy these relations, then for two distinct cases, Re = Re_1 and Re = Re_2, the following conditions should be satisfied:

$$u(r, z_{tp_1}, \mathrm{Re}_1) = \frac{\mathrm{Re}_2}{\mathrm{Re}_1} u(r, z_{tp_2}, \mathrm{Re}_2) \tag{4.8}$$

$$v(r, z_{tp_1}, \mathrm{Re}_1) = v(r, z_{tp_2}, \mathrm{Re}_2) \tag{4.9}$$

$$w(r, z_{tp_1}, \mathrm{Re}_1) = w(r, z_{tp_2}, \mathrm{Re}_2) \tag{4.10}$$

$$z_{tp_1} \mathrm{Re}_1^{-1} = z_{tp_2} \mathrm{Re}_2^{-1}. \tag{4.11}$$

Conditions (4.9) and (4.10) were observed to be true for the axial and azimuthal velocity profiles shown in Figures (4.11) and (4.12), respectively. z_{tp} is found to satisfy (4.11), rewritten as

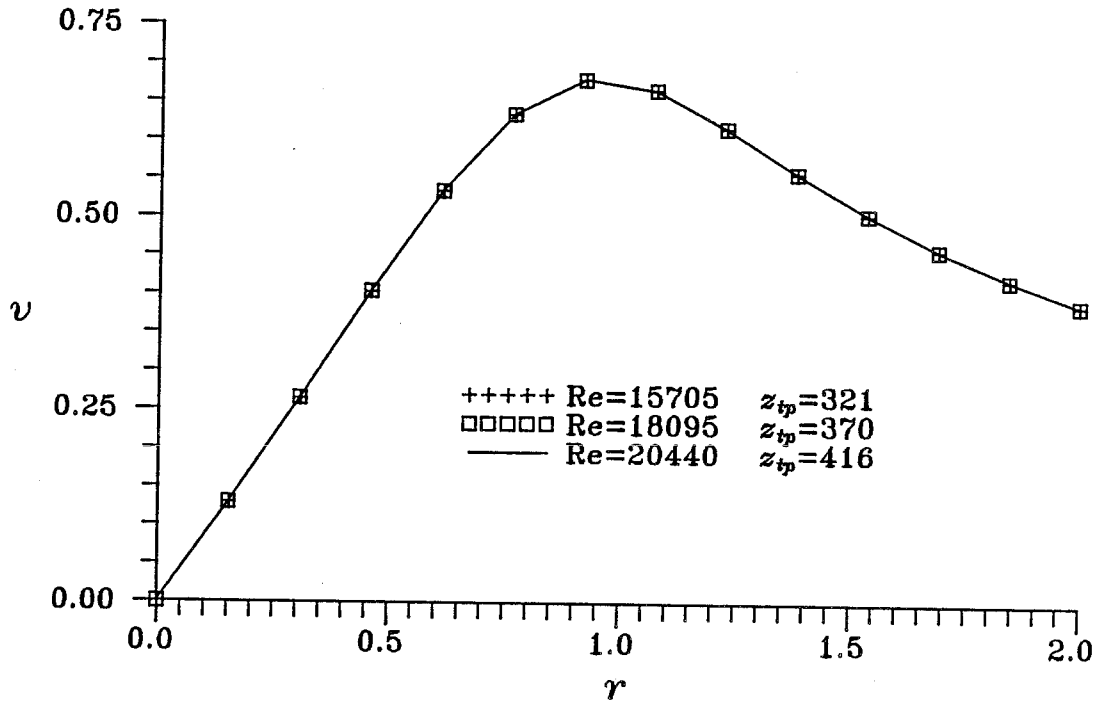

Figure 4.12 Azimuthal velocity profiles at z_{tp}: Re = 15705, 18095 and 20440

$$\frac{z_{tp_2}}{z_{tp_1}} = \frac{\mathrm{Re}_2}{\mathrm{Re}_1}. \tag{4.12}$$

Figure (4.13) shows a plot of z_{tp} versus Reynolds number for the three cases compared in Figures (4.11) and (4.12) and for three additional cases: NS700 (Re = 2104), NS701 (Re = 7063) and NS702 (Re = 13143). Also shown is a line passing through the point corresponding to case NS705, given by the equation

$$z_{tp} = \mathrm{Re}\left(\frac{z_{tp}}{\mathrm{Re}}\right)_{\mathrm{Re}=20440}. \tag{4.13}$$

Figure (4.13) verifies that computed values of z_{tp} are well predicted by (4.13).

Equation (4.8), however, is found to be invalid. Profiles of radial velocity are plotted in Figure (4.14) for four cases: NS702, NS703, NS704 and NS705. In each of the plots, radial velocity is multiplied by the factor $\frac{\mathrm{Re}}{20440}$. Equation (4.8) is satisfied if all four scaled profiles coincide. Instead, it is found at z_{tp} that radial velocity, after scaling, generally increases as Reynolds number increases. This effect is due to the way in which z_{tp} is defined. At the transition point, the flow is in an intermediate state between a quasi-cylindrical flow and an oscillatory flow,

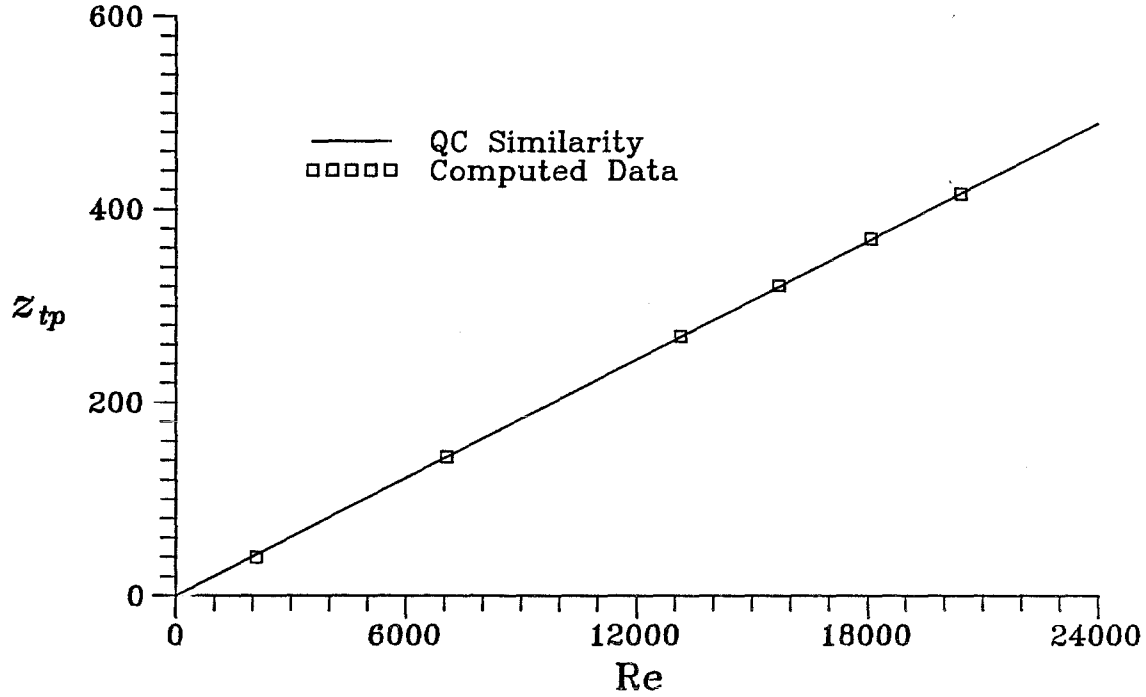

Figure 4.13 z_{tp} versus Reynolds number for cases NS700-5

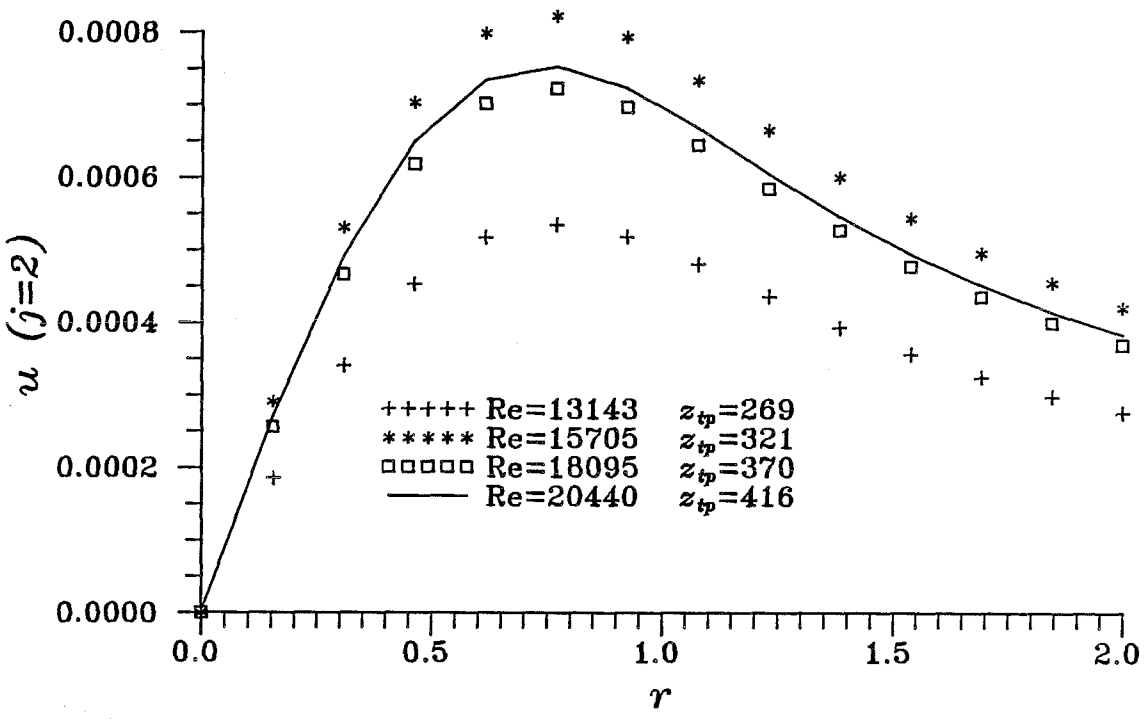

Figure 4.14 Radial velocity profiles at z_{tp}: Re = 13142, 15705, 18095 and 20440

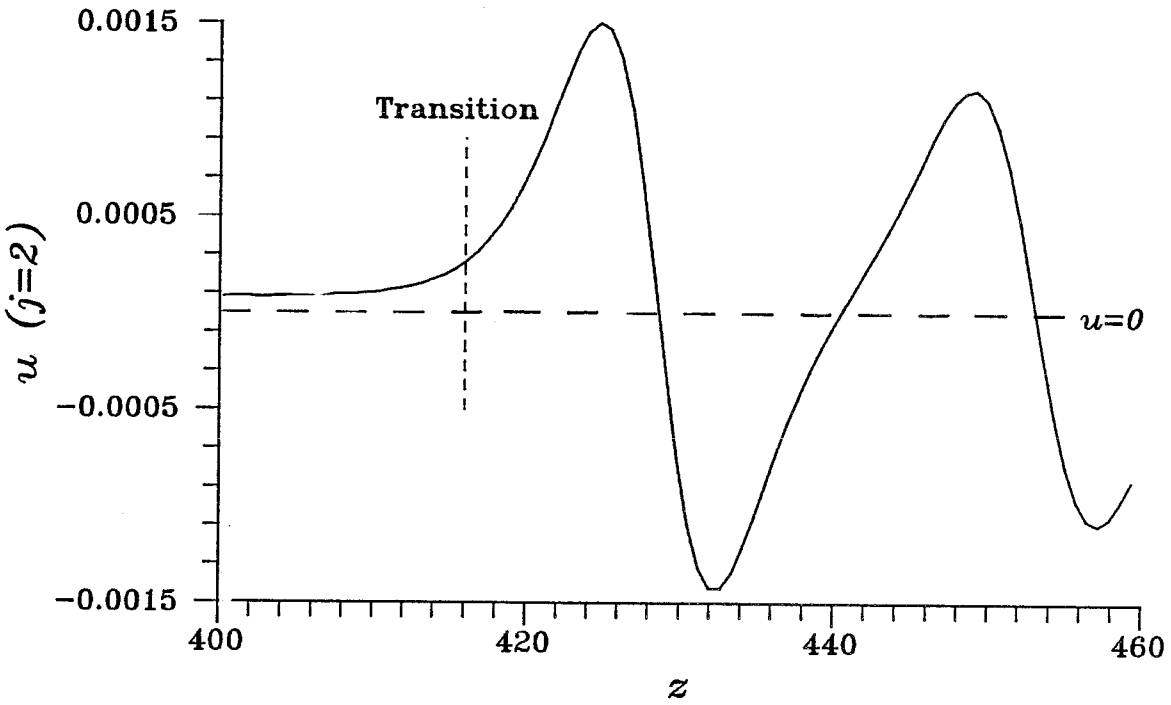

Figure 4.15 Radial velocity ($r = h_r$) versus z for Re = 20440

and in this intermediate state (4.8) is violated, while (4.9) and (4.10) are well approximated. To illustrate this point, radial velocity, along the line $r = h_r$, is plotted versus z in Figure (4.15) and axial velocity, along the line $r = 0$, is plotted versus z in Figure (4.16). In Figure (4.15), it is apparent that there is a relatively large difference between the magnitude of u at $z = z_{tp}$ and at an axial position, a few core radii less than z_{tp}. Thus, one would not expect the radial velocity profiles at z_{tp} to be governed by a similarity condition derived from the QC equations, since the radial velocity field deviates markedly from a quasi-cylindrical state at the transition point. In contrast, there is a relatively small deviation in the trend of centerline axial velocity as the transition point is approached from the inflow boundary (Figure (4.16)). Therefore, it is reasonable to expect the axial velocity profiles at z_{tp} to be governed by (4.10), as indeed they are.

At z_{tp}, radial velocity, after scaling, increases with increasing Re since the magnitude of spatial oscillations downstream of transition increases with Reynolds number. Through continuity, radial velocity at z_{tp} increases as the magnitude of

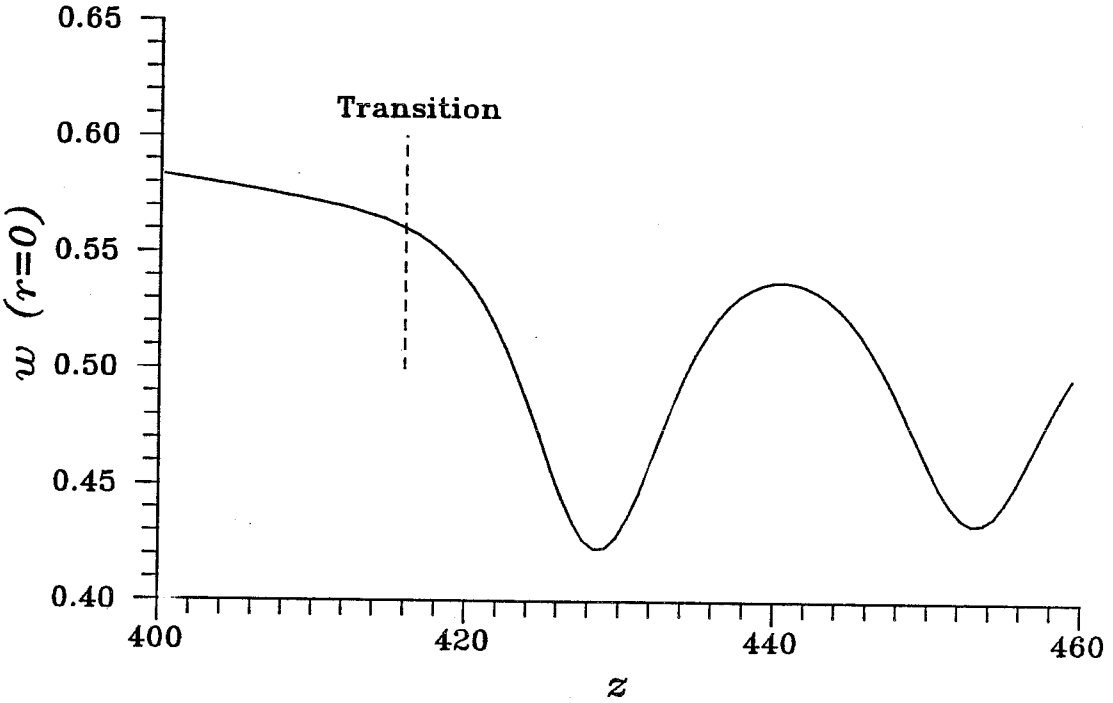

Figure 4.16 Centerline axial velocity versus z for Re = 20440

Run	Re	Profile Position (z)	Multiplicative Factor
NS703	15705.	119.5	0.7683
NS704	18095.	137.7	0.8853
NS705	20440.	155.5	1.0000

Table 4.3 Multiplicative factors and axial positions of profiles in Figure (4.17)

the axial gradient of w increases.

Radial velocity profiles do satisfy (A.45) well upstream of the transition point, giving further evidence that the flow is well approximated by the QC equations in this region. Radial velocity, after scaling, is plotted against r in Figure (4.17) for three different values of Re. Multiplicative factors and axial positions of each profile, given by (4.8) and (4.11), respectively, are tabulated in Table (4.3). The results shown in Figure (4.17) indicate that (A.45) is an excellent approximation.

The results presented in this section lead to two main conclusions. First, the axial and azimuthal velocity profiles at the transition point are nearly independent of Reynolds number, suggesting that there is a criterion or set of criteria, based on the functional form of $v(r)$ and $w(r)$, which determine where transition

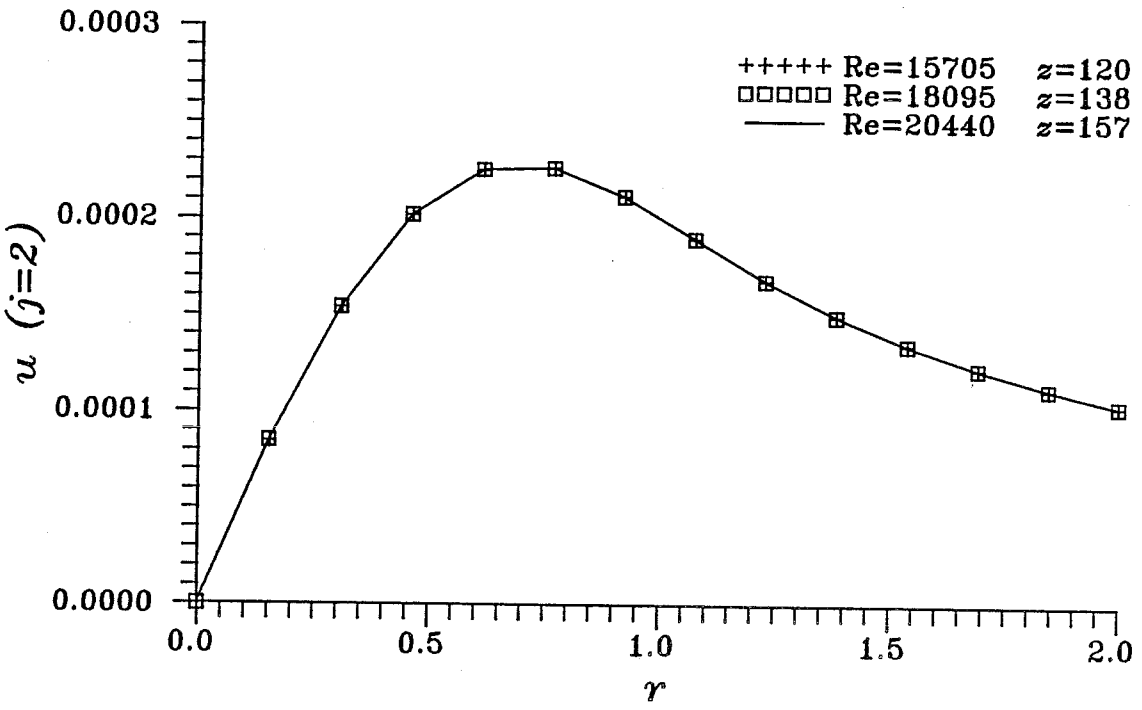

Figure 4.17 Radial velocity profiles: Re = 15705, 18095 and 20440

occurs. Second, z_{tp} is related to Reynolds number in a simple way predicted by the assumption of quasi-cylindrical flow at the transition point.

Chapter 5

Conclusions

This chapter provides a summary and discussion of the results presented in Chapters 3 and 4 and, more importantly, examines these results in the context of theories of vortex breakdown proposed by Benjamin (1967); Brown and Lopez (1988); and Hall (1967). Section (5.1) evaluates the algorithm used to compute solutions of the Navier-Stokes equations and suggests improvements to the algorithm that would be considered in follow-up work to this investigation. The phenomenon of transition is described in Sections (5.2)—(5.4), with reference to experimental observations, and then in Section (5.5), discussed in light of theoretical work by Benjamin (1967). Findings of nonunique solutions to the steady-state Navier-Stokes equations are reviewed in Section (5.6), and the existence of nonunique solutions is used to explain recent results obtained by Brown and Lopez (1988) in Section (5.7). Finally, comparisons between solutions of the Navier-Stokes and QC equations are discussed in Section (5.8). The applicability of the "boundary-layer-analogy" theory of vortex breakdown is also discussed in this section.

5.1 Navier-Stokes Code

The algorithm employed in this work to solve the Navier-Stokes equations, Euler-Newton pseudo-arclength continuation, proved to be an efficient and robust scheme. Solution points were computed quickly and over a wide range of parameter values. Furthermore, nonunique solutions were obtained that would not normally

be found using standard numerical algorithms.

Efficiency was obtained, however, at the expense of versatility. Use of Newton's method and Gaussian elimination is practical only for simple two-dimensional problems such as the model studied in this work. For three-dimensional or complex, two-dimensional problems, Gaussian elimination must be replaced by an iterative method, suitable for sparse matrices.

The primary factor limiting the use of Gaussian elimination is the storage requirement. For problems on square computational domains, with an equivalent number of nodes, L, in each coordinate direction, the memory requirement is $O(L^3)$. In most of the computations reported in this paper, about 3.5 million words of computer memory were needed, approximately the limit of main memory readilly accessible on the computer on which calculations were performed. If more main memory had been readily accessible, better results could have been obtained, in some cases, by decreasing the node spacing or enlarging the computational domain.

The FORTRAN code corresponding to the described algorithm was validated by comparison of the solution obtained for the case Re = 200 and $V = 1$, with results obtained in three independent investigations (see Section (3.2)). Computed solutions also compared favorably with solutions of the QC equations in the regions of validity of the QC equations.

The algorithm could be improved by including a mapping transformation, which would place a greater number of nodes in the region of the vortex core without increasing the amount of computer memory required. This step would also improve the resolution of flow structure in the breakdown region in those cases with reversed flow. Also, stability of solutions should be further examined by searching for Hopf points on the surfaces of equilibrium solutions computed in this work. Computed solutions that would benefit from a finer mesh discretization or a larger computational domain should be reexamined. This could be done by using a computer with a sufficiently large main memory (e.g., Cray-2) or by

utilizing an iterative method, such as the Multigrid method, in place of Newton's method and Gaussian elimination.

5.2 Transition Phenomenon

The central element of this paper is the observation that trailing vortices, under the assumptions of rotational symmetry, incompressibility, and steady flow, can undergo a transition between a state marked by slow growth of core radius with axial position and a state marked by spatial oscillation of core radius, lightly damped with axial position. The former state occurs upstream of the transition point, while the latter state occurs downstream of the transition point. The axial position of the transition point is precisely defined in Section (3.4). Transition was first observed by Beran (1987).

Transition is observed over a restricted range of vortex strengths, V, and over a wide range of Reynolds numbers. In most cases, the axial flow is assumed to be uniform over the inflow boundary of the computational domain, although transition is also observed when $a > 0$, where a is the excess in centerline axial velocity relative to the freestream velocity. The range of V, over which transition is observed, is restricted, since the position of the transition point, z_{tp}, is very sensitive to vortex strength. Transition first occurs when, as V is increased, the flow at some axial station in $\Re$ goes from a supercritical state to a subcritical state. Then, as V is slowly increased, the transition point moves rapidly upstream until the inflow boundary is reached. At this point, the only region of flow in $\Re$ which can be considered quasi-cylindrical is the flow near the outflow boundary, assuming that flow oscillations are sufficiently damped in the neighborhood of the outflow boundary. Further increase of V leads to changes in the structure of the wave train formed downstream of the inflow boundary, but does not lead to significant movement of the wave train relative to the boundary.

5.2.1 Reversed Flow

Reversed flow is not a necessary condition of transition, but reversed flow will occur downstream of the transition point if V is sufficiently large. In the past, the development of reversed flow in an isolated vortex has been referred to as "vortex breakdown." Many similarities between the breakdown of trailing vortices and the breakdown of tube vortices have been noted (Grabowski (1974)). It is observed in the results of this work that as V increases, centerline axial velocity, at the global minimum in centerline axial velocity just downstream of the transition point, decreases monotonically until reversed flow is obtained on the symmetry axis.

Although the appearance of a recirculation region represents a change in the structure of the flow, a corresponding change in the structure of the solution space of the Navier-Stokes equations does not necessarily occur. As an example, refer to the solution diagram shown in Figure (3.12). In this diagram, a solution branch (branch I) that is free of simple bifurcation points and limit points links solutions devoid of reversed flow to solutions that exhibit recirculation. When V is sufficiently large, the solution path does experience a fold, but only after a large recirculation region is formed near the inflow boundary (see Figure (3.13b)). Detachment of the recirculation bubble from the symmetry axis is the most probable cause for the development of a limit point on the solution path.

In the series of solutions described in Section (3.3.2), a transition point is not observed within the computational domain if recirculation is present. As V is increased, with Re = 200, the transition point moves upstream until the inflow boundary is reached. During this movement, the minimum value of centerline axial velocity remains positive, and the axial position of the minimum decreases. As V increases beyond the critical value at which the transtion point reaches the inflow boundary, the minimum value of centerline axial velocity decreases, eventually becoming negative, but the position of the minimum remains approximately constant.

A different series of events is observed to take place when the Reynolds number is large (Re $\geq$ 1000), or when a jetlike profile of axial velocity is specified at the inflow boundary ($a > 0$). For example, refer to the results presented in Section (3.6) for $a = 1.5$. As V is increased from 0.5, with Re = 250, a transition point forms and moves upstream with further increase of V. At $V = 2.4559$, a small recirculation bubble emerges downstream of the transition point. In contrast to the situation described above, the transition point is far downstream of the inflow boundary when recirculation is first evident. Also, as V increases beyond 2.4559, the continuation procedure essentially fails. Failure is signaled by the growth of short-period, numerical noise in computed solutions.

When both Reynolds number and vortex strength are sufficiently large, a small region of recirculation will develop while the transition point is downstream of the inflow boundary. Again, the development of recirculation immediately precedes the failure of the continuation process. Further work must be done to determine why the appearance of recirculation while the transition point is downstream of the inflow boundary leads to the emergence of numerical noise.

Based on the discussion above and on results presented in Chapter 4, the vortex flows that have been observed can be classified into four, generic types of flow states, described as follows.

1. The flow is entirely supercritical. The state can be accurately simulated using the QC equations, and is found when V is sufficiently small.

2. As V is increased, the flow becomes critical at an axial station, and a transition point develops. The point lies downstream of the inflow boundary and is trailed by a global minimum in centerline axial velocity. However, reversed flow is not observed.

3. In the third state, a small bubble of reversed flow is observed downstream of the transition point. The transition point remains downstream of the inflow boundary.

4. When V is sufficiently large, the entire flow is marked by large-amplitude, spatial oscillations of core radius. The transition point is not evident within the computational domain, and, typically, one or more large regions of reversed flow are observed.

It is possible that a transition point could be trailed by a large region of recirculation, but also lie downstream of the inflow boundary. In fact, such a situation is depicted in Figures (3.40c)—(3.40e). However, this potential flow state is not included in the classification above, since computed solutions in this category were substantially polluted by numerical noise.

5.2.2 Effects of Parameter Changes on z_{tp}

Further evidence that transition without reversed flow and vortex breakdown are related phenomena is provided by a comparison of the effects of parameter changes on z_{tp}, the position of the transition point, and the position of breakdown.

The effect of changes in vortex strength on z_{tp} is qualitatively the same as the effect of changes in circulation on the breakdown position of tube vortices. As V is increased, the transition point moves upstream (thereby decreasing z_{tp}). This is also the observed change in the position of the breakdown "bubble" of a tube vortex when the nondimensional circulation is increased (Faler and Leibovich (1977)). Also, Beran (1988) has found that imposing an external, adverse pressure gradient on the trailing vortex causes the transition point to move upstream with V and Re fixed. This has been the observed effect on the breakdown position of tube vortices as the tube divergence angle increases (except possibly when the vortex interacts with the boundary layer of the tube), with nondimensional circulation and Re fixed (Sarpkaya (1974)).

The qualitative effect of changes in Reynolds number on the position of the transition point is not, however, the same as on the position of the breakdown bubble. (The Reynolds number recorded in experiments is usually based on the average axial velocity and the diameter of the test section, while in this study,

Reynolds number is based on the freestream velocity and the radius of the vortex core.) The transition point moves downstream when Reynolds number is increased with V fixed, while the breakdown bubble of a tube vortex is observed to move upstream when Reynolds number is increased with nondimensional circulation fixed (Faler and Leibovich (1977)). This fundamental difference in behavior may be attributable to the fact that in experiment the profiles of nondimensional axial velocity, $w(r)$, and nondimensional swirl velocity, $v(r)$, at a station downstream of the tube centerbody vary with Reynolds number. Analysis of data provided by Faler and Leibovich indicates that as Reynolds number increases, the radius of the vortex core decreases, peak w increases and peak v increases. It is seen in this work that when peak v is increased with all variables fixed, the transition point moves upstream. Since, in experiment, the velocity profiles at the entrance to the test section are dependent on Reynolds number in a complicated way, it is perhaps not inconsistent that the position of the transition point varies with Reynolds number in a different manner than does the breakdown position.

5.2.3 Boundary Conditions on Inflow Vorticity

When V is sufficiently large, computed solutions are highly dependent on the choice of conditions enforced on azimuthal vorticity at the inflow boundary. In this work, two different conditions were examined. The first condition, $u(0,r) = 0$, led to (2.25). With this condition, vorticity at the inflow boundary is implicitly computed with the solution of (2.21). The second condition involves the explicit specification of vorticity on the inflow boundary by assuming the flow to be quasi-cylindrical at that boundary. With this assumption, azimuthal vorticity can be directly computed from the streamfunction profile specified at the inflow boundary via (3.1). The explicit condition on vorticity specifies that the axial gradient of radial velocity vanishes at the inflow boundary, $u_z(0,r) = 0$, or equivalently, through continuity, that $w_{zz}(0,r) = 0$. Using the explicit condition, solutions may be computed with large axial gradients in axial velocity at the inflow boundary

which violate the assumption of quasi-cylindrical flow at the boundary.

When V is not too large and the transition point lies far downstream of the inflow boundary, the computed solution is relatively insensitive to the choice of the inflow vorticity condition. With the implicit condition, transition occurs downstream of the transition point computed using the explicit condition (see Figure (3.29)). Consequently, the spatially oscillatory flow in the wake of transition is shifted by approximately the distance between transition points. In all other respects, however, computed solutions using the two inflow conditions are nearly identical.

The downstream shifting of the transition point with the implicit condition is a result of the flow adjusting to a quasi-cylindrical state, downstream of the inflow boundary, in which radial velocity is nonzero, but nearly constant with axial position. The adjustment is made in the first few grid points of the computational domain so that the centerline axial velocity profiles corresponding to both conditions parallel each other in the quasi-cylindrical flow region. In cases in which transition occurs far downstream of the inflow boundary, the explicit condition on vorticity is a more natural boundary condition, since it is consistent with the nature of the flow in the neighborhood of the boundary.

As V increases, the position of the transition point moves upstream, and when V is sufficiently large, transition occurs at the inflow boundary. The statement that transition occurs "at" the inflow boundary is taken to mean that the wave train begins at the boundary, and that the profile of centerline axial velocity in the neighborhood of the inflow boundary is similar in form to the profile in the neighborhood of a velocity maximum downstream of the inflow boundary. This situation is exemplified in Figure (3.25).

Transition occurs at the inflow boundary only when the implicit condition on inflow vorticity is specified. Once transition occurs at the inflow boundary, further increase of V does not change the axial position of the wave train, although the structure of the reversed flow region changes as the "bubble" of reversed flow lifts

off the symmetry axis. With this change in structure, centerline velocity varies asymmetrically with respect to z about local extrema in centerline axial velocity, and computed solutions become similar in appearance to the type 0 breakdown form observed by Faler and Leibovich (1977) and the breakdown bubbles computed by Brown and Lopez (1988). The implicit condition on inflow vorticity is a natural boundary condition to force the wave train to begin at the inflow boundary, since radial velocity vanishes at the points of the wave train where core radius is either a minimum or a maximum.

Indeed, solutions in which transition takes place at the inflow boundary could not be computed using the explicit condition on inflow vorticity. The sole reason is that by imposing the explicit condition, the axial gradient of radial velocity must vanish at the inflow boundary. Thus, a local maximum in axial velocity, of the kind observed downstream of the inflow boundary, cannot occur since w_{zz} is generally nonzero at these maxima.

Using the explicit condition, transition points are found to move upstream with increasing V. However, the continuation procedure generally fails before the transition point reaches the inflow boundary if the minimum value of centerline axial velocity is near 0 (i.e., if a recirculation bubble is nearly developed). This failure is discussed in Section (5.2.1).

From the results presented in Section (3.3.4), obtained using the explicit condition, it is found that the continuation procedure does not fail before the transition point reaches the inflow boundary. However, in this case, the minimum value of centerline axial velocity does not vanish while z_{tp} is positive. Reversed flow first occurs when z_{tp} is significantly negative, or in other words, when the transition point is upstream of the inflow boundary. The physical meaning of $z_{tp} < 0$ is unclear, since in this situation, axial gradients are large near the inflow boundary, in violation of the assumption of quasi-cylindrical flow at that boundary.

5.3 Flow Downstream of Transition

The flow downstream of the transition point approximates a spatially periodic flow. The quality of this approximation is dependent on the Reynolds number. At low Reynolds numbers, approximately 100, no wave train is discernible, and the flow monotonically approaches the conditions enforced at the radial boundary as axial position increases, starting from the point at which there is a global minimum in centerline axial velocity. If the Reynolds number is increased to 200, the approach is not monotonic, and local extrema are observed in the profile of centerline axial velocity between the global minimum and the outflow boundary (see Figure (3.6)). As Reynolds number continues to increase, the number of spatial oscillations experienced by the vortex increases, and the amplitude of these oscillations increases. Oscillation amplitude is largest just downstream of the transition point, decreasing with increased distance away from the point. The effect of viscosity on oscillation wavelength, as shown in Table (3.2), is an increase of wavelength with increased distance away from the transition point (except if oscillations are still of large amplitude at the outflow boundary, in which case wavelength may decrease with downstream position because of the presence of the boundary). Wavelength grows rapidly in the final few oscillations as seen in case NS701. As Reynolds number increases, the rate at which oscillation wavelength grows decreases.

The description above is consistent with the picture of the emergence of a spatially periodic flow downstream of the transition point as Reynolds number increases, or in other words, as the relative magnitude of viscous forces decreases. It is also found in Table (3.2), a tabulation of observed wavelengths for the cases NS701, NS703 and NS705, that the first wavelength of each wave train, λ_1, equals 24.5, independent of Reynolds number, and is assumed to remain true for Reynolds numbers larger than 20440 (case NS705). These observations indicate that the oscillatory flow downstream of the transition point is an inviscid phenomenon, and that the effect of viscosity is simply the slow decay of the amplitude of the wave

train.

Evidence of the existence of periodic, finite-amplitude waves in solutions of the Euler equations has been found by Táasan (1986) and Hafez et al. (1987). Táasan computed solutions of a nonlinear streamfunction equation, equivalent to the Euler equations for a special choice of streamfunction, circulation and azimuthal vorticity profiles at the inflow boundary of a computational domain, similar to the one employed in this work. These solutions were not periodic, but represented one-half of a single wave in an assumed wave train of infinite extent. Using continuation in vortex strength, finite-amplitude waves, often leading to bubbles of reversed flow attached to the symmetry axis, were computed. Periodic solutions of the same nonlinear streamfunction equation were obtained by Hafez et al. (1987). Periodic solutions were computed by enforcing a Dirichlet condition on streamfunction at the inflow boundary and a Neumann condition on streamfunction at the outflow boundary. Thus, wave trains occurring in solutions of the Navier-Stokes equations, as observed in this work, may be directly related to those periodic solutions of the Euler equations.

5.4 Experimental Evidence of Oscillatory Flow

The main limitation of this work, which prevents extensive comparison of results with experiment, is the assumption of rotational symmetry. In all experimental observations of vortex breakdown, some degree of asymmetry has been evident, both within the reversed flow region and in the breakdown wake (Faler and Leibovich (1977)), and is attributed to the instability of the underlying, axisymmetric flow to asymmetric disturbances (Leibovich (1983)). It is still an open question in the literature, however, whether breakdown would occur, regardless of asymmetries, if there was not a fundamental mechanism for the breakdown of strictly axisymmetric vortices. The results of this work clearly show that axisymmetric bursting of trailing vortices, possibly involving reversed flow, can occur. However, further work must be done to determine the effect of flow asymmetries

on the position of the transition point and on the structure of the flow downstream of the transition point. This work would necessarily involve the time integration of the Navier-Stokes without assumption of rotational symmetry, and is currently beyond the scope of this work.

Despite the problems associated with asymmetric instabilities, aspects of experimental observations of the structure of breakdown bubbles and the structure of the resulting wake flows are in qualitative agreement with present results. Sarpkaya (1971B) found that the sudden increase of the circulation of a tube vortex led to the temporary formation of a wave train involving up to three bubbles of reversed flow. Sarpkaya noted that the bubbles downstream of the primary bubble were rapidly destroyed by the upstream propagation of a spiral disturbance which, one by one, converted the bubbles into the spiral form of breakdown. The primary bubble was not destroyed in this process, but evolved in structure, to the form that would normally be observed at the new level of circulation. The destruction of bubbles downstream of the primary bubble may explain why steady-state trains of breakdown bubbles, as predicted by this work, are not observed in experiment.

Sarpkaya (1971A) and Faler and Leibovich (1977) observed that breakdown bubbles were generally trailed by breakdown structures of the spiral form. The results of the present work indicate that in the region downstream of the primary bubble, there will be a second minimum in centerline axial velocity, at which point the velocity may or may not be negative, depending on the Reynolds number and the strength of the vortex. In the case that one or more bubbles occur downstream of the primary bubble, these trailing bubbles are smaller and involve a lesser degree of recirculation than the primary bubble (cf. Figure (3.7)). Centerline axial velocity at the primary minimum may be greater than at other minimums (cf. Figure (3.8)), but in these cases, the region of reversed flow associated with the primary bubble has moved away from the vortex axis. Sarpkaya (1971B) found that weak vortices are susceptible to the spiral form of breakdown and that by sufficiently increasing the circulation of a vortex, initially supporting a breakdown of

the spiral form, breakdown of the bubble form would be obtained. If it is assumed that the spiral form of breakdown is the result of the instability of the axisymmetric swelling (of the kind seen in this work) of a weak vortex, then the results of this work would predict that breakdown bubbles are trailed by spiral forms of breakdown.

5.5 Comparison with Benjamin's Conjugate-Flow Theory

The theory of vortex breakdown that is in best agreement with the results described in this work is Benjamin's conjugate-flow theory (Benjamin (1967)). The theory is outlined in Chapter 1. According to Benjamin, the theory "proposes that vortex breakdown is fundamentally a transition from a uniform state of swirling flow to one featuring stationary waves of finite amplitude." This statement is an accurate account of the transition process observed in this study.

Benjamin predicted that in the absence of dissipative forces, a columnar flow that is supercritical may make a transition to a "conjugate" flow which is equivalent to the columnar flow plus a solitary wave, and that when a small amount of energy dissipation is allowed the columnar flow may make a transition to a flow which is equivalent to the columnar flow plus a wave train of finite-amplitude. The latter case is what is observed in this work.

There are several aspects of Benjamin's analysis that are either observed or found to be good approximations. First, the flow upstream of transition is well approximated by a columnar flow when the Reynolds number is sufficiently large. Because of viscous effects, the upstream flow is not strictly columnar, but axial gradients in the flow are generally small enough that the flow upstream of the transition point can be regarded as columnar (i.e., ψ_{zz} can be neglected with respect to other terms in the streamfunction equation, (2.1)). Second, the flow at the transition point is always observed to be supercritical (cf. Figure (3.38)), a condition found to be necessary by Benjamin for a conjugate flow to exist in the absence of external forces. Third, Benjamin assumed that

$$\beta/l^2 = -\gamma_o^2/l^2 = O[1], \tag{5.1}$$

where l is the length scale for axial changes in the conjugate flow and γ_o^2 is the eigenvalue of (1.10) of least magnitude. Given that that the upstream flow is supercritical, this eigenvalue is positive. As shown in Figure (3.38) $\beta \approx -0.0025$ and $l \approx 25$ for case NS705, where l is specified to be approximately the wavelength of the wave train downstream of the transition point. In this case (5.1) is satisfied, as was generally found to be true of other computed solutions in which transition was observed. Finally, the flow downstream of transition is found to be well approximated by a wave train supported by a columnar flow. When the Reynolds number is sufficiently large, the wavelength of flow oscillation is nearly constant with axial position.

There are two points on which the present results are in possible disagreement with the conjugate-flow theory. First, it is predicted by the theory that wave-train wavelength increases without bounds as the dissipation parameter, q, vanishes. This prediction implies that as Reynolds number increases (i.e., as the effect of viscosity is reduced), wavelength should increase. However, it is observed that as Reynolds number increases, wavelength approaches a limiting value. One explanation for this discrepancy involves the way in which the dissipation parameter is defined; q represents the integrated drop in total head between two conjugate flows in which total head is otherwise constant. In the computed flow, however, the total effect of viscosity is not simply applied at the transition point but is distributed throughout the flow downstream of the point. Since the extent of oscillatory flow grows as Reynolds number increases, the total head loss due to viscosity, measured at the end of the oscillatory flow region, does not vanish as Reynolds number increases. Thus, it is reasonable to assume that q does not vanish as $\mathrm{Re} \rightarrow \infty$.

Second, the amplitude of the computed wave is much larger than that assumed in the conjugate-flow theory. In the theory, it is assumed that $\epsilon/l^2 = O[1]$, a condition clearly violated near the vortex axis. There, changes in axial velocity are on the order of the freestream velocity. This observation does not imply,

however, that the conjugate-flow theory fails to account for the salient features of the transitional flow, but does suggest the need for a higher-order analysis in the context of the conjugate-flow theory.

5.6 Nonunique Solutions of the Navier-Stokes Equations

The discovery of nonunique solutions of the Navier-Stokes equations for the problem of vortex breakdown distinguishes this work from previous numerical investigations. The use of pseudo-arclength continuation was crucial to the calculation of such solutions. Examples of nonuniqueness are provided in Sections (3.3.2)—(3.3.4) for unbounded flows, and in Section (3.6) for flows through a frictionless pipe of constant radius. There are two important implications of the existence of nonunique solutions. First, disparities between the results of calculations of the time-dependent and steady-state Navier-Stokes equations may be attributable to this nonuniqueness, as will be discussed in more detail in Section (5.5). Second, nonuniqueness may help explain the experimentally observed interchange between different forms of vortex breakdown.

The calculation of nonunique solutions in the case of flow through a frictionless pipe is of particular interest, since time-dependent calculations for this flow situation have been by reported by Brown and Lopez (1988). There is also a substantial body of experimental results with which the present results can be compared. The solution diagram for solutions corresponding to different vortex strengths with Re = 250 is shown in Figure (3.39). In the figure, five distinct solution branches are evident, which have been labelled I, II, III, IV and V. Branches I and II compose the lowermost solution path in the diagram and are separated at the first limit point encountered when moving along branch II in the direction of decreasing V. Branches III, IV and V compose the uppermost solution path. Branches III and IV are separated at the limit point computed at $V = 2.2748$ while branches IV and V are separated at the point, just beyond $V = 2.46$, at which there is an abrupt change in slope of the solution path.

In the vicinity of the point $V = 2.46$ and $E_\Gamma = 4.2$ on the solution diagram, computed solutions exhibit a high degree of numerical noise. Apparently in this region of the solution space, the resolution of the computational grid is not sufficiently fine to resolve important structural events in the flow. One striking feature of this region, however, is the closeness to which a transcritical bifurcation is obtained. Although the two solution paths do not cross, each branch on one solution path appears to be a continuation of a branch on the other path. Furthermore, the signs of the determinants of branches IV and II are opposite, as is also true of branches I and V. The fact that a bifurcation point was not computed is probably due to the inaccuracy of flow calculcations in this region as described above.

5.7 Comparison with Results of Brown and Lopez

In Section (3.6.1), calculations for the case of flow through a frictionless pipe are compared with results reported by Brown and Lopez (1988). In contrast with the approach taken in this work, Brown and Lopez obtained time-dependent solutions of the governing equations by integrating the governing equations in time. They reported one time-dependent solution for the case $V = 2.3692$. In this simulation, the evolution of vortex breakdown from an initially uniform flow was observed. For large times, the computed breakdown structure was found to be very similar to that observed in experiment.

For the same value of the vortex strength examined by Brown and Lopez, three solutions of the steady-state equations were computed in the present study. This nonunique behavior is described in Sections (5.6) and (3.6.1), and is depicted in the solution diagram shown in Figure (3.39) for a wide range of vortex strengths. As proposed in Section (5.6), the solution on branch I for $V = 2.3692$ is stable, while the solution on branch IV for $V = 2.3692$ is unstable. The solution on branch III is found to share many qualitative features with the large-time solution obtained by Brown and Lopez. However, since Brown and Lopez observed that their evolutionary solution did not converge to a steady state, the stability of the

solution on branch III is open to question. The solution on branch I for $V = 2.3692$ was found to be entirely supercritical – further evidence that the solution is stable – and devoid of reversed flow.

Further work must be carried out to reconcile the apparent differences in results obtained by the two different algorithms. First of all, it is not clear that the evolutionary solution obtained by Brown and Lopez is independent of initial condition. Although their choice of uniform flow as an initial condition is certainly reasonable, the resulting evolutionary solution may not be attracted by the solution, presumably stable, on branch I.

This hypothesis could be tested by computing a series of time-dependent solutions for a sequence of values of the vortex strength. If V were sufficiently small, breakdown would not take place, and the flow would converge to a steady state qualitatively similar to flow states computed on branch I. Then, for example, an evolutionary solution could be computed for a slightly larger value of the vortex strength, using the previously obtained steady-state solution as an initial condition. If the difference between vortex strengths is not too large, then the second solution should also converge to a steady state. In principle, this process could be continued for successively larger values of V until either a steady-state solution for $V = 2.3692$ is obtained or until no steady-state solution is found. If the solution for $V = 2.3692$ on branch I is indeed stable, then such an approach should yield a steady-state solution identical to the one computed using the steady-state equations.

Another approach would be to allow V to increase slowly in time, starting with $V = 0$, until $V = 2.3692$ is reached, after which point the vortex strength is held constant. Again, if the solution on branch I is stable, and if the vortex strength is increased at a sufficiently slow rate, then the large-time solution should be identical with the solution obtained with the steady-state equations.

The stability of the solution for $V = 2.3692$ on branch III could also be assessed by integrating the time-dependent equations and by using the steady-state solution

as an initial condition. If the solution is unstable, then accumulation of roundoff errors should be sufficient to push the evolutionary solution away from the initial state. It is quite possible that such a solution would possess all the features of the evolutionary solution obtained by Brown and Lopez.

Brown and Lopez verified that (1.45), a necessary condition they proposed for the development of reversed flow (1988), was satisfied by the choice of $V = 2.3692$. However, since this condition is necessary, but not sufficient, satisfaction of the condition does not imply that the equilibrium solution on branch I for $V = 2.3692$ is unstable.

5.8 The Quasi-Cylindrical Approximation

The QC equations are found to provide an accurate description of the evolution of a trailing vortex in the flow region upstream of the transition point. Comparisons between solutions of the Navier-Stokes equations and the QC equations are presented in Section (4.2), and in all cases solutions were in excellent agreement upstream of the transition point.

Provided that Re is sufficiently large, it is found that z_{tp} varies linearly with Reynolds number, and that axial and azimuthal velocity profiles at the transition point are nearly independent of changes in Re. Also, z_{tp} does not appear to be dependent on axial gradients of the axial and azimuthal velocity profiles. Thus, a criterion or set of criteria based on the functional form of the axial and azimuthal velocity profiles should determine whether a flow makes a transition to an oscillatory state.

As mentioned in Section (5.3), the transition point was always found to occur in supercritical flow. Since the QC equations are singular at a critical point (see Appendix D), then the point at which the integration of these equations fails, z_{cr}, should lie downstream of the transition point. In all cases this was found to be true. The observation of a supercritical transition is in agreement with both Benjamin's conjugate-flow theory and Leibovich's nonlinear-wave model (1983).

Specifically, Leibovich predicts the upstream propagation of the wave system from z_{cr} to a point at which the wave system comes to rest.

Failure of the QC equations is found to be a necessary and sufficient condition for the existence of a transition point. If integration of the QC equations fails at some point, then a transition point is observed downstream of z_{cr} in the solution computed using the Navier-Stokes equations. And if integration of the QC equations does not fail, then transition is not observed. In the latter case, solutions of the QC and the Navier-Stokes equations are in excellent agreement over the entire computational domain.

Thus, integration of the QC equations may serve as a useful and efficient means by which the evolution of a trailing vortex can be simulated (for example, solutions of the QC equations presented here were computed on a microcomputer, while solutions of the Navier-Stokes equations were necessarily obtained on a supercomputer). When the QC equations are integrated without failure, then the solution is accurate over the entire domain. If, on the other hand, integration fails, then the position of the transition point, z_{tp}, can be estimated. Downstream of the transition point the QC equations are not valid, but the same may be claimed of the Navier-Stokes equations, when the flow is assumed to be steady and rotationally symmetric, because of the typical presence of flow asymmetries and turbulence. æ

Appendix A

Derivation of the Quasi-Cylindrical Equations

In direct analogy with the development of boundary-layer equations for two-dimensional, planar flows, a set of equations approximately governing the high Reynolds number behavior of rotationally symmetric, viscous vortices can be derived. These equations, first proposed for the study of vortex breakdown by Gartshore (1962), are referred to in the literature as the "quasi-cylindrical" equations and will henceforth be referred to as the QC equations. Numerically computed solutions of the QC equations have been reported for a variety of internal and external vortical flows. An analytical solution to a linearized form of the QC equations has also been found for a trailing-vortex flow. The QC equations have an important role in the investigation of vortex breakdown as the equations contain a singularity at the point at which the flow becomes critical (see Appendix D).

This appendix contains a derivation of the QC equations. The QC equations are cast in dimensional and nondimensional form. Scalings used to obtain the nondimensional equations provide a description of how properties in the layer change with Re, a Reynolds number based on layer thickness. Solutions of the Navier-Stokes equations are compared with solutions of the QC equations in Chapter 4. Transition point position is found to vary with Re in a way predicted by the QC equations, assuming that transition is dependent only on the local state of the axial and azimuthal velocity profiles.

A.1 Boundary-Layer Hypothesis

The starting point of the derivation of the boundary-layer equations is the boundary-layer hypothesis attributed to Prandtl (1905). Generally speaking, this hypothesis proposes that in convection-dominated flows, viscosity is important only in thin layers adjacent to solid boundaries and in thin layers formed by flow separation that are subsequently convected downstream. Trailing vortices fall into the latter category and are marked by a viscous core lying on a line approximately aligned with the freestream flow. A consequence of the hypothesis is that, stability considerations aside, layer thinness approaches zero as the Reynolds number of the flow goes to infinity.

Within these layers, lateral diffusion of vorticity becomes as important as vorticity convection, a condition that qualitatively defines layer thickness, δ, through the following order-of-magnitude relation (Batchelor (1967)):

$$O\left(\frac{\partial^2\eta}{\partial r^2}/w\frac{\partial\eta}{\partial z}\right) = 1. \tag{A.1}$$

An appropriate scale for the axial velocity is the freestream velocity, W. Assuming that axial changes within the layer have a length scale of L and that radial changes within the layer have a length scale of δ, (A.1) gives

$$\delta \sim L\mathrm{Re}_L^{-1/2} \quad \text{as } \mathrm{Re}_L \to \infty, \tag{A.2}$$

where $\mathrm{Re}_L \equiv WL/\nu$ is a Reynolds number based on the axial length scale.

The radial velocity scale, U, is determined from the continuity equation,

$$\frac{\partial w}{\partial z} + \frac{u}{r} + \frac{\partial u}{\partial r} = 0. \tag{A.3}$$

Order-of-magnitude analysis gives

$$O\left(\frac{\partial w}{\partial z}/\frac{1}{r}\frac{\partial(ru)}{\partial r}\right) = 1, \tag{A.4}$$

so that

$$U \sim W\mathrm{Re}_L^{-1/2} \quad \text{as } \mathrm{Re}_L \to \infty. \tag{A.5}$$

A.2 Nondimensional QC Equations — Form I

Using the asymptotic relations for δ and W, an approximate form of the Navier-Stokes equations, valid in the limit of infinite Reynolds number, can be derived. Following the approach of Batchelor (1967) the dependent and independent variables are scaled as follows (primed variables are nondimensional):

$$\delta = L\mathrm{Re}_L^{-1/2} \tag{A.6}$$

$$U = W\mathrm{Re}_L^{-1/2} \tag{A.7}$$

$$r' = \frac{r}{\delta} = \mathrm{Re}_L^{1/2}\frac{r}{L} \tag{A.8}$$

$$z' = \frac{z}{L} \tag{A.9}$$

$$u' = \frac{u}{U} = \mathrm{Re}_L^{1/2}\frac{u}{W} \tag{A.10}$$

$$v' = \frac{v}{W} \tag{A.11}$$

$$w' = \frac{w}{W} \tag{A.12}$$

$$p' = \frac{p - p_\infty}{\rho W^2}. \tag{A.13}$$

After some manipulation, substitution of these scalings into the Navier-Stokes equations (2.1—2.3) gives

$$\frac{\partial w'}{\partial z'} + \frac{u'}{r'} + \frac{\partial u'}{\partial r'} = 0 \tag{A.14}$$

$$\frac{1}{\mathrm{Re}_L}\left(u'\frac{\partial u'}{\partial r'} + w'\frac{\partial u'}{\partial z'}\right) + \frac{\partial p'}{\partial r'} - \frac{v'^2}{r'}$$

$$= \frac{1}{\mathrm{Re}_L}\left(\frac{1}{\mathrm{Re}_L}\frac{\partial^2 u'}{\partial z'^2} + \frac{\partial^2 u'}{\partial r'^2} + \frac{1}{r'}\frac{\partial u'}{\partial r'} - \frac{u'}{r'^2}\right) \tag{A.15}$$

$$u'\frac{\partial v'}{\partial r'} + w'\frac{\partial v'}{\partial z'} + \frac{u'v'}{r'} = \frac{1}{\mathrm{Re}_L}\frac{\partial^2 v'}{\partial z'^2} + \frac{\partial^2 v'}{\partial r'^2} + \frac{1}{r'}\frac{\partial v'}{\partial r'} - \frac{v'}{r'^2} \tag{A.16}$$

$$u'\frac{\partial w'}{\partial r'} + w'\frac{\partial w'}{\partial z'} + \frac{\partial p'}{\partial z'} = \frac{1}{\mathrm{Re}_L}\frac{\partial^2 w'}{\partial z'^2} + \frac{\partial^2 w'}{\partial r'^2} + \frac{1}{r'}\frac{\partial w'}{\partial r'}. \tag{A.17}$$

Equations (A.14—A.17) involve a single free parameter, Re_L. In the limit of $\mathrm{Re}_L \to \infty$, the three momentum equations become independent of this parameter, simplifying to

$$\frac{\partial p'}{\partial r'} = \frac{v'^2}{r'} \tag{A.18}$$

$$u'\frac{\partial v'}{\partial r'} + w'\frac{\partial v'}{\partial z'} + \frac{u'v'}{r'} = \frac{\partial^2 v'}{\partial r'^2} + \frac{1}{r'}\frac{\partial v'}{\partial r'} - \frac{v'}{r'^2} \tag{A.19}$$

$$u'\frac{\partial w'}{\partial r'} + w'\frac{\partial w'}{\partial z'} + \frac{\partial p'}{\partial z'} = \frac{\partial^2 w'}{\partial r'^2} + \frac{1}{r'}\frac{\partial w'}{\partial r'}. \tag{A.20}$$

The QC equations, in nondimensional form, consist of the continuity equation (A.14) and the three momentum equations (A.18—A.20) and are accurate (away from the singularity contained in the equations) for sufficiently large values of Re_L.

A.3 Dimensional QC Equations

The QC equations are obtained in dimensional form by substituting (A.8—A.13) into (A.14) and (A.18—A.20):

$$\frac{\partial w}{\partial z} + \frac{u}{r} + \frac{\partial u}{\partial r} = 0 \tag{A.21}$$

$$\frac{1}{\rho}\frac{\partial p}{\partial r} = \frac{v^2}{r} \tag{A.22}$$

$$u\frac{\partial v}{\partial r} + w\frac{\partial v}{\partial z} + \frac{uv}{r} = \nu\left(\frac{\partial^2 v}{\partial r^2} + \frac{1}{r}\frac{\partial v}{\partial r} - \frac{v}{r^2}\right) \tag{A.23}$$

$$u\frac{\partial w}{\partial r} + w\frac{\partial w}{\partial z} + \frac{1}{\rho}\frac{\partial p}{\partial z} = \nu\left(\frac{\partial^2 w}{\partial r^2} + \frac{1}{r}\frac{\partial w}{\partial r}\right). \tag{A.24}$$

A.4 Nondimensional QC Equations — Form II

A more useful formulation of the nondimensional QC equations introduces a Reynolds number based on the length scale, δ_o, the core radius at the inflow boundary. This Reynolds number, $\mathrm{Re} \equiv W\delta_o/\nu$, is the same used in the nondimensionalization of the governing equations in Chapter 2. Scaling lengths by δ_o and velocities by W give a new set of nondimensional variables:

$$r' = \frac{r}{\delta_o} \tag{A.25}$$

$$z' = \frac{z}{\delta_o} \tag{A.26}$$

$$u' = \frac{u}{W} \tag{A.27}$$

$$v' = \frac{v}{W} \tag{A.28}$$

$$w' = \frac{w}{W} \tag{A.29}$$

$$p' = \frac{p - p_\infty}{\rho W^2}. \tag{A.30}$$

Substitution of (A.25—A.30) into (A.21—A.24) gives a second form of the nondimensional QC equations:

$$\frac{\partial w'}{\partial z'} + \frac{u'}{r'} + \frac{\partial u'}{\partial r'} = 0 \tag{A.31}$$

$$\frac{\partial p'}{\partial r'} = \frac{v'^2}{r'} \tag{A.32}$$

$$u'\frac{\partial v'}{\partial r'} + w'\frac{\partial v'}{\partial z'} + \frac{u'v'}{r'} = \frac{1}{\mathrm{Re}}\left(\frac{\partial^2 v'}{\partial r'^2} + \frac{1}{r'}\frac{\partial v'}{\partial r'} - \frac{v'}{r'^2}\right) \tag{A.33}$$

$$u'\frac{\partial w'}{\partial r'} + w'\frac{\partial w'}{\partial z'} + \frac{\partial p'}{\partial z'} = \frac{1}{\mathrm{Re}}\left(\frac{\partial^2 w'}{\partial r'^2} + \frac{1}{r'}\frac{\partial w'}{\partial r'}\right). \tag{A.34}$$

A.5 Nondimensional QC Equations — Form III

Numerical solutions of the QC equations were computed with the equations cast in terms of the dependent variables (ψ, η, Γ) instead of the dependent variables (u', v', w', p'). In this form, solutions of the QC equations could be directly compared with solutions of the Navier-Stokes equations, (2.1—2.3).

With the definitions

$$\psi_z \equiv -r'u' \tag{A.35}$$

$$\psi_r \equiv r'w' \tag{A.36}$$

$$\eta \equiv -\frac{1}{r'}\frac{\partial w'}{\partial r'} \tag{A.37}$$

$$\Gamma \equiv r'v', \tag{A.38}$$

the continuity equation (A.31) is identically satisfied and the momentum equations (A.32—A.34) become

$$\psi_{rr} - \psi_r/r = -r\eta \tag{A.39}$$

$$\frac{\psi_r\Gamma_z}{r} - \frac{\psi_z\Gamma_r}{r} = \frac{1}{\mathrm{Re}}\left(\Gamma_{rr} - \Gamma_r/r\right) \tag{A.40}$$

$$\frac{\psi_r\eta_z}{r} - \frac{\psi_z\eta_r}{r} + \frac{\psi_z\eta}{r^2} = \frac{2\Gamma\Gamma_z}{r^3} + \frac{1}{\mathrm{Re}}\left(\eta_{rr} + \eta_r/r - \eta/r^2\right) \tag{A.41}$$

(note that in (A.39)—(A.41) unprimed variables are assumed to be nondimensional).

A.6 Solution Similarity

One solution of the nondimensional QC equations, Form I, represents a one-parameter family of solutions, in the parameter Re, of the nondimensional QC equations written as Form II. This fact can be used to establish similarity relations between two members of the family. Consider two such members and let Re_1 and Re_2 be the Reynolds numbers corresponding to those solutions. It is assumed that the boundary conditions, discussed in Chapter 2, are identical in both cases. Suppose that flow properties at station z_1 of the first solution and z_2 of the second solution are compared. Equation (A.8) gives

$$\frac{r_1}{\delta_o} = \left(\frac{z_1}{\delta_o}\right)^{1/2} \mathrm{Re}_1^{-1/2} r' \tag{A.42}$$

$$\frac{r_2}{\delta_o} = \left(\frac{z_2}{\delta_o}\right)^{1/2} \mathrm{Re}_2^{-1/2} r'. \tag{A.43}$$

If z_1 and z_2 are chosen such that

$$\frac{z_1}{\delta_o}\mathrm{Re}_1^{-1} = \frac{z_2}{\delta_o}\mathrm{Re}_2^{-1}, \tag{A.44}$$

then flow property profiles with respect to radial position, r/δ_o, will have the same functional form. Using (A.44) with (A.10—A.12) gives the following similarity relationships:

$$u(\frac{r}{\delta_o}, z_1, \mathrm{Re}_1) = \frac{\mathrm{Re}_2}{\mathrm{Re}_1} u(\frac{r}{\delta_o}, \frac{\mathrm{Re}_2}{\mathrm{Re}_1} z_1, \mathrm{Re}_2) \tag{A.45}$$

$$v(\frac{r}{\delta_o}, z_1, \mathrm{Re}_1) = v(\frac{r}{\delta_o}, \frac{\mathrm{Re}_2}{\mathrm{Re}_1} z_1, \mathrm{Re}_2) \tag{A.46}$$

$$w(\frac{r}{\delta_o}, z_1, \mathrm{Re}_1) = w(\frac{r}{\delta_o}, \frac{\mathrm{Re}_2}{\mathrm{Re}_1} z_1, \mathrm{Re}_2). \tag{A.47}$$

In Section (4.4), these relationships are shown to be satisfied by solutions of the Navier-Stokes equations in approach flows leading to transition.

Appendix B

Solution Procedure for Discrete Models

The system of nonlinear algebraic equations (2.21) can be solved through a variety of iterative methods. In the present work, solutions were computed through the combined use of Newton's method and the pseudo-arclength continuation method. This appendix will be devoted to a description of these two methods.

We consider systems of nonlinear algebraic equations of the form

$$\underline{F}(\underline{x};\lambda) = 0, \tag{B.1}$$

where $\underline{F}$ is a set of N equations dependent on $\underline{x}$ and λ. $\underline{x}$ is an N-dimensional vector that we wish to calculate, and λ is a free scalar parameter. Since $\underline{F}$ depends on λ, the solution vector, $\underline{x}$, generally depends on λ. Newton's method is an algorithm to compute $\underline{x}$ for a specified value of λ and the pseudo-arclength continuation method, like other continuation methods, is an algorithm to use this solution to compute another solution corresponding to a different value of λ.

With grid geometry fixed, the system of equations (2.21) is dependent on three free parameters: Re, V and a. When applying the continuation procedure outlined in this appendix, one of these parameters is allowed to vary, while the others are held fixed. In this way, (2.21) can be represented by the model system (B.1). Thus, for example, solutions are computed for a sequence of different Reynolds numbers, with V and a held constant, or solutions are computed for a sequence of vortex strengths, with Re and a held fixed. It is possible to perform continuation with two free parameters, if additional constraints are added to the system, but such an approach was not attempted in this work.

B.1 Newton's Method

When used with continuation (described below), Newton's method is a robust algorithm for computing solutions to systems of equations such as (B.1). The algorithm is iterative. Given λ and an initial approximation to the solution vector, $\underline{x}^i$, one Newton iterate consists of the computation of an improved approximation, $\underline{x}^{i+1}$, obtained by solving the linear system of equations,

$$\underline{F}_{\underline{x}}(\underline{x}^i;\lambda)\left(\underline{x}^{i+1}-\underline{x}^i\right) = -\underline{F}(\underline{x}^i;\lambda). \tag{B.2}$$

Successive Newton iterates are computed until the weighted L2 norm of the residuals,

$$||\underline{r}||_2 \equiv \left(\sum_{k=1}^{N} h_z h_r F_k^2(\underline{x}^{i+1};\lambda)\right)^{1/2},$$

becomes tolerably small (assuming h_r and h_z are the node spacings in the two coordinate directions of the computational domain).

The linear operator in (B.2) is the Jacobian matrix, the elements of which are given by

$$\underline{F}_{\underline{x}} \equiv \left[\frac{\partial F_i}{\partial x_j}\right].$$

In this study, Jacobian matrices were computed by evaluating analytically derived expressions for matrix elements at the current solution estimate.

Newton's method was used since it is reliable, easy to program, and will, under certain conditions, find solutions to (B.1) in just a few iterations. If the Jacobian matrix is nonsingular at the solution, $\underline{x}^*$, and if the initial guess, $\underline{x}^i$, is sufficiently good, then Newton's method is guaranteed to converge with a quadratic convergence rate. The systems of linear equations encountered with each Newton iterate were solved to machine precision by Gaussian elimination with partial pivoting. In computing solutions of (B.1), the Newton iteration process was stopped when the residual norm decreased below 10^{-10}. The Jacobian matrix was defined to be singular if in the process of solving (B.1), the maximum pivot had a magnitude of less

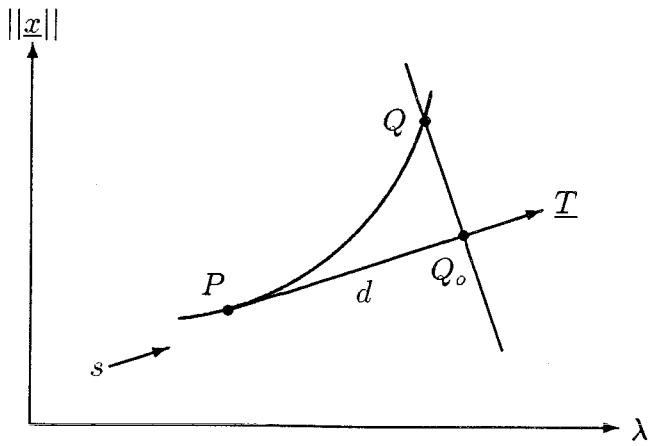

Figure B.1 Illustration of continuation procedure

than about 100 times machine precision. No singular matrices were encountered in any of the computations performed.

B.2 Pseudo-Arclength Continuation

The process of computing successive solution points is, in effect, the computation of the solution path, $\underline{x}(\lambda)$, and is referred to as "continuation." The continuation method used in this study was Keller's (1977) pseudo-arclength continuation method. For a review of continuation methods and their application to computational fluid dynamics, see Keller (1982).

To facilitate the description of Keller's method, refer to Figure (B.1), which shows the solution path, $\underline{x}(\lambda)$, as it appears when the norm of the solution vector is plotted against λ. Choose arclength, s, to parameterize the path, so that on the path, $\underline{x} = \underline{x}(s)$, $\lambda = \lambda(s)$ and $\underline{F} = \underline{F}(s) = 0$. The first step in the continuation process is to compute the vector tangent to the solution path at a known solution point. From

$$\frac{d}{ds}\underline{F}(\underline{x}(s);\lambda(s)) = 0 \tag{B.3}$$

and the chain-rule,

$$\underline{F}_{\underline{x}}(s)\dot{\underline{x}}(s) + \underline{F}_{\lambda}(s)\dot{\lambda}(s) = 0, \tag{B.4}$$

where

$$\dot{\underline{x}}(s) \equiv \frac{d\underline{x}}{ds}(s) \tag{B.5}$$

$$\dot{\lambda}(s) \equiv \frac{d\lambda}{ds}(s) \tag{B.6}$$

and

$$\underline{F}_{\lambda} \equiv \frac{\partial \underline{F}}{\partial \lambda}. \tag{B.7}$$

The definition of arclength is

$$||\dot{\underline{x}}(s)||^2 + \dot{\lambda}^2(s) = 1. \tag{B.8}$$

Conditions (B.4) and (B.6) can be solved for the tangent vector,

$$\underline{T}(s) \equiv \left(\dot{\underline{x}}(s), \dot{\lambda}(s)\right)^T, \tag{B.9}$$

at points on the solution path for which the Jacobian matrix is nonsingular. Define $\underline{\phi}$ such that

$$\underline{\phi} = \underline{F}_{\underline{x}}^{-1}(s)\underline{F}_{\lambda}(s). \tag{B.10}$$

Then (B.4) and (B.6) give

$$\dot{\lambda}(s) = \pm 1/\left(1 + ||\phi||^2\right)^{1/2} \quad \text{and} \tag{B.11}$$

$$\dot{\underline{x}}(s) = -\dot{\lambda}(s)\underline{\phi}. \tag{B.12}$$

The sign in (B.9) is indeterminate because the tangent can point in either the direction of increasing s or decreasing s.

Given a known solution point, P, a neighboring solution point, Q, is required to lie on a planar manifold perpendicular to the path tangent projected from the known solution point (see Figure (B.1)). The parameter d fixes the distance between the point P and the intersection point, Q_o, of the path tangent and the planar manifold perpendicular to the tangent. Thus,

$$\begin{pmatrix} \underline{x} \\ \lambda \end{pmatrix}_{Q_o} = \begin{pmatrix} \underline{x} \\ \lambda \end{pmatrix}_P + d \begin{pmatrix} \dot{\underline{x}} \\ \dot{\lambda} \end{pmatrix}_P .$$

The condition that Q lie on a planar manifold perpendicular to the path tangent at Q_o is

$$D\left(\underline{x}_Q; \lambda_Q\right) \equiv \dot{\underline{x}}_P^T(\underline{x}_Q - \underline{x}_P) + (\lambda_Q - \lambda_P)\dot{\lambda}_P = d, \tag{B.13}$$

and is added to (B.1) to form an enlarged system of nonlinear equations. An initial approximation to the solution point Q is the point Q_o and is a good approximation if d is small compared to the local radius of curvature of the solution path. The initial approximation is improved through Newton iteration until a converged solution to $\underline{F} = \underline{0}$ and $D = d$ is found. A Newton iterate of the enlarged system of nonlinear equations requires the computation of the solution of the linear system,

$$\underline{F}_{\underline{x}}^i(\underline{x}^{i+1} - \underline{x}^i) + \underline{F}_{\lambda}^i(\lambda^{i+1} - \lambda^i) = -\underline{F}^i \tag{B.14}$$

$$\dot{\underline{x}}_P^T(\underline{x}^{i+1} - \underline{x}^i) + \dot{\lambda}_P(\lambda^{i+1} - \lambda^i) = d - D^i. \tag{B.15}$$

After the solution point Q has been calculated, another point on the path is found by repeating the process outlined above.

In this work, the solution path is graphically represented by plotting the free parameter (e.g., Re) against the weighted L2 norm of the deviation of $\Gamma_{(i,j)}$ from $\Gamma_{o(j)}$:

$$E_\Gamma \equiv \left(h_z h_r \sum_{i=1}^{I} \sum_{j=1}^{J} (\Gamma_{(i,j)} - \Gamma_{o(j)})^2 \right)^{1/2} . \tag{B.16}$$

Recall that $\Gamma_o(r)$ is the circulation profile specified at the inflow boundary. The norm E_Γ will also be referred to as the "circulation perturbation" norm.

Appendix C

Linearized Analysis of Inviscid, Columnar Vortices

This appendix contains a derivation of an Orr—Sommerfeld equation for inviscid, columnar vortices. The purpose in this derivation is not to determine the stability of such vortices, a task that has already been performed by Howard and Gupta (1962), but to develop an equation by which the criticality of a columnar flow can be examined and the effects of phase velocity observed. The equation is used in Chapter 3 to evaluate the change in criticality, as a function of axial position, of solutions of the Navier-Stokes equations for trailing vortices, assuming that vortex evolution is sufficiently slow.

C.1 Development of Orr-Sommerfeld Equation

The time-dependent equations of motion for an inviscid, rotationally symmetric vortex are (see Chapter 2 for definitions of ψ, η and Γ):

$$\psi_{zz} + \psi_{rr} - \frac{1}{r}\psi_r = -r\eta, \tag{C.1}$$

$$\eta_t - \frac{1}{r}\psi_z\eta_r + \frac{1}{r}\psi_r\eta_z + \frac{1}{r^2}\psi_z\eta = \frac{2}{r^3}\Gamma\Gamma_z, \tag{C.2}$$

$$\Gamma_t - \frac{1}{r}\psi_z\Gamma_r + \frac{1}{r}\psi_r\Gamma_z = 0. \tag{C.3}$$

Columnar solutions of (C.1—C.3) are those steady-state flows that are independent of z. Columnar flows may have arbitrary axial and azimuthal velocity distributions with respect to the r coordinate. The ability of columnar, or "primary," flows to

support waves of infinitesimal amplitude is assessed by assuming solutions of the form:

$$\psi(r,z) = \psi_o(r) + \epsilon e^{ik(z-ct)}\psi_1(r), \tag{C.4}$$

$$\eta(r,z) = \eta_o(r) + \epsilon e^{ik(z-ct)}\eta_1(r), \tag{C.5}$$

$$\Gamma(r,z) = \Gamma_o(r) + \epsilon e^{ik(z-ct)}\Gamma_1(r), \tag{C.6}$$

where $\psi_o(r)$, $\eta_o(r)$ and $\Gamma_o(r)$ satisfy (C.1—C.3), and $\epsilon << 1$. Disturbance wave number, k, is chosen to be real while phase velocity, c, is assumed complex: $c \equiv c_r + ic_i$. Substitution of (C.4—C.6) into (C.1—C.3) yields, in the limit $\epsilon \to 0$:

$$-k^2\psi_1 + \ddot{\psi}_1 - \frac{1}{r}\dot{\psi}_1 = -r\eta_1, \tag{C.7}$$

$$-c\eta_1 - \frac{\dot{\eta}_o}{r}\psi_1 + \frac{\dot{\psi}_o}{r}\eta_1 + \frac{\eta_o}{r^2}\psi_1 = \frac{2\Gamma_o}{r^3}\Gamma_1, \tag{C.8}$$

$$-c\Gamma_1 - \frac{\dot{\Gamma}_o}{r}\psi_1 + \frac{\dot{\psi}_o}{r}\Gamma_1 = 0. \tag{C.9}$$

Note that terms of $O(\epsilon^2)$ have been dropped. Γ_1 is eliminated by combining (C.8) and (C.9) to give

$$(w_o - c)\eta_1 - \frac{\dot{\eta}_o}{r}\psi_1 + \frac{\eta_o}{r^2}\psi_1 = \frac{2\Gamma_o\dot{\Gamma}_o}{r^4(w_o - c)}\psi_1, \tag{C.10}$$

where $w_o \equiv \frac{1}{r}\dot{\psi}_o$. Singular neutral modes may exist for which $w_o - c = 0$. The behavior of these modes will not be investigated since, assuming that w_o is a nonnegative function of r, their existence will not affect the determination of flow criticality. Thus, assuming that $w_o \neq c$,

$$\eta_1 = \left(\frac{\psi_1}{w_o - c}\right)\left[\frac{2\Gamma_o\dot{\Gamma}_o}{r^4(w_o - c)} + \frac{\dot{\eta}_o}{r} - \frac{\eta_o}{r^2}\right]. \tag{C.11}$$

Finally, η_1 is eliminated by combining (C.7) and (C.11), leading to a second-order differential equation for the disturbance streamfunction, ψ_1:

$$\ddot{\psi}_1 - \frac{\dot{\psi}_1}{r} + \frac{1}{(w_o - c)}\left[\frac{2\Gamma_o\dot{\Gamma}_o}{r^3(w_o - c)} + \dot{\eta}_o - \frac{\eta_o}{r}\right]\psi_1 = k^2\psi_1. \tag{C.12}$$

Equation (C.12) has been derived previously, in slightly different forms, by Chandrasekhar (1961), Howard and Gupta (1962) and Benjamin (1965).

In the far-field, w_1 ($w_1 = \frac{1}{r}\dot{\psi}_1$) must vanish so that, for some $r = R$ in the far-field,

$$\dot{\psi}_1(R) = 0. \tag{C.13}$$

On the vortex axis $\psi(z, 0) = 0$, or equivalently,

$$\psi_1(0) = 0. \tag{C.14}$$

Equations (C.12—C.14) comprise an eigenvalue problem for k^2. For a specified phase speed, there exists an infinite spectrum of eigenvalues, but only eigenvalues satisfying $k^2 > 0$ (i.e., k real and positive) correspond to physically realizable waves.

C.2 Assessment of Flow Criticality

The criticality of a columnar flow depends on its ability to support standing waves of infinitesimal amplitude. As defined by Benjamin (1962), a columnar flow is "supercritical" when all eigenvalues are negative and "subcritical" when at least one eigenvalue is positive for the case $c = 0$. The flow is "critical" when one eigenvalue is identically zero, corresponding to a standing wave of infinite wavelength, and all other eigenvalues are negative.

Hall (1972) has formally shown that the notion of flow criticality can be extended to quasi-cylindrical flows in which core properties change slowly with axial position. In this case, flow criticality can change with axial position and is decided on the basis of the axial and azimuthal velocity profiles at a particular axial station, using the analysis presented above for columnar vortices.

Two special cases of (C.12) will be focused upon in this appendix. First, in preparation for the evaluation of the criticality of solutions presented in Chapters 3 and 4, the case of $c = 0$ is examined. Then, the special case of $w_o(r) = 1$ is

treated in the next section to demonstrate the relationship between flow criticality and the phase speed of supportable neutral waves.

For standing waves, $c = 0$ and (C.12) becomes

$$\ddot{\psi}_1 - \frac{1}{r}\dot{\psi}_1 + \left(\frac{\Phi}{w_o^2} - \frac{\ddot{w}_o}{w_o} + \frac{\dot{w}_o}{r w_o}\right)\psi_1 = k^2\psi_1, \tag{C.15}$$

where $\eta_o = -\dot{w}_o$ has been used and

$$\Phi \equiv \frac{2\Gamma_o\dot{\Gamma}_o}{r^3}. \tag{C.16}$$

Equation (C.15) with the boundary conditions (C.13) and (C.14) form an eigenvalue problem for k^2. A discrete spectrum of eigenvalues, approximating the true spectrum, is computed by replacing (C.15) with a system of linear equations, obtained by discretization of the continuum equation through use of central-difference operators. The line between $r = 0$ and $r = R$ is discretized with a set of evenly spaced nodes at which (C.15) is approximated. At nodes adjacent to boundary nodes, the discrete equations are modified to account implicitly for the boundary conditions. Condition (C.13) is approximated with a second-order accurate, one-sided difference expression. Eigenvalues are computed with the IMSL EIGRF subroutine. Flow criticality at various axial stations of solutions presented in Chapter 3 is computed by using a node arrangement in the eigenvalue analysis equivalent to that used in the viscous calculation and by using the azimuthal vorticity and circulation data resulting from the viscous calculation.

C.3 Neutral Waves for the Special Case $w_o = 1$

Benjamin (1962, 1965) has shown that for neutral waves of extreme wavelength ($k \to 0$), two waves exist that have the largest phase velocities relative to the primary flow and that when the primary flow is supercritical, both waves propagate downstream, while when the flow is subcritical, one wave has negative phase speed. Thus, supercritical and subcritical flows may be differentiated by the phase speed of neutrally stable waves of extreme wavelength that the flow can support.

The example treated in this section provides a demonstration (not a proof), using the analysis outlined in the previous section, that differentiation between supercritical and subcritical flows according to the phase speed of supportable neutral waves is applicable to waves not of extreme wavelength.

Consider the special case of a columnar vortex with $w_o(r) = 1$ and the circulation profile (which was also used as an inflow boundary condition for the Navier-Stokes model):

$$\Gamma_o(r) = \begin{cases} V & r \geq 1 \\ Vr^2(2 - r^2) & r < 1. \end{cases} \tag{C.17}$$

With the assumption of $w_o(r) = 1$, (C.15) is now written as

$$\ddot{\psi}_1 - \frac{1}{r}\dot{\psi}_1 + \Phi(V)\psi_1 = k^2\psi_1, \tag{C.18}$$

where Φ is a function of the vortex strength, V. Results of the solution of the eigenvalue problem are shown in Figure (C.1) for three different phase speeds. The figure shows that as V is increased from 0, standing waves ($c_r = 0$) are first possible when $V \approx 0.968$. At this point, representative of the critical state, the supportable standing wave is of infinite wavelength. Subcritical states support standing waves of finite wavelength and occur for values of V larger than that marking the critical state. In distinction, supercritical states cannot support standing waves and occur for values of V smaller than the critical value.

Neutral waves with positive phase velocity are supported by a supercritical state as shown in Figure (C.1) for the case of $c_r = 0.1$. Subcritical states support neutral waves with both positive and negative phase speed, although upstream propagating waves are of greater wavelength than waves with positive phase speed. The results are not conclusive, since only two nonzero phase speeds were examined. However, the results support the categorization of a primary flow as supercritical if neutral waves of extreme wavelength have positive phase speed, since it appears, in the special case treated here, that the same is true for waves of moderate wavelength.

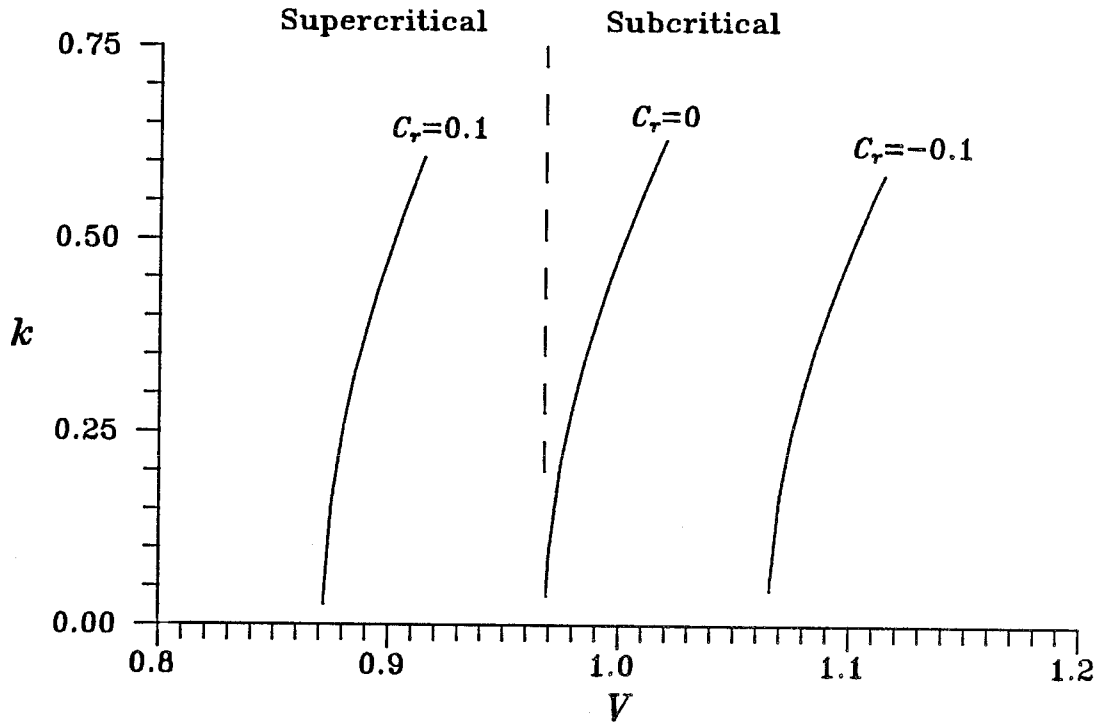

Figure C.1 Wavenumber of neutral wave vs. V for c_r = -0.1, 0 and 0.1

C.4 Remarks on the Linear Stability of Columnar Vortices

Leibovich (1984) has given a summary of stability and instability criteria for columnar vortices, including criteria for nonaxisymmetric as well axisymmetric disturbances. The main result, from the perspective of this work, is the stability condition established by Howard and Gupta (1962). This is a sufficient condition for stability, stating that a columnar vortex is stable to axisymmetric disturbances, if

$$J \equiv \frac{\Phi}{\dot{w}^2} \geq \frac{1}{4} \tag{C.19}$$

over the entire interval $0 \leq r < \infty$, where J is the Richardson number. Leibovich applied the Howard and Gupta condition to a columnar vortex, referred to in the literature as the "Q-vortex," with the following axial and azimuthal velocity profiles:

$$w(r) = 1 + \delta e^{-r^2} \tag{C.20}$$

$$v(r) = q|\delta|(1 - e^{-r^2}). \tag{C.21}$$

These profiles were chosen to model flows upstream and downstream of breakdown events observed in tubes by Garg and Leibovich (1979). Leibovich found that the stability condition (C.19) becomes $q \geq 0.403$ for the Q-vortex.

The stability of the vortex examined in the last section is indeterminate, according to the Howard and Gupta condition, since both Φ and $\dot{w}$ are zero outside the vortex core. A similar problem is encountered when the stability of solutions presented in Chapter 3 is evaluated. For these solutions, computed data reflected freestream conditions outside the vortex core but within the computational domain, so that the Richardson number could not be evaluated throughout the domain. However, $J(r)$ was found to be an increasing function of r, greater than $\frac{1}{4}$, before becoming indeterminate. And, in the freestream flow region where the Richardson number becomes indeterminate, appeal can be made to the classic, necessary and sufficient stability condition for flow between rotating cylinders shown by Rayleigh (1916), which calls for stability if Γ, as a function of r, nowhere decreases between the cylinders. One can think of the vortex core, which is stable according to the Howard and Gupta condition, as a cylinder that generates circulation in the surrounding freestream. Since the generated circulation does not decrease as a function of r in the freestream flow, stability is suggested by the Rayleigh criterion.

Appendix D

Axial Gradients of Quasi-Cylindrical Flow

The parabolic QC equations can be integrated in the streamwise direction, assuming $w(r,z) > 0$, starting from an axial station at which flow quantities are known. An algorithm is proposed in Appendix E that can be used to integrate the QC equations explicitly. This appendix provides supporting material for the development of that algorithm and includes an example supportive of the analyses of Hall (1972) and Trigub (1985), which show that large axial gradients necessarily occur in the vicinity of critical points of the QC equations.

D.1 Local Evaluation of Axial Gradients

As the QC equations are parabolic, the axial gradients of flow quantites at an axial station may be computed when the flow quantities are known at the station. In this section, expressions for $\psi_z(r)$ and $\Gamma_z(r)$, in terms of functions determinable at specified axial stations, are developed. These results are applied to the explicit algorithm proposed in Appendix E.

In (ψ, Γ, η) form, the QC equations are (Form III — see Appendix A):

$$\eta = -w_r = -\frac{1}{r}\left(\psi_{rr} - \frac{\psi_r}{r}\right) \tag{D.1}$$

$$u\left(\eta_r - \frac{\eta}{r}\right) + w\eta_z = \frac{2\Gamma\Gamma_z}{r^3} + \frac{1}{\mathrm{Re}}\left(\eta_{rr} + \frac{\eta_r}{r} - \frac{\eta}{r^2}\right) \tag{D.2}$$

$$u\Gamma_r + w\Gamma_z = \frac{1}{\mathrm{Re}}\left(\Gamma_{rr} - \frac{\Gamma_r}{r}\right). \tag{D.3}$$

Equation (D.1) is used to relate the axial gradient of azimuthal vorticity with the radial velocity. After differentiation of (D.1) with respect to z, (D.1) becomes

$$\eta_z = -\frac{1}{r}\left(\psi_{zrr} - \frac{\psi_{zr}}{r}\right). \tag{D.4}$$

The definition of streamfunction,

$$u \equiv -\frac{\psi_z}{r}, \tag{D.5}$$

is used in (D.4) to give

$$\eta_z = u_{rr} + \frac{u_r}{r} - \frac{u}{r^2}. \tag{D.6}$$

Equation (D.3) can be solved for the axial gradient of circulation,

$$\Gamma_z = \frac{1}{w}\left(\frac{1}{\mathrm{Re}}\left(\Gamma_{rr} - \frac{\Gamma_r}{r}\right) - u\Gamma_r\right). \tag{D.7}$$

Equations (D.6) and (D.7) are now used in (D.2) to find a second-order, ordinary differential equation for u in the independent variable r. Substitution of (D.6) and (D.7) into (D.2) gives

$$u\left(\eta_r - \frac{\eta}{r}\right) + w\left(u_{rr} + \frac{u_r}{r} - \frac{u}{r^2}\right) = \frac{1}{\mathrm{Re}}\left(\eta_{rr} + \frac{\eta_r}{r} - \frac{\eta}{r^2}\right)$$
$$+ \frac{2\Gamma}{wr^3}\left(\frac{1}{\mathrm{Re}}\left(\Gamma_{rr} - \frac{\Gamma_r}{r}\right) - u\Gamma_r\right). \tag{D.8}$$

After moving terms containing u to the left-hand side of (D.8) and then dividing by w, (D.8) becomes

$$u_{rr} + \frac{u_r}{r} + u\left(\frac{1}{w}\left(\eta_r - \frac{\eta}{r}\right) + \frac{2\Gamma\Gamma_r}{w^2r^3} - \frac{1}{r^2}\right)$$
$$= \frac{1}{w\mathrm{Re}}\left(\eta_{rr} + \frac{\eta_r}{r} - \frac{\eta}{r^2}\right) + \frac{2\Gamma}{w^2r^3\mathrm{Re}}\left(\Gamma_{rr} - \frac{\Gamma_r}{r}\right). \tag{D.9}$$

Equation (D.9) is more conveniently written as

$$u_{rr} + \frac{u_r}{r} + uf(w, \eta, \Gamma, \mathrm{Re}, r) = g(w, \eta, \Gamma, \mathrm{Re}, r), \tag{D.10}$$

where f and g are functions of the variables indicated in (D.10) and of the partial derivatives of those variables. Suppose that at some axial station, $\hat{z}$, $\psi = \hat{\psi}(r)$ and $\Gamma = \hat{\Gamma}(r)$, where $\hat{\psi}$ and $\hat{\Gamma}$ are known functions of r. Then, by (D.1),

$$\eta = -\frac{1}{r}\left(\hat{\psi}_{rr} - \frac{\hat{\psi}_r}{r}\right), \tag{D.11}$$

and by the definition of streamfunction,

$$w = \frac{\hat{\psi}_r}{r}. \tag{D.12}$$

Equation (D.10) is now expressed as

$$u_{rr} + \frac{u_r}{r} + uf(w, \eta, \hat{\Gamma}, \mathrm{Re}, r) = g(w, \eta, \hat{\Gamma}, \mathrm{Re}, r) \tag{D.13}$$

and can be solved numerically as a two-point, boundary-value problem for the radial velocity profile, u, at $\hat{z}$. An example in which this equation is solved is presented in the next section.

The calculation of u allows the determination of the axial gradients of ψ and Γ at the station. Equation (D.5) gives

$$\psi_z = -ru, \tag{D.14}$$

while (D.7) gives

$$\Gamma_z = \frac{1}{w}\left(\frac{1}{\mathrm{Re}}\left(\hat{\Gamma}_{rr} - \frac{\hat{\Gamma}_r}{r}\right) - u\hat{\Gamma}_r\right). \tag{D.15}$$

The axial gradient of azimuthal vorticity can be found from (D.6). This quantity, however, need not be evaluated to integrate the QC equations, since at every station azimuthal vorticity is given by (D.11).

D.2 An Example — Divergence of Radial Velocity Near Critical State

Hall (1972) showed that solutions of the QC equations exhibit singularities at axial stations at which critical flow conditions exist, and that axial gradients necessarily become unbounded as critical stations are approached. A rigorous

treatment of Hall's approach was given by Trigub (1985). It is demonstrated here that solutions of (D.13) also become unbounded as station conditions become critical. Through (D.14) and (D.15), divergence of the radial velocity implies divergence of the axial gradients of streamfunction and circulation.

Consider the example treated in Section (C.3), in which the criticality of an inviscid, columnar vortex, is examined. The vortex is defined by the axial velocity profile

$$w(r) = 1,$$

and the circulation profile,

$$\Gamma(r) = \begin{cases} V & r \geq 1 \\ Vr^2(2-r^2) & r < 1. \end{cases}$$

It was found that the vortex is critical when $V \approx 0.968$. We now assume that viscosity is present and that the local state of the viscous vortex is defined by the axial velocity and circulation profiles given above. With these assumed profiles, the functions appearing in (D.13) become

$$f(V, \mathrm{Re}, r) = \begin{cases} -1/r^2 & r \geq 1 \\ 8V^2(1-r^2) - 1/r^2 & r < 1 \end{cases} \tag{D.16}$$

$$g(V, \mathrm{Re}, r) = \begin{cases} 0 & r \geq 1 \\ -16V^2 r/\mathrm{Re} & r < 1. \end{cases} \tag{D.17}$$

The radial velocity profile at a specified value of V is calculated by casting (D.13) in finite-difference form through the use of central differences and then solving the resulting linear system of equations with Gaussian elimination (with partial pivoting). The boundary conditions applied to the differential equation are

$$u = 0 \qquad (r = 0) \tag{D.18}$$

$$u_r + \frac{u}{r} = 0 \quad (r = R). \tag{D.19}$$

R is assumed to be sufficiently large such that the outer boundary may be considered to be in the freestream where w_z is zero. Condition (D.19) is discretized with a second-order accurate, one-sided difference approximation.

Figure (D.1) shows a plot of the weighted L1 norm of the radial velocity,

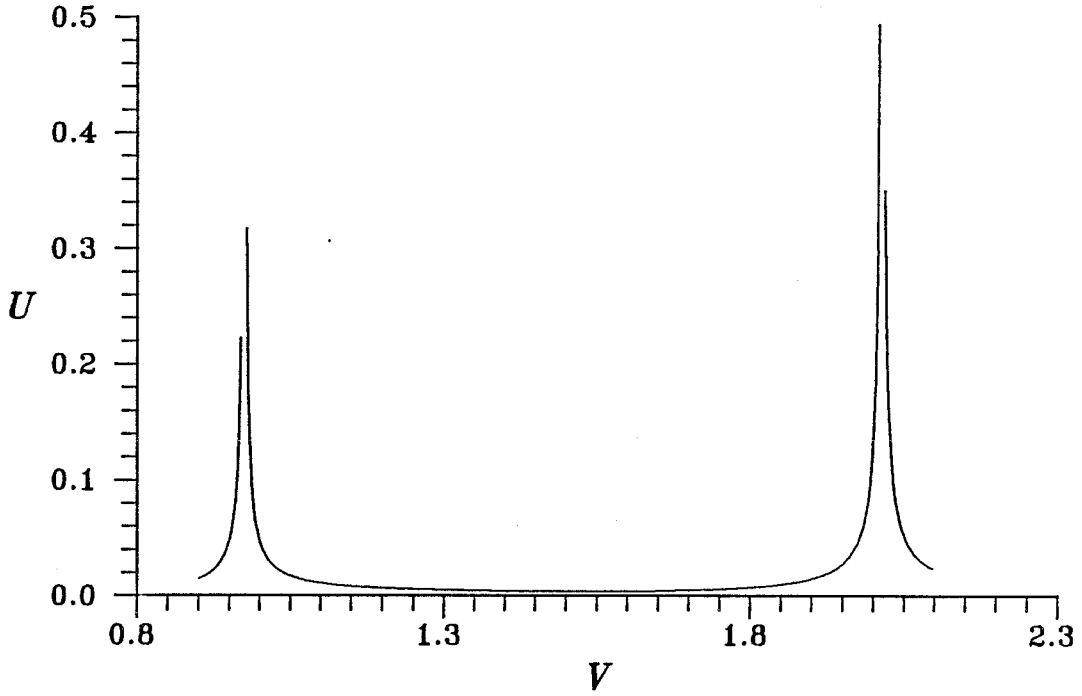

Figure D.1 Norm of radial velocity as a function of vortex strength

$$U \equiv \left(h_r \sum_{j=1}^{J} u_j^2 \right)^{1/2}, \tag{D.20}$$

versus V for V ranging between 0.8 (supercritical) and 2.1 (subcritical). Reynolds number was assumed to be 1000, so that local conditions would approximate that of the inviscid, columnar vortex studied in Section (C.3). R was chosen to be 2 and the number of nodes in the radial direction was chosen to be 27. Singularities are apparent at $V \approx 0.975$ and $V \approx 2.013$. The former singularity corresponds to the critical point identified in Section (C.3). The latter singularity corresponds to a critical point that occurs when a second eigenvalue of (C.18) becomes positive. The development of multiple critical points was suggested by Trigub (1985). The small difference in the value of V at which the singularity is observed and the value of V at which a critical point occurs, as computed in Section (C.3), can be attributed to a discretization error. Increasing R and the number of nodes used to discretize the interval reduced the difference.

Appendix E

Integration of the Quasi-Cylindrical Equations

As discussed in Chapter 1, integration of the QC equations served as an early tool for the investigation of vortex breakdown for various flow situations. Conditions upstream of breakdown events that were experimentally observed served as initial conditions for the integration procedure. Breakdown was thought to occur in the vicinity of where the computed flow became critical, since at such points the QC equations become singular. (Hall (1972)).

As a research tool, integration of the QC equations has been found to be of only limited use. Hall (1972) and Leibovich (1978) have observed that breakdown occurs in supercritical flow, indicating that the singularity associated with critical flow is not the direct cause of breakdown. Breakdown was also found to occur in supercritical flow in the results presented in Chapter 3. And, as noted in Chapter 1 and observed in the results shown in Chapter 4, the divergence of the QC equations is very abrupt and provides no structural information about breakdown. Trigub (1985) has shown that the solution of the QC equations cannot be continued through the singularity.

There are several reasons for having developed an algorithm for the integration of the QC equations and for reporting results of calculations using this algorithm in Chapter 4. First, and most importantly, onset of transition is observed to be dependent on the local state of the vortex and should be governed by a criterion or set of criteria based on the local axial and azimuthal velocity profiles. Since divergence of the QC equations occurs downstream of the transition point, solutions of

the QC equations provide an accurate description of the flow up to transition and could be used to evaluate the criterion or criteria on which the onset of transition depends. Solutions of the QC equations also serve as a useful check of solutions of the Navier-Stokes in regions where the QC equations are valid. The algorithm described in this appendix has advantages over previously reported schemes, since the scheme is very efficient and since the QC equations are solved in (ψ,Γ,η) form.

E.1 Integration Algorithm

The QC equations are integrated by computing the flow state at successive axial stations with the explicit, first-order accurate, Euler method. The axial gradients of flow quantities at each station are approximated by evaluating (D.11), (D.14) and (D.15) in finite-difference form, after having solved (D.13) for the radial velocity profile. The computational domain is discretized in the manner described in Chapter 2. Partial derivatives with respect to radial position are approximated with second-order accurate, central differences, while partial derivatives with respect to axial position are approximated with first-order accurate, one-sided differences.

The finite-difference representations of (D.11—D.15) can be expressed in terms of three different, finite-difference operators, $\triangle_z^+$, $\triangle_{rr}$ and $\triangle_r^o$, defined as follows (h_r and h_z are the node spacings in the radial and axial coordinate directions respectively):

$$\triangle_z^+ x_{(i,j)} \equiv \frac{x_{(i+1,j)} - x_{(i,j)}}{h_z} \tag{E.1}$$

$$\triangle_{rr} x_{(i,j)} \equiv \frac{x_{(i,j+1)} + x_{(i,j-1)} - 2x_{(i,j)}}{h_r^2} \tag{E.2}$$

$$\triangle_r^o x_{(i,j)} \equiv \frac{x_{(i,j+1)} - x_{(i,j-1)}}{2h_r}. \tag{E.3}$$

Assume that streamfunction and circulation are known at each node corresponding to an axial station defined by $i = n$. Then, the definitions of azimuthal vorticity and streamfunction (see Section (A.5)) give

$$w_{(n,j)} = \frac{1}{r_{(j)}} \Delta_r^o \psi_{(n,j)} + O(h_r^2) \tag{E.4}$$

$$\eta_{(n,j)} = -\frac{1}{r_{(j)}} \left(\Delta_{rr} \psi_{(n,j)} - \frac{1}{r_{(j)}} \Delta_r^o \psi_{(n,j)} \right) + O(h_r^2). \tag{E.5}$$

The discrete profile of radial velocity is computed to second-order accuracy ($O(h_r^2)$) by solving a system of equations derived from the finite-difference approximation to (D.13),

$$\Delta_{rr} u_{(n,j)} + \Delta_r^o u_{(n,j)} + u_{(n,j)} f_{(n,j)} = g_{(n,j)}, \tag{E.6}$$

where $f_{(n,j)}$ and $g_{(n,j)}$ are known functions of $w_{(n,j)}$, $\eta_{(n,j)}$, $\eta_{(n,j\pm1)}$, $\Gamma_{(n,j)}$ and $\Gamma_{(n,j\pm1)}$.

The discrete radial velocity profile is used to predict the axial gradients of ψ and Γ at each of the station node points. The discrete forms of (D.14) and (D.15) are

$$\Delta_z^+ \psi_{(n,j)} = -r_{(j)} u_{(n,j)} + O(h_z, h_r^2) \tag{E.7}$$

$$\Delta_z^+ \Gamma_{(n,j)} = \frac{1}{w_{(n,j)} \mathrm{Re}} \left(\Delta_{rr} \Gamma_{(n,j)} - \frac{\Delta_r^o \Gamma_{(n,j)}}{r_{(j)}} \right)$$

$$- \frac{u_{(n,j)} \Delta_r^o \Gamma_{(n,j)}}{w_{(n,j)}} + O(h_z, h_r^2). \tag{E.8}$$

An estimate of ψ and Γ at the next station, $i = n + 1$, is computed through the Euler step

$$\psi_{(n+1,j)} = \psi_{(n,j)} + h_z \Delta_z^+ \psi_{(n,j)} \tag{E.9}$$

$$\Gamma_{(n+1,j)} = \Gamma_{(n,j)} + h_z \Delta_z^+ \Gamma_{(n,j)}. \tag{E.10}$$

The integration proceeds by repeating the calculations outlined in (E.1—E.10) for station $i = n + 1$ and for all other stations downstream of station n.

E.2 Boundary Conditions

For the parabolic problem, boundary conditions must be specified on surfaces S1, S2 and S3 (see Figure (2.2)). At the inflow surface, the streamfunction and circulation profiles are specified. It is not necessary to specify the vorticity profile on this surface, since the vorticity profile can be computed from the discrete form of (D.1). Since S2 is assumed to lie in the freestream, the following boundary conditions are chosen:

$$\psi_r(R) \equiv -Rw(R) = -R \tag{E.11}$$

$$\eta(R) \equiv -w_r(R) = 0 \tag{E.12}$$

$$\Gamma(R) = V. \tag{E.13}$$

On the symmetry axis, the conditions $\psi = \eta = \Gamma = 0$ are applied.

Bibliography

[1] Batchelor, G.K. 1967 *An Introduction to Fluid Dynamics.* Cambridge University Press.

[2] Benjamin, T.B. 1962 Theory of the Vortex Breakdown Phenomenon. *J. Fluid Mech.*, **14** (4), 593.

[3] Benjamin, T.B. 1965 Significance of the Vortex Breakdown Phenomenon. *Trans. of the ASME*, **87**, 518.

[4] Benjamin, T.B. 1967 Some Developments in the Theory of Vortex Breakdown. *J. Fluid Mech.*, **28** (1), 65.

[5] Beran, P.S. 1986 Numerical Simulation of Vortex Breakdown. *Caltech Ae200 Report.*

[6] Beran, P.S. 1987 Numerical Simulations of Trailing Vortex Bursting. *AIAA Paper* 87-1313.

[7] Beran, P.S. 1988, to be published.

[8] Brown, G.L. and Lopez J.M. 1988 Axisymmetric Vortex Breakdown Part II: Physical Mechanisms. *Aero. Res. Lab. Aero. Report* 174.

[9] Chandrasekhar, S. 1961 *Hydrodynamic and Hydrodynamic Stability.* Oxford University Press.

[10] Chorin, A.J. 1967 *J. Comp. Phys.*, **2**, 2.

[11] Elle, B.J. 1960 On the Breakdown at High Incidences of the Leading E. V. on Delta Wings. *J. of the Royal Aero. Soc.*, **64**, 491.

[12] Faler, J.H. and Leibovich, S. 1977 Disrupted States of Vortex Flow and Vortex Breakdown. *Physics of Fluids*, **20** (9), 1385.

[13] Faler, J.H. and Leibovich, S. 1978 An Experimental Map of the Internal Structure of a Vortex Breakdown. *J. Fluid Mech.*, **86** (2), 313.

[14] Fier, J.M. 1985 Fold Continuation and the Flow between Rotating, Coaxial Disks. Ph.D. Thesis, California Institute of Technology.

[15] Garg, A.K. 1977 Oscillatory Behavior in Vortex Breakdown Flows: an Experimental Study Using a Laser Doppler Anemometer. MS Thesis, Cornell University.

[16] Garg, A.K. and Leibovich, S. 1979 Spectral Characteristics of Vortex Breakdown Flowfields. *Phys. Fluids*, **22** (11), 2053.

[17] Gartshore, I.S. 1962 Recent Work in Swirling Incompressible Flow. *Nat. Res. Council Report* LR-343.

[18] Grabowski, W.J. 1972 Solutions of the Navier-Stokes Equations for Vortex Breakdown. *Berkeley Report* FM-74-6.

[19] Grabowski, W.J. and Berger, S.A. 1976 Solutions of the Navier-Stokes Equations for Vortex Breakdown. *J. Fluid Mech.*, **75** (3), 525.

[20] Hafez, M., Kuruvila, G. and Salas, M.D. 1986 Numerical Study of Vortex Breakdown. *AIAA Paper* 86-0558.

[21] Hafez, M., Ahmad, J., Kuruvila, G. and Salas, M.D. 1987 Vortex Breakdown Simulation. *AIAA Paper* 87-1343.

[22] Hall, J.L. 1985 An Introduction to Vortex Breakdown and Vortex Core Bursting. *Nat. Res. Council* No. 24336.

[23] Hall, M.G. 1965 A Numerical Method for Solving the Equations for a Vortex Core. *Aero. Res. Council* RM-3467.

[24] Hall, M.G. 1967 A New Approach to Vortex Breakdown. *Proc. Heat Trans. Fluid Mech. Inst.*, 319.

[25] Hall, M.G. 1972 Vortex Breakdown. *Ann. Rev. of Fluid Mech.*, **4**, 195.

[26] Harvey, J.K. 1962 Some Observations of the Vortex Breakdown Phenomenon. *J. Fluid Mech.*, **14**, 585.

[27] Howard, L.N. and Gupta, A.S. 1962 On the Hydrodynamic and Hydromagnetic Stability of Swirling Flows. *J. Fluid Mech.*, **14**, 463.

[28] Keller, H.B. 1977 Numerical Solution of Bifurcation and Nonlinear Eigenvalue Problems. *Applications of Bifurcation Theory.* Academic Press, New York, p. 359.

[29] Keller, H.B. 1982 Continuation Methods in Computational Fluid Dynamics. *Numerical and Physical Aspects of Aerodynamic Flows*, (ed. T. Cebeci). Springer-Verlag, New York, p. 3.

[30] Kirkpatrick, D.L.I. 1964 Experimental Investigation of the Breakdown of a Vortex in a Tube. *Aero. Res. Council* CP-821.

[31] Kopecky, R.M. and Torrance K.E. 1973 Initiation and Structure of Axisymmetric Eddies in a Rotating Stream. *Computers and Fluids*, **1**, 289.

[32] Krause, E., Shi, X.G. and Hartwich, P.M. 1983 Computation of Leading-Edge Vortices. *AIAA Paper* 83-1907.

[33] Lambourne, N.C. and Bryer, D.W. 1961 The Bursting of Leading-edge Vortices—Some Observations and Discussions of the Phenomenon. *Aero. Res. Council* RM-3282.

[34] Leibovich, S. 1978 The Structure of Vortex Breakdown. *Ann. Rev. of Fluid Mech.*, **10**, 221.

[35] Leibovich, S. 1983 Vortex Stability and Breakdown. *AGARD Report* CP-342, No. 23.

[36] Leibovich, S. 1984 Vortex Stability and Breakdown: Survey and Extension. *AIAA Journal*, **22** (9), 1192.

[37] Lopez, J.M. 1988 Axisymmetric Vortex Breakdown Part I: Confined Swirling Flow. *Aero. Res. Lab. Aero. Report* 173.

[38] Lopez, J.M. 1988, private communication.

[39] Menne, S. 1988 Vortex Breakdown in an Axisymmetrtic Flow. *AIAA Paper* 88-0506.

[40] Morton, B.R. 1969 The Strength of Vortex and Swirling Core Flows. *J. Fluid Mech.*, **38** (2), 315.

[41] Nakamura, Y., Leonard, A. and Spalart, P.R. 1985 Vortex Breakdown Simulation. *AIAA Paper* 85-1581.

[42] Nakamura, Y., Leonard, A. and Spalart, P.R. 1986 Internal Structure of a Vortex Breakdown. *AIAA Paper* 86-107.

[43] Peckham, D.H. and Atkinson, S.A. 1957 Preliminary Results of Low-Speed Wind Tunnel Tests on Gothic Wing of AR 1.0. *Aero. Res. Council* CP-508.

[44] Rayleigh, J.W.S. 1916 On the Dynamics of Revolving Fluids. *Proc. Roy. Soc. A*, **93**, 148.

[45] Sarpkaya, T. 1971A On Stationary and Travelling Vortex Breakdowns. *J. Fluid Mech.*, **45** (3), 585.

[46] Sarpkaya, T. 1971B Vortex Breakdown in Swirling Conical Flows. *AIAA Journal*, **9** (9), 1792.

[47] Sarpkaya, T. 1974 Effect of the Adverse Pressure Gradient on Vortex Breakdown. *AIAA Journal*, **12** (9), 602.

[48] Táasan, S. 1986 Multigrid Method for a Vortex Breakdown Simulation. *NASA Contractor Report* 178106.

[49] Trigub, V.N. 1985 The Problem of Breakdown of a Vortex Line. *PMM U.S.S.R.*, **49** (2), 166.